2016

Scanning Probe Investigations of Multidentate Thiol and Spatially Confined Porphyrin Nanoassemblies using Nanoscale Lithography

Xianglin Zhai Zhai
Louisiana State University and Agricultural and Mechanical College, xzhai1@lsu.edu

SCANNING PROBE INVESTIGATIONS OF MULTIDENTATE THIOL AND SPATIALLY CONFINED PORPHYRIN NANOASSEMBLIES USING NANOSCALE LITHOGRAPHY

A Dissertation

Submitted to the Graduate Faculty of the
Louisiana State University and
Agricultural and Mechanical College
in partial fulfillment of the
requirements for the degree of
Doctor of Philosophy

in

The Department of Chemistry

by
Xianglin Zhai
B.S., Northeast Forestry University, 2006
M.S., Northeast Forestry University, 2009
May 2016

ACKNOWLEDGMENTS

I would like to thank my advisor, Dr. Jayne C. Garno. She has truly given me the encouragement, inspiration, and guidance needed during my time at LSU. I would like to thank her for affording me the opportunity to work in her group, and for playing an instrumental role in my academic success. She is truly a woman who cares about the success of her students. I would also like to thank Dr. Justin Ragains, my collaborator. He has been a blessing as both a mentor and a role model during my graduate career. Thank you to my committee members Dr. Bin Chen, Dr. Louis Haber, and Dr. Kevin S. McCarter for reviewing my dissertation and providing valuable feedback.

To the Garno group (both past and present), the blood, sweat, and tears we shared will always be held close to my heart. It was truly a pleasure to work for a group with such a nurturing and collaborative spirit. I will miss all of the tailgates, lunches, group parties, and conference trips we've shared over the years. I hope to stay in touch with each of you, and wish you all the success in the future. Specifically, I like to acknowledge my colleagues, Dr. Tian Tian, Dr. Lauren Englade-Franklin, Dr. ChaMarra Saner, and Dr. Susan Sutton. Each of you has played an integral role in my research in some way, and for that I will be forever grateful. More importantly, you have each become a friend, and I cannot express how much this means to me personally.

To my parents Xilan Zhai and Guilan Yue, I must say thank you for always putting up with me! Your love and support have led me to where I am today. Mom, you are the strongest woman I have ever met. Thank you for always standing up for what is right, and being the amazing role model you are. You've always been there for me, and I can't tell you how much I love you. Dad, you have pushed me to always succeed and never give up. Thank you for teaching me what is

worth fighting and working for in life, I love you. I would also like to thank my families in China. Your love is the powerful and secure backing for me whenever I was facing difficulties in my life.

Finally, I would like to express my gratitude and love to my darlings, Zheng Xue and Sophia S. Zhai. It is a huge bless that I have you in my life. Thank you my wife, Zheng Xue for always believing in me when I doubt myself. I would not step so far without your support. Thank you my beloved Sophia, thank you for being in my life. Your arrival to my life made me grown, tough and fearless to my unknown future. You are both my families, my love and my best friends. I love you both forever!

TABLE OF CONTENTS

LIST OF TABLE

LIST OF SCHEMES

LIST OF FIGURES

LIST OF ABBREVIATIONS

ABBREVIATION	NAME
AC-AFM	Alternating contact atomic force microscopy
AFM	Atomic force microscopy
BMPHA	16-[3,5-bis(mercaptomethyl)phenoxy] hexadecanoic acid
CP-AFM	Conductive-probe atomic force microscopy
DPN	Dip-pen nanolithography
I-V	Current-voltage
MHA	16-mercaptohexadecanoic acid
MOS	Metal-oxide-semiconductor
NbN	Niobium nitride
NPRW	NanoPen Reader and Writer
SAM	Self-assembled monolayer
SPM	Scanning probe microscopy
STM	Scanning tunneling microscopy
TPC	5,10,15,20-tetraphenyl-21H,23H-porphine cobalt(II)
TPP	5,10,15,20-tetraphenyl-21H,23H-porphine
TSG	Templated stripped gold

ABSTRACT

Approaches to prepare spatially selective surfaces were developed in this dissertation for constructing nanopatterns of organic thin film materials. Nanoscale surface patterns were prepared using immersion particle lithography and scanning probe lithography combined with organothiol chemistry. Organic thin films and nanomaterials can be patterned with tunable periodicities and designed shapes by selecting the diameter of mesospheres used as surface masks or scanning probe lithography, respectively. The surface platforms of well-defined nanopatterns are ideal for high resolution investigations using scanning probe microscopy (SPM). Local measurements of surface properties and conductive properties combined with nanolithography were accomplished at the molecular level.

Sample characterizations were accomplished with selected modes of SPM. Scanning probe studies can be used to probe the morphological and physical properties of samples, when spatially confined nanomaterials are prepared. Atomic force microscopy (AFM) can be used to analyze many types of samples in ambient and liquid environments. Arrays of nanostructures formed with newly designed molecules and porphyrins were fabricated using the spatial selectivity of chemical patterns prepared with nanolithography. The designed nanopatterns were evaluated for morphological details and physical properties.

A newly designed bidentate organosulfur compound, i.e. 16-[3,5-bis(mercaptomethyl)phenoxy] hexadecanoic acid (BMPHA), was selected for study. The solution phase self-assembly onto Au(111) was investigated with scanning probe-based nanolithography and particle lithography. The two thiol groups of BMPHA were specially designed as surface linkers for improved stability. The orientation of BMPHA on Au(111) was investigated by referencing the heights of *n*-alkanethiols as an *in situ* molecular ruler. Protocols for patterning

porphyrin nanostructures i.e. nanodots and nanorods on Au(111) were developed based on protocols with immersion particle lithography. Porphyrins with and without a central metal ion, 5,10,15,20-tetraphenyl-21H,23H-porphine (TPP) and 5,10,15,20-tetraphenyl-21H,23H-porphine cobalt(II) (TPC) were patterned using immersion particle lithography. Individual nanorods and nanodots of porphyrins were spatially isolated into well-defined, nanoscale arrangements directed by a template film of a nanopatterned thiol monolayer. The conductivity of the nanostructures of the porphyrins was evaluated using conductive probe-atomic force microscopy (CP-AFM). The studies evaluate the applicability of nanolithography for preparing surface platforms for the measurements of morphological and physical properties at the nanoscale.

CHAPTER 1: INTRODUCTION

Approaches were developed in this dissertation to prepare spatially selective surfaces for constructing assemblies of organic materials by combining particle lithography with molecular self-assembly. The surface platforms that were designed and constructed are potentially useful for investigating the surface orientation of selected molecules, providing a side-by-side comparison of surface properties at the molecular level. Surface templates were applied for evaluating electronic properties using conductive probe atomic force microscopy (CP-AFM). With nanoscale lithography, the size and shape of the nanopatterns can be controlled by selecting experimental conditions. Measurements with atomic force microscopy (AFM) provide molecular-level views of nanostructures and insight into the process of molecular self-assembly.

1.1 Nanoscale studies using scanning probe microscopy (SPM)

Molecular imaging studies began with scanning tunneling microscopy (STM) that enabled us to directly view the surface of semiconductor and metal samples. For STM, a sharp needle is brought very close (ca. one atomic diameter) to the surface to map the topography with subatomic resolution.[1] Five years after the invention of STM, AFM was introduced.[2] The invention of AFM expanded the application of scanning g probe microscopy (SPM) into studies with nonconductive samples. With the development of SPM, scientists have conquered the limitation of the Rayleigh wavelength of light for imaging resolution. Scanning probe techniques opened new possibilities for nanotechnology. In Chapter 2, the background and basic principles of SPM will be described along with the advanced modes of AFM used in this dissertation.

1.2 Self-assembly of bidentate thiol on Au(111) studied with AFM[3]

In Chapter 3, The solution-phase self-assembly of bidentate 16-[3,5-bis(mercaptomethyl)phenoxy]hexadecanoic acid (BMPHA) on Au(111) was studied using

nanofabrication protocols with scanning probe nanolithography and immersion particle lithography. Molecularly thin films of BMPHA prepared by surface self-assembly have potential application as spatially selective layers in sensor designs. Either monolayer or bilayer films of BMPHA can be formed in ambient conditions, depending on the parameters of concentration and immersion intervals. Experiments with scanning probe-based lithography (nanoshaving and nanografting) were applied to measure the thickness of BMPHA films. The thickness of a monolayer and bilayer film of BMPHA on Au(111) were measured *in situ* with atomic force microscopy (AFM) using *n*-octadecanethiol as an internal reference. Scanning probe-based nanofabrication provides a way to insert nanopatterns of a reference molecule of known dimensions within a matrix film of unknown thickness to enable a direct comparison of heights and surface morphology. Immersion particle lithography was used to prepare a periodic arrangement of nanoholes within films of BMPHA. The nanoholes could be backfilled by immersion in a SAM solution to produce nanodots of *n*-octadecanethiol surrounded by a film of BMPHA. Test platforms prepared by immersion particle lithography enables control of the dimensions of surface sites to construct supramolecular assemblies.

1.3 Measurement of spatially confined nanoclusters of porphyrins using CP-AFM

The conductive properties of nanodots of model porphyrins were investigated using conductive-probe atomic force microscopy (CP-AFM) in Chapter 4. Porphyrins provide excellent model structures that can be used as potential building blocks for molecular devices. The conjugated, planar structure of porphyrins offers opportunities for tailoring the electronic properties. Two model porphyrins were selected, 5,10,15,20-tetraphenyl-21H,23H-porphine cobalt(II) (TPC) and its metal free analogue 5,10,15,20-tetraphenyl-21H,23H-porphine (TPP) for CP-AFM studies. Arrays of TPP and TPC nanodots were prepared within a dodecanethiol resist

on Au(111) using particle lithography. The nanopatterned surfaces exhibit millions of reproducible test structures in a periodic arrangement. Only a single measurement was made for each nanodot since the voltages used for CP-AFM measurements were found to damage the samples, evident in I-V profiles. The porphyrin nanostructures have slight differences in dimensions at the nanoscale, to enable size-dependent measurements of conductive properties. The size of the nanodots corresponds to ~ 3-5 layers of porphyrin. The conductivity along the vertical direction of the nanodots was measured by applying a bias voltage between the Au(111) surface and a metal-coated AFM cantilever. The TPP nanodots exhibited semi-conductive profiles while the TPC nanodots exhibited profiles that are typical of a conductive film or molecular wire. The engineered nanostructures of porphyrins provide an effective platform for investigation and measurement of conductive properties.

1.4 Nanorods derived from porphyrins characterized with CP-AFM

In Chapter 5, protocols for preparing porphyrin nanostructures i.e. nanorods on Au(111) were developed based on immersion particle lithography. Porphyrins with and without a central metal ion, TPP and TPC were placed on surfaces using steps of solution immersion of a gold substrate masked with silicon mesospheres. Individual nanorods of porphyrins were spatially arranged into well-defined, nanoscale arrays directed by a template film of a nanopatterned thiol monolayer. A surface mask of silica mesospheres was used to prepare nanopores within an alkanethiol matrix film. Nanopores within a methyl-terminated alkanethiol matrix were backfilled with porphyrins by an immersion step. By controlling the concentration and immersion interval, nanorods of porphyrins were generated. The porphyrin nanorods exhibited slight differences in dimensions at the nanoscale, to enable size-dependent measurements of conductive properties. The conductivity along the horizontal direction of the nanorods was evaluated using CP-AFM. Changes

in conductivity were measured along the long axis of TPP and TPC nanorods. The TPP nanorods exhibited conductive behavior of a rectifier. The TPC nanorods exhibited typical behavior of a semi-conductive film.

1.5 Synopsis

Nanolithography combined with self-assembly can generate nanostructures with designed shapes and sizes. The nanostructures demonstrated in this dissertation include nanopatterns of alkanethiol SAMs and arrays of porphyrins in defined arrangements. For investigations using AFM, controlling the size and orientation of samples on surfaces provides advantages for nanoscale measurements. In Chapter 6, the key results of the dissertation are presented along with a discussion of future directions for research experiments.

CHAPTER 2: ATOMIC FORCE MICROSCOPY

2.1 Overview of scanning probe microscopy

Atomic force microscopy (AFM) can be used to image, measure, and manipulate nanomaterials at the nanometer size scale, including insulating and conducting materials. The surface structures and properties of the samples are studied with AFM through the extremely weak interactions (nanonewton or piconewton) between atoms of the sample and a miniaturized force sensor. The miniaturized force sensor is usually referred to as the AFM tip, has a radius of a few nanometers and is affixed at the end of a cantilever. When the AFM tip is brought close to the surface, the interactions between the tip and sample influences the motion or the deformation of the cantilever. During the scanning of the AFM tip over the sample, information of the interaction between the probe and surface is collected to provide a surface map. With a sharp probe, the surface morphology and properties can be acquired at the atomic scale for atomically flat samples. By modifying the AFM tips and instrument setup, specific properties of the sample can be acquired including electrical properties,[4] mechanical properties,[5] magnetic properties,[6] thermal properties[7] and photochemical properties.[8] Owing to the unique operation principal, AFM can be operated under controlled temperatures, as well as in ambient, liquid and vacuum environments.[9] The capabilities and flexibility of AFM has been applied over broad areas in scientific research such as surface science, biology, material science and analytical chemistry.

Atomic force microscopy was introduced by Binnig, Quate and Gerber in 1986.[2] The idea of AFM was originated from scanning tunneling microscopy (STM), which is the predecessor of scanning probe microscopy (SPM) invented by Binning and Rohrer in 1982.[1] In the first setup of AFM, an STM was used as a detector for tracing the motion of the AFM cantilever along the surface contour.[2] In modern instruments, the scanners for AFM typically employ an optical-

deflection configuration to trace the motion of the cantilever.[10] The basic setup of an AFM is outlined in Figure 2.1.

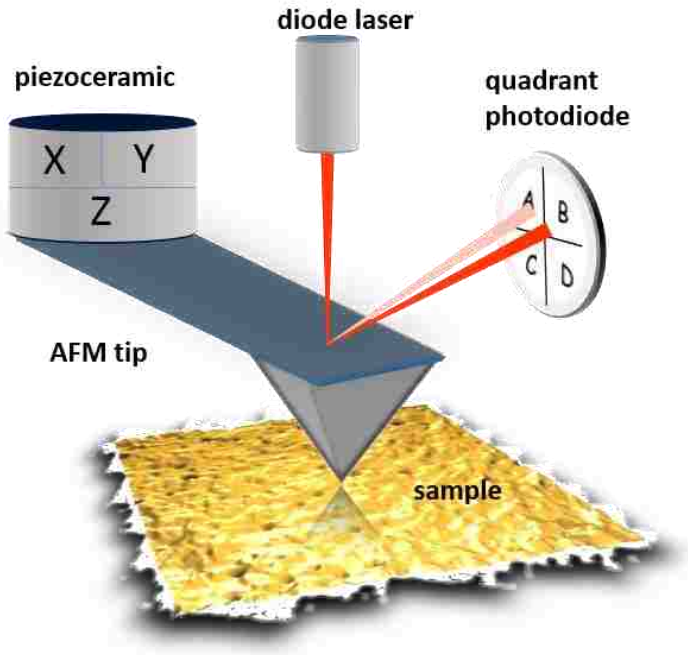

Figure 2.1 Basic setup of a tip-scan AFM.

In a typical AFM system, a scanner made of piezoceramic controls the movement of an AFM cantilever in three dimensions by expanding and contracting proportionally to an applied voltage. There are two types of scanner constructed either by a tripod piezoceramic or tube-shaped scanner. The tube scanner design has three piezoceramic elements for scanning in the x, y or z direction,[2] providing nanoscale control in three dimensions.[11] An AFM cantilever with a sharp tip is used to scan the sample. The cantilever is typically made of silicon or silicon nitride with a tip radius of curvature on the order of nanometers. The interactions between the tip and the sample cause a deformation of the cantilever according to Hooke's law, when the tip is approached into the proximity of the surface.[12] During the raster scanning of the tip over the surface, the cantilever bends according to the contour of the surface. A laser spot is shined on the back of the cantilever

and is reflected onto a position-sensitive photodiode detector to trace the motion of the tip. A 3-D image of the surface morphology can be mapped by AFM because of the motion of the tip moving in three dimensions.

The force interactions between the tip and the sample during approach are shown in Figure 2.2. No interactions between the tip and sample are present when they are separated by large distances. During the approach process, the attractive force increases between the tip and surface. The first interaction zone is known as the "non-contact" regime, in which the weak attractive forces are dominant. As the tip and sample get closer to each other, the attractive force increases rapidly until the repulsive force takes place at a distance of a few angstroms. The second interaction zone is called the "intermittent contact" regime. With intermittent contact, the strong attraction and weak repulsion are dominant. The third interaction zone is the "contact regime," where the strong repulsion forces are dominant. The three major AFM modes are classified by the distance-dependent operating regimes.

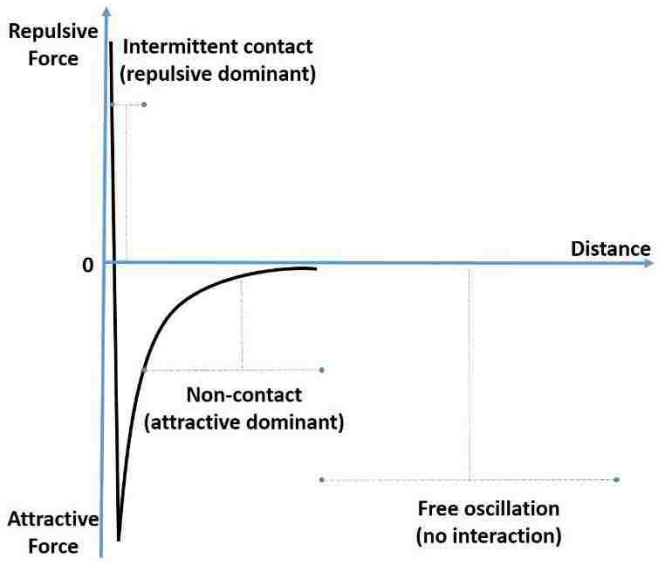

Figure 2.2 Interactions as the tip approaches the sample.

2.2 Imaging modes of AFM

The imaging modes of AFM are classified according to the forces established between the tip and surface. Three primary modes of AFM are contact mode (repulsion domain), tapping mode (weak repulsion and strong attraction domain) and non-contact mode (weak attraction dominant) each named according to the nature of the tip motion.

2.2.1 Contact mode AFM and lateral force imaging

In contact mode AFM, the tip gently touches the surface during raster scanning. There is a net repulsive force between the tip and the sample. The deflection of the cantilever is used as a feedback signal for mapping the contour of the surface morphology. For this reason cantilevers with a low spring constant, i.e. soft cantilevers, are used to boost the deflection signal. Contact mode AFM can be operated in two ways, constant height or constant force mode depending if directly using the deflection of the cantilever to map the surface contour or using the deflection as the feedback signal for the control system to keep the cantilever at a certain position, respectively. In constant height mode, the scanner is operated at a fixed height above the sample. The cantilever deflects according to the height change of the surface morphology during the scan. The topography image is mapped as the error signal which is generated by vertical movement of the reflected laser beam from the back of the cantilever. The constant height mode is usually used for imaging atomically flat surfaces, where vertical deflection of the cantilever and the exert force are small. It is sensitive to small changes in topography. In constant force mode, the scanner is operated at a certain distance from the surface. The scanner responds to the topography of the sample by compensating for the deflection of the cantilever during the scan. The error signal which is generated by vertical movement of the reflected laser beam from the back of the cantilever is used as the feedback to control the expansion and contraction of the piezoceramic in z-direction. The

force between the tip and sample is held constant by keeping the deflection of cantilever constant using the feedback loop. The topography image is generated by the output signal of the feedback circuit.

Lateral force images can be simultaneously acquired with topography images using contact mode AFM. Lateral force images reveal the difference in surface chemistry. The AFM probe interacts with the tip in the lateral direction according to frictional forces. During the scan, as the tip constantly contacts with the sample, the cantilever is twisted by the lateral interactions. The torsion of the cantilever generates a surface map of the frictional forces for identifying the surface chemistry of the sample.

Example images of topography and the corresponding lateral force images acquired by constant force contact mode AFM are shown in Figure 2.3. A densely packed film of decane was formed on Au(111) surface by immersion lithography.[13] A periodic arrangement of dark holes is observed throughout areas of the sample shown in Figure 2.3, a. The periodicity of the nanoholes measures 500 nm, which corresponds to the size of the silica mesospheres used as a surface mask. Sixty-two nanoholes are counted within a 5×5 μm^2 frame, scaling to a surface density of 10^8 nanoholes/cm^2. The sum area of the uncovered nanoholes measured ~1 % of the entire frame. A trace amount of photocatalyst is loosely adsorbed on the decane film shown as bright dots in Figure 2.3, a. Darker contrast, which corresponds to areas of the uncovered Au(111) surface, are vaguely apparent in the simultaneously acquired lateral force image (Figure 2.3, b.). The shapes of the fabricated nanoholes in decane film are clearly shown in a zoom-in view (Figure 2.3, c.). The shape of the silica mesospheres used as surface mask are not perfectly spherical. These periodic nanoholes within decane film offers a reference baseline to measure the thickness of the film *in situ.* Defects of gold substrate such as pinholes and scars are resolved in the area covered by decane

film. The uncovered bare gold areas are clearly shown with bright contrast in the simultaneously acquired lateral force image (Figure 2.3, d.). The hexagonal pattern of the nanoholes indicates the way the mesospheres are arranged on surface. An example cursor profile is shown in Figure 2.3, e., which is drawn from the white line in Figure 2.3, c. The thickness of the decane film measured 1.8 ± 0.7 nm.

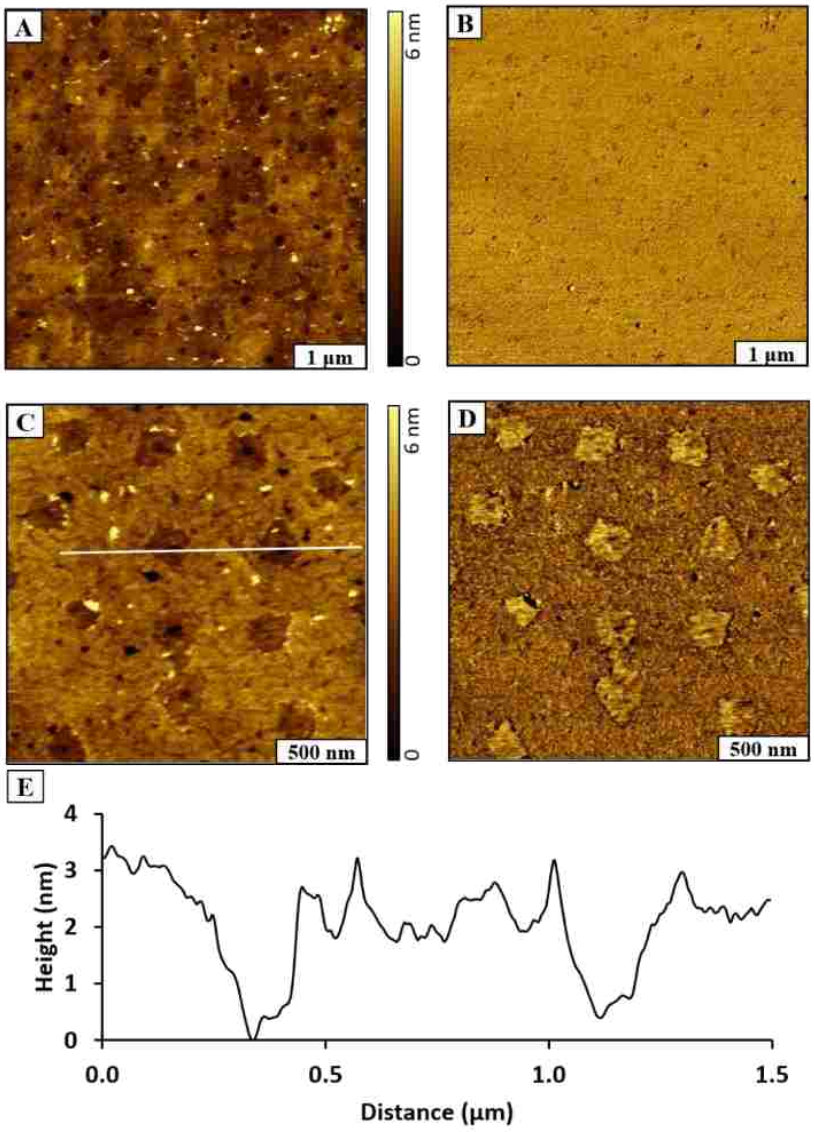

Figure 2.3 Nanopatterns prepared in a decane thin film using particle lithography. *(a)* Topography image; *(b)* simultaneously acquired lateral-force image. *(c)* Higher magnification topography image; *(d)* corresponding lateral force image. *(e)* Height profile for the white line cross-section. (Sample courtesy: Ragains Group of Louisiana State University)

2.2.2 Tapping mode AFM and phase imaging

Tapping mode is more commonly used for AFM imaging compared to contact mode imaging. With tapping mode, the lateral frictional force between the tip and the sample during imaging is absent to protect the sample, especially for soft samples.[14] In tapping mode AFM, an additional piezoelectric actuator is connected to the cantilever for driving the tip to oscillate in a sinusoidal manner over the sample. The driving frequency of the piezoelectric actuator is chosen at or near one of the resonance frequencies of the cantilever. The amplitude of the oscillating tip is monitored as the feedback of the operating process. During each oscillation cycle, the tip travels within the attraction and repulsion force (intermittent contact regime in Figure 2.2) to touch the surface of the sample. Under the complex tip-sample interactions during imaging, the amplitude and phase of the oscillating cantilever change, therefore, topography and phase images are mapped simultaneously. Tapping mode AFM is also referred to as alternating contact AFM (AC-AFM).

The feedback system for tapping mode is used to maintain a constant oscillation amplitude of the cantilever (the setpoint value). For this reason, amplitude images for tapping are not interpreted for data analysis. Similar to the deflection signal in contact mode AFM, the amplitude change caused by the interaction between the tip and the sample is called "error signal" and used as the input for the feedback system adjusting the amplitude in vertical scale to map the topography image.

The phase image is generated by the phase shift signal of the oscillating cantilever when the tip interacts with the sample. Differences in viscoelasticity can be revealed in phase images which is complementary information to the morphology images.[15] The phase shift is closely related to the amount of energy dissipated as the tip interacts with the sample. The areas with different viscoelasticity can be identified by the mapped phase shift in phase images.[16-21]

Example images of topography and corresponding phase images acquired by tapping mode AFM are shown in Figure 2.4. A cluster of body diagonal cubic Fe_3O_4 particles were imaged by tapping mode AFM in ambient conditions. The height information is shown in the topography image (Figure 2.4, a.). The morphology of the particles is not clearly shown in topography because

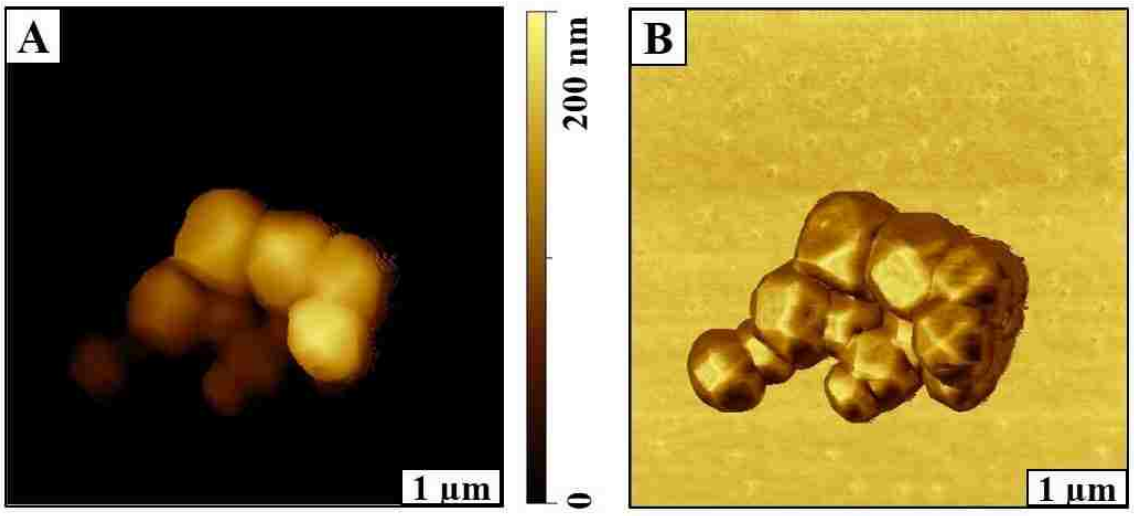

Figure 2.4 Example tapping mode images. *(a)* Topography and *(b)* phase AFM images of cubic Fe_3O_4 particles (Sample courtesy: Lee Group of University of Houston)

the height range of the imaged feature is too large to be fully expressed by the color scale.However, the shape of the particles is accurately mapped in the phase image (Figure 2.4, b.) as diagonal polyhedrons. The facets of the polyhedrons with different angles to the vertical tapping tip interact with the tip differently, thus the phase shift of the oscillating cantilever is sensitive to the tip-sample force interactions.[15] Thus, the surface features of the particles is better revealed in the phase image as compared to the topography image.

2.3 Force-distance curve

The force interactions between the AFM tip and the sample can be recorded at different distances in the cycle of approaching and retracting. A force-distance curve (force spectroscopy)

is a plot of cantilever deflection as a function of tip position in vertical direction. Forces are measured indirectly by using the stiffness of the cantilever according to Hooke's law to calculate values from the measured deflection of the cantilever.[22] Additional physico-chemiscal properties of the samples can be acquired at the nanoscale by interpreting the force-distance curve.[12, 23-24]

A typical force-distance curve acquired in air is shown in Figure 2.5. When the tip is brought to the surface from a relatively far distance (a few hundreds of nm), no force interaction is between the tip and the sample is detected until the tip is attracted to the surface by van der Waals forces at a distance of in a few nm. The attraction between the tip and the sample causes the cantilever to bend to the surface. As the cantilever keeps pushing the tip to the sample, repulsive forces increase causing the cantilever to bend against the sample. In the retracting process, the repulsive force between the tip and sample decreases as the tip withdraws from the surface. The cantilever deflection is converted from bending against the surface to bending to the surface as the repulsive force decreases to zero and the adhesion force takes place before the tip leaves the surface. The adhesion force is due to the capillary force caused by the adsorbed layer of water on the surface.

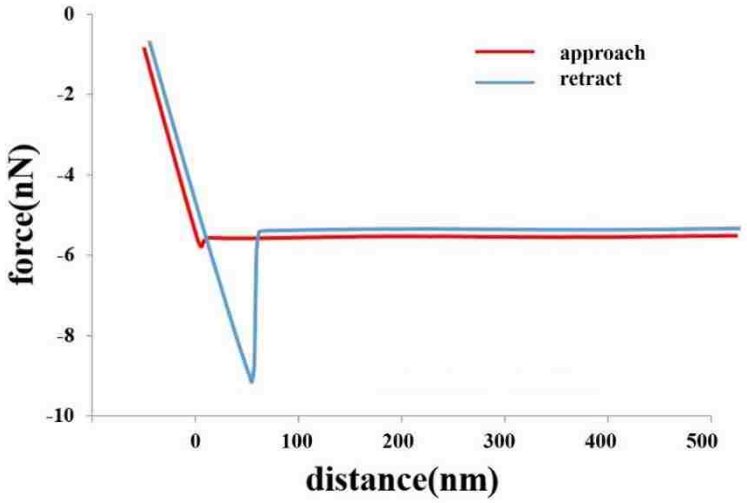

Figure 2.5 Force-distance curves for contact mode AFM acquired in air.

2.4 Liquid imaging

Liquid imaging extends the application of AFM to high resolution imaging, *in situ* imaging,[25] biological imaging,[26] biophysics[27] and nanografting.[28] The experimental setup for liquid imaging is shown in Figure 2.6. The liquid cell is made from polycarbonate and can be used with a certain chemical solvents. The cell is mounted onto a regular AFM sample plate. The feeding syringe is connected to the liquid cell with 0.9 mm tubing for maintaining and replenishing the liquid level inside the AFM liquid cell for several hours for imaging or observing the kinetics of surface reactions.

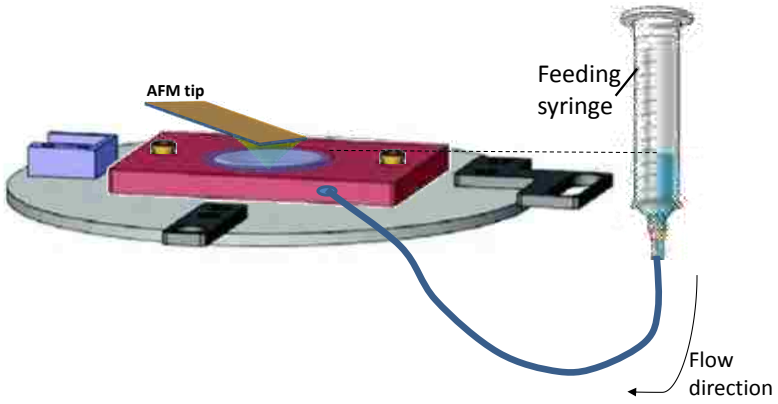

Figure 2.6 Experimental setup for AFM liquid imaging

A major merit of liquid imaging is eliminating the capillary force between the tip and the sample. A typical force-distance curve acquired in liquid media is presented in Figure 2.7. Compared to the force-distance curve acquired in air (Figure 2.5), the capillary forces of attraction are substantially decreased in the retracting process when the tip is operated in liquid media. This is due to the absence of the adsorbed layer of water at the surface. The minimized capillary force facilitates the quality of AFM images owing to the overall lower forces exerted for imaging.[22] Molecular and atomic lattices can be resolved by AFM in liquid environment.[29-31]

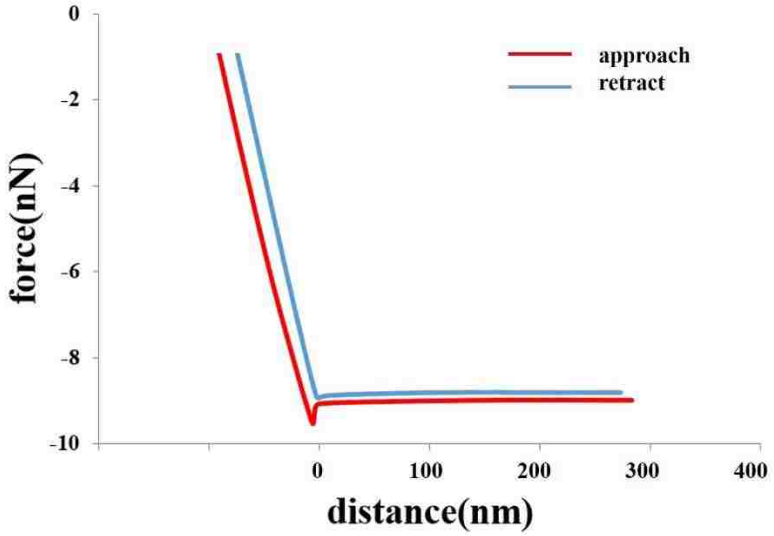

Figure 2.7 Force-distance curves for contact mode AFM acquired in ethanol.

With the function of liquid imaging, advanced experiments can be performed with AFM. For example, biological samples under physiological conditions can be imaged.[32-33] The surface reactions of organic molecules can be imaged *in situ* in liquid environments.[25] Mechanical properties between biological molecules can be measured, such as the unfolding energy of DNA and binding energy of proteins.[4]

2.5 Scanning probe fabrication

Nanopatterns can be accurately fabricated as templates to selectively graft molecules.[34-35] Atomic force microscope-based lithography methods can be applied to fabricate nanopatterns within organic thin films, while maintaining the capability of molecular-level imaging with the same probe used to fabricate the nanopatterns.[36-37] Representative methods of scanning probe fabrication include nanoshaving,[28] nanografting,[38] dip-pen nanolithography (DPN),[39] NanoPen Reader and Writer (NPRW),[40] tip-directed material deposition,[41] local oxidation nanolithography,[42-43] local chemical or electrochemical lithography,[44] tip-induced catalysis,[45] and

thermal-mechanical based writing.[46] Nanoshaving and nanografting will be introduced in this section in detail since these methods were applied in Chapter 3.

2.5.1 Nanoshaving

Besides imaging the surface with a tip, AFM can also manipulate the surface material by applying a high force onto the tip. Nanoshaving was first reported in 1994 for a *n*-alkanethiol self-assembled monolayer (SAM) on Au(111).[47] In the following year, an octadecyltriethoxysilane SAM on mica was nanoshaved by the same approach.[48] Since then, nanoshaving has been widely applied for nanoscale experiments[49-50] and for constructing nanoscale features.[51-52] Nanoshaving has three steps described in Figure 2.8.

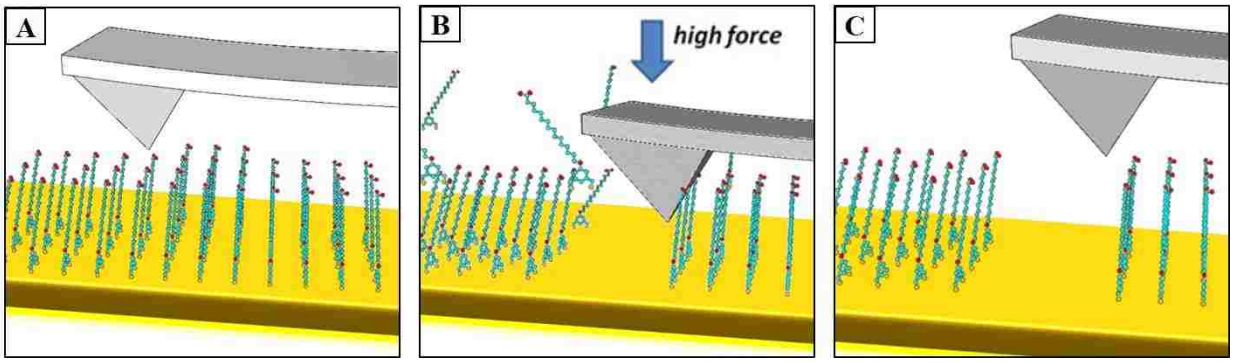

Figure 2.8 Steps of nanoshaving. *(a)* Surface characterization under low force. *(b)* Nanoshaving is accomplished by exerting high force onto selected area. *(c)* Returning to low imaging force, the nanoshaved patterns can be imaged with the same AFM tip.

To accomplish nanoshaving, the probe is swept multiple times across a small region with a higher mechanical force applied to the AFM tip (Figure 2.8, b.). The sweeping action of the probe is used to remove or displace molecules of the matrix SAM. The area can be characterized *in situ* using the same probe by returning to low force for nondestructive AFM imaging (Figure2.8, c.). The amount of force that is required and the number of times needed to cleanly sweep an area needs to be evaluated for each experiment, depending on the sharpness of the probe. Nanoshaving can be done in either ambient air or in a liquid environment. In air, the molecules are displaced to

form piles at the edges of the nanoshaved patterns. In liquid media, the shaved molecules can be swept away to produce clean edges at the sides of nanopatterns.

A square nanoshaved pattern (200 × 250 nm^2) was fabricated within a SAM of 1-dodecanethiol on Au(111). The nanoshaved area is the dark square shown in the topography image (Figure 2.9, a.) and reveals the underlying gold substrate. To assess how effective the nanoshaving parameters were for removal of 1-dodcanethiol molecules from the Au(111) surface, the simultaneously acquired lateral force image is shown in Figure 2.9, b. The dark area of the square nanopattern located at the left side of the image indicates the exposed areas of the Au(111) substrate, which indicates clean removal of dodecanethiol molecules. The tip-surface interactions mapped in lateral force frames are distinct for the gold surface and methyl end groups of dodecanethiol. Two domains are clearly shown in the scanned frame, i.e., the dodecanethiol SAM

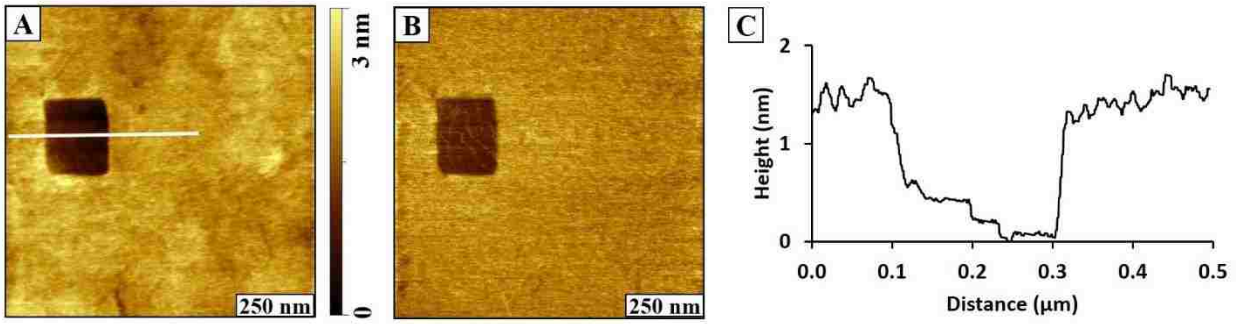

Figure 2.9 Topography and lateral force AFM images of a nanoshaved square within dodecanethiol. *(a)* Topography image acquired in ethanol; *(b)* simultaneously acquired lateral force image; *(c)* cursor profile of the line drawn in *(a)*.

and the rectangular area of the Au(111) substrate in the topography and corresponding lateral force images. The thickness of dodecanethiol can be locally evaluated with a cursor measurement, referencing the uncovered area of the substrate as a baseline at the bottom of the nanoshaved square pattern (Figure 2.9, c.). The thickness of the dodecanethiol film measured 1.5 ± 0.2 nm, which is in close agreement with the value obtained by ellipsometry and simulation.[53-55] A conservative

error term of 0.2 nm is reported due to the roughness of the underlying gold substrate, which is based on the height of a single gold terrace step.

2.5.2 Nanografting

Nanografting is an AFM-based approach for fabricating nanopatterns within organic thin films using an AFM tip under force. The process of nanografting is shown in Figure 2.10, which was invented by Song Xu in 1997.[28] Nanografting is accomplished in a liquid environment that contains the selected molecules for patterning. A single sweep of the selected area at high force is used to remove molecules of the matrix SAM simultaneously as molecules from solution self-assemble onto uncovered areas of the substrate (Figure 2.10, b.). Returning to low force for *in situ* imaging, the nanografted patterns can be characterized using the same AFM tip (Figure 2.10, c.).

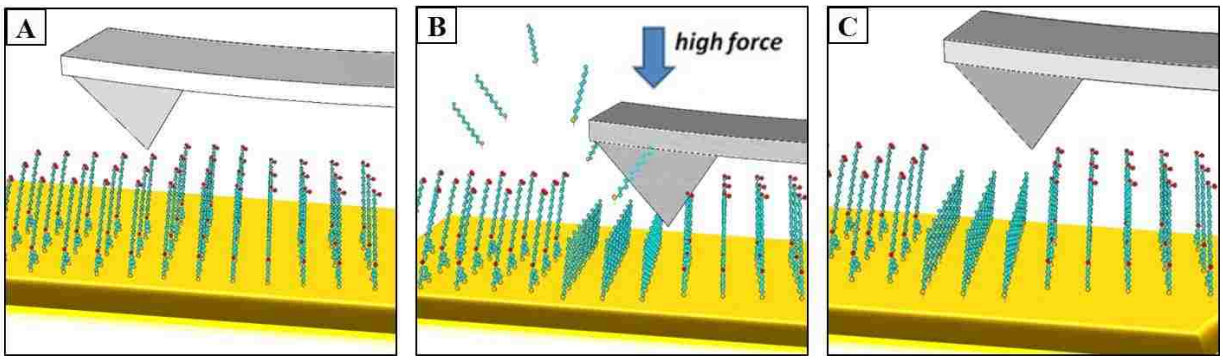

Figure 2.10 Steps of nanografting. *(a)* Surface characterization is accomplished under low force while imaging in a solution containing thiol molecules. *(b)* Nanografting is accomplished by increasing the force applied to the AFM tip, free molecules from solution assemble onto the exposed substrate. *(c)* Returning to low force, the nanografted patterns can be imaged with the same AFM tip.

When designing nanografting protocols, the analyst can choose from a range of commercially available thiol molecules with different lengths and head group chemistries.[36] An example is shown in Figure 2.11 of nanografted pattern with height that is higher than the matrix monolayer. The topography and corresponding lateral force images of a logo of Louisiana State University schematic are presented in Figures 2.11, a. and 2.11, b., respectively.

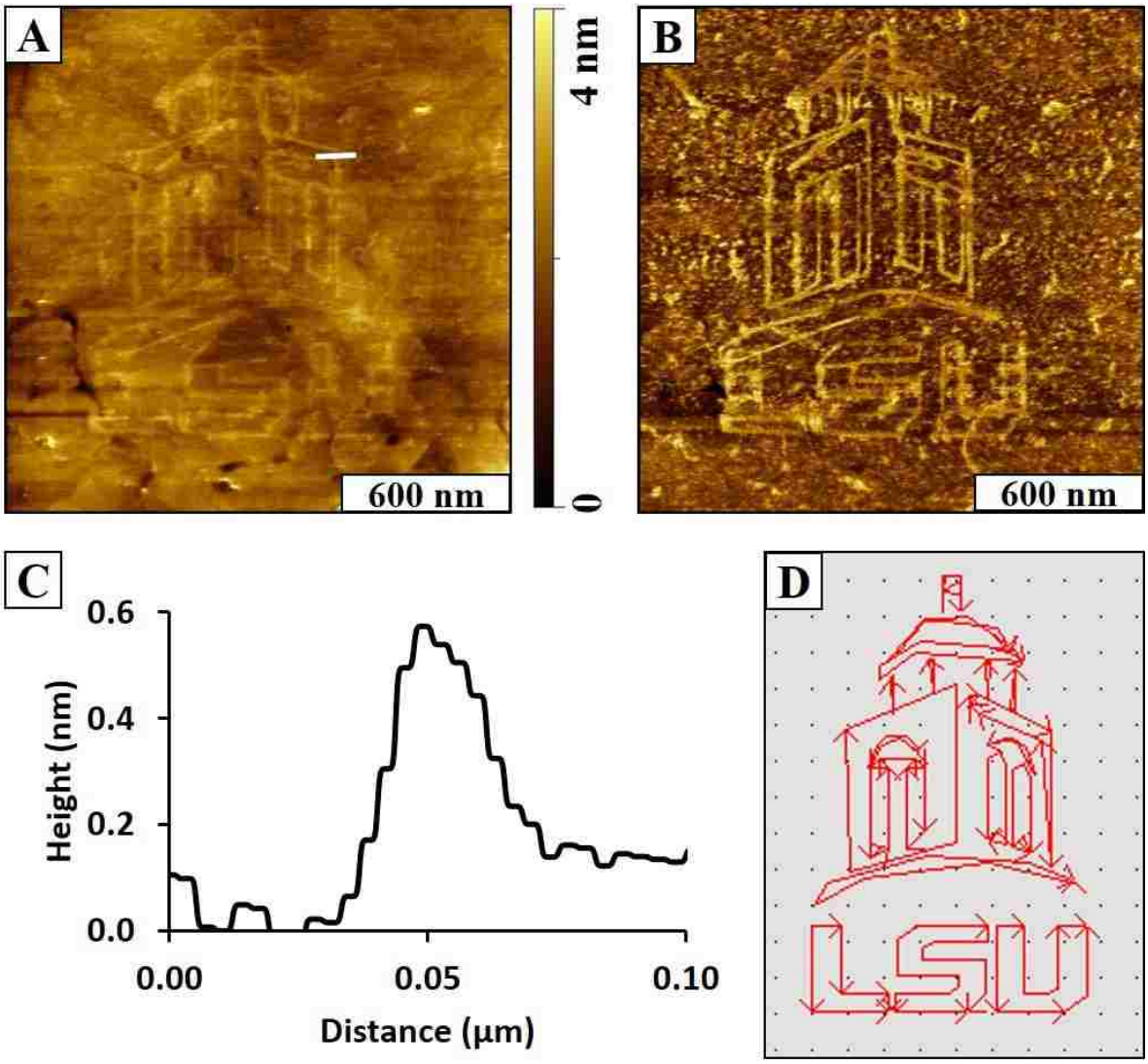

Figure 2.11 A nanoscale Louisiana State University logo written with 16-mercaptohexadecanoic acid within a 1-dodecanethiol SAM. *(a)* Contact mode AFM topography for a 1.8 ×1.8 μm^2 scan area; *(b)* corresponding lateral force image; *(c)* cursor profile of the line drawn in *(a)*; *(d)* design used for nanografting.

Terrace steps of the general morphology of an *n*-alkanethiol SAM on Au(111) are apparent in the topography frame. The lateral force image more prominently reveals the pattern design, because the headgroups of the patterned areas are chemically different than the matrix SAM which provides frictional contrast. The acid headgroups of the nanopatterns exhibit strong tip-surface adhesion, producing line spike artifacts in the topography frames. The differences in surface

chemistry between the nanografted patterns (carboxylic acid headgroups) and the dodecanethiol matrix SAM (methyl headgroups) provide excellent contrast for the lateral force image of Figure 2.11, b. The areas surrounding the pattern are methyl-terminated dodecanethiol and the patterns were written with carboxylic acid-terminated 16-mercaptohexadecanoic acid (MHA), which is 0.5 nm higher than the matrix SAM. The height difference of the two molecules can be measured with a local cursor measurement shown in Figure 2.11, c. The height of the MHA molecules on Au(111) measured 2.0 nm. The script used to outline the nanopatterns is shown in Figure 2.11, d., with excellent correspondence between the design and resulting nanografted patterns for such small size scales. The linewidth achieved for this pattern was accomplished with a single sweep, measuring 20 nm in width. With an ultra-sharp AFM probe, the smallest feature produced with nanografting was an island of a 2×4 nm^2 dot pattern, which is an area that would accommodate approximately 32 thiol molecules.[56]

2.6 Conductive-probe AFM

An early and important variation of AFM is conductive-probe AMF (CP-AFM),[57] also known as conducting (probe) AFM,[58-62] conductive AFM[63] and current sensing AFM.[64-66] It is applied for current mapping and measurement at the nanoscale in addition to the regular topographic mapping and force measurement with a metal-coated AFM tip. The basic instrumental setup of CP-AFM is shown in Figure 2.12. A regular AFM tip made from silicon or silicon nitride (Si_3N_4) is coated with a thin layer (ca. 15 – 100 nm) of metal as an electrode. The metal used for coating an AFM tip includes Au,[59, 63] Pt,[59, 61-62] Ti,[57] and Niobium nitride (NbN).[67] A conductive (e.g. Au and graphite) or semi-conductive (e.g. silicon wafer) substrates are used as the other electrode for measuring conductivities of the samples by applying a voltage between the conductive tip and the substrate. The current flow through the tested material is mapped simultaneously with the

topography image by the tip constantly contacting the sample during raster scan under a certain voltage and loaded force. The local conductivity of tested material can be drawn from current-voltage (I-V) curves, which are acquired by parking the conductive tip on a selected point of the sample and then recording the flow current during a voltage sweep.

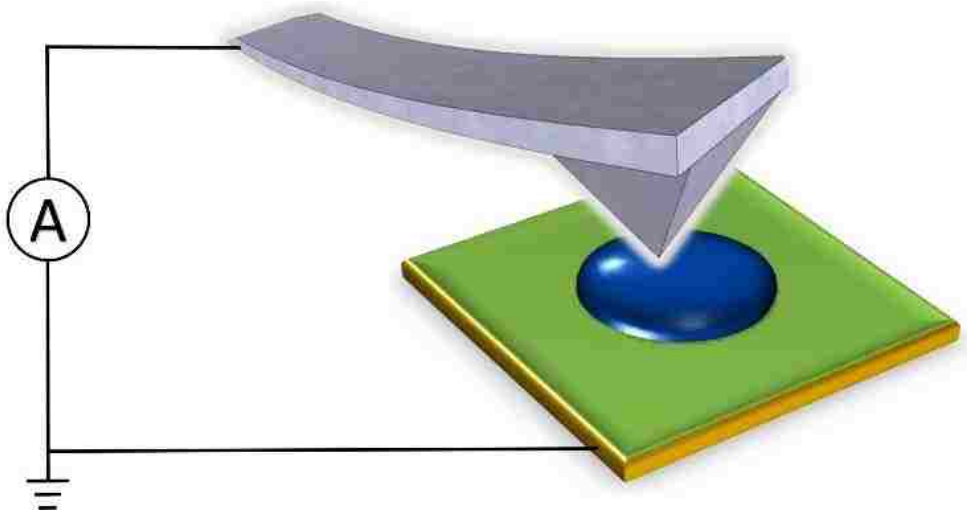

Figure 2.12 Instrumental setup for CP-AFM.

Since the first research using CP-AFM was published in 1993,[57] various materials have been characterized by this technique including metal-oxide-semiconductors (MOSs),[57-58, 60, 62, 65] nanotubes,[67-68] SAMs,[63, 66, 69-73] molecular wires,[61, 74] and polymers.[64, 75] The operating environment of CP-AFM can be in ambient conditions, gas phase, UHV and liquid.[59, 61] The liquid for CP-AFM imaging should be carefully selected. Dry toluene is a good choice for liquid CP-AFM imaging.[59, 61]

As an alternative SPM technique for measuring conductive properties at the nanoscale, an advantage of CP-AFM compared to non-contact STM is prevention of the effect of a tunneling junction from to collect I-V curves.[70-71] The direct contact between the conductive AFM probe and the sample simplify the interpretation of the electrical behavior owing to the absence of an additional tunneling gap. Another advantage of CP-AFM compared to STM is controlling the

mechanical load of the tip to the sample, which facilitates understanding the measured resistance or conductance.[61, 70] For STM experiments, there is no contact between the tip and sample.[61]

Example images acquired with CP-AFM are shown in Figure 2.13. An organic thin film with periodic array of nanopores was fabricated on template-stripped gold (TSG) using immersion particle lithography. As CP-AFM is operated in contact mode, using deflection as the feedback signal, topography and lateral force images are simultaneously acquired with current image of the

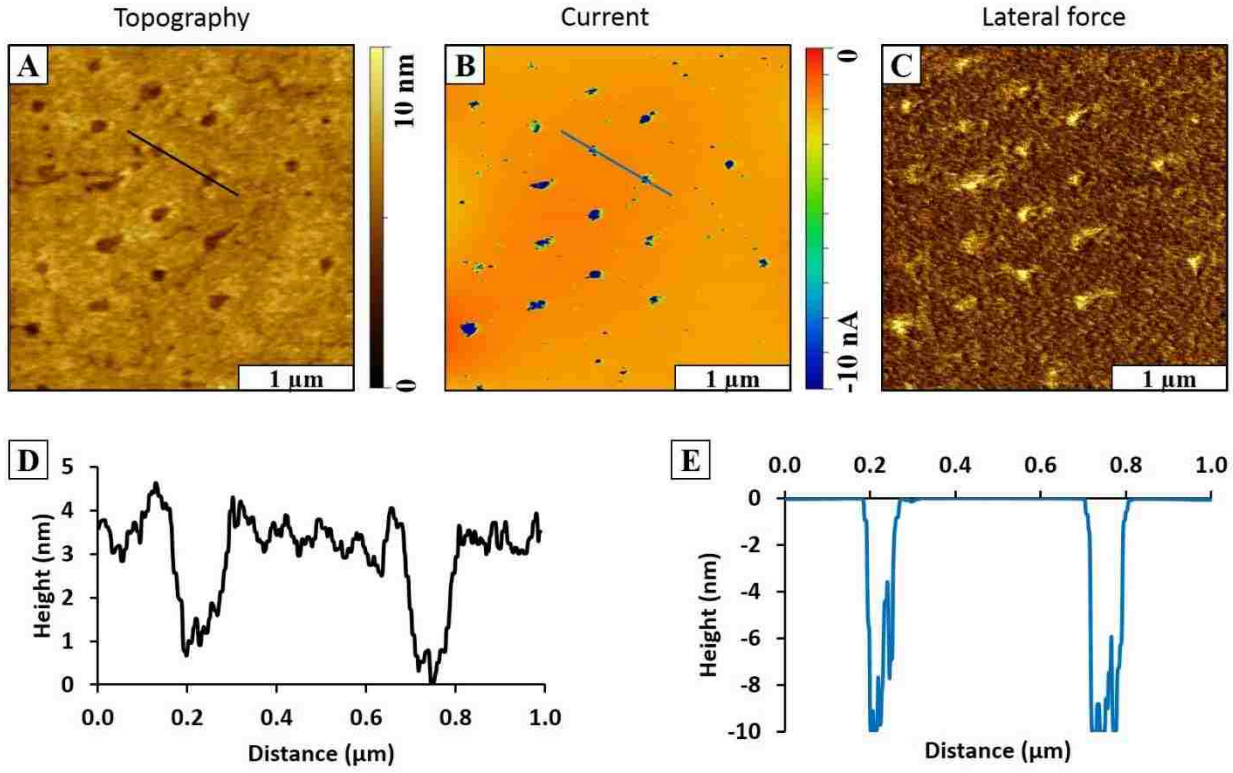

Figure 2.13 Simultaneously-acquired topography, current and lateral force images of patterned nanopores in an anisole thin film on Au(111) obtained with CP-AFM. *(a)* Topography image; *(b)* simultaneously acquired current image; *(c)* lateral force image; *(d)* height profile taken from two nanopores in topography image; *(e)* current profile taken from the same two nanopores in current image. (Sample courtesy: Ragains Group of Louisiana State University).

same scanned area. A representative topography image is shown in Figure 2.13, a. The periodic nanopores are shown as black circular dots in a hexagonal arrangement. The areas of the nanopores are bare Au(111) which were protected by mesospheres during formation of the organic thin film.

The defects of Au(111) surface such as scars can be observed at the background. The current image of the same scanned area is shown in Figure 2.13, b. The conducting Au areas are clearly shown as the blue dots correspond to the nanopores in the topography image. The insulating background shown with orange contrast indicates the resistivity of the organic thin film. In the lateral force image, shown in Figure 2.13, c., two distinct domains, i.e. bare Au(111) areas and organic thin film are presented as bright gold dots and dark brown background respectively. A representative cursor profile of height is shown in Figure 2.13, d., corresponding to the black line drawn in Figure 2.13, a. The thickness of the film is 3.5 ± 1 nm from the cursor profile. The distance of the two measured nanopores measured 500 nm, which is determined by the diameter of the mesospheres used as surface mask. A cursor profile of the current measured from the same two nanopores is shown in Figure 2.13, e. The Au(111) areas show the highest current values in contrast to the background organic layer, which shows high resistivity.

2.7 Self-assembled monolayers of organosulfur

Since R. G. Nuzzo and coworkers firstly reported the adsorption of organosulfur on gold surfaces in 1983,[76] alkanethiol molecules have been widely used to form self-assembled monolayers (SAMs) on metal surfaces for surface modification. Studies have shown that *n*-alkanethiol molecules are well ordered as a commensurate ($\sqrt{3}\times\sqrt{3}$)R30° lattice on Au(111) with backbones tilted approximately 30° from surface normal (Figure 2.14).[77-79] The application of 2D alkanethiol SAMs ranges from electronic devices to biosensor detection. The stability of organosulfur-based SAMs on noble metal surfaces is a concern which limits the reliability and durability of organic thin film materials.[80] A potential drawback of applications of *n*-alkanethiol SAMs is degradation due to ultraviolet (UV) light, heat, and oxidation.[80] Studies have shown that thiol SAMs formed with longer alkane chains are more thermally stable than those formed with

shorter chain lengths.[81-83] Improved stability for organosulfur SAMs on noble metal surfaces can be achieved by anchoring more than one sulfur group to the metal surface atoms to form multiple anchoring points for each molecule.[84] It has been reported that multidentate thiols improve the etch selectivity and increase the resist surface film quality, and the enhancement of stability originates from an entropy-driven chelate effect.[85] In an alkanethiol-gold system, the exchange of sulfur atoms on a gold surface is a dynamic process during surface assembly.[86] The formation of an initial sulfur-metal bond facilitates further bonding between other sulfur atoms to anchor multidentate thiol molecules on a gold surface. Studies using ellipsometry indicate that multidentate thiols have improved thermal stability compared to monodentate thiols.[87,88-89] Electrochemical studies have shown that SAMs from multidentate thiols exhibit greater stability.[90,91-92]

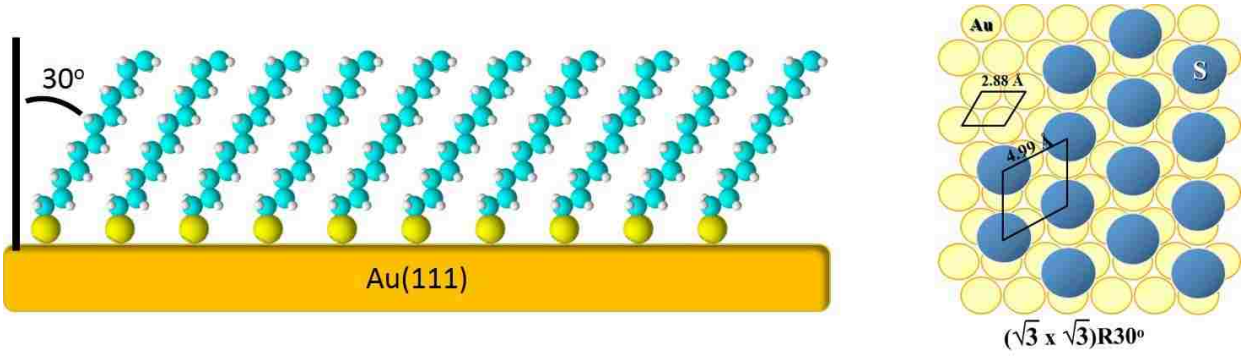

Figure 2.14 Model of *n*-alkanethiols SAMs on Au(111) surface.

2.8 Particle lithography

Particle lithography is an example of natural lithography. It provides a generic approach for high-throughput fabrication of nanopatterns with nanoparticles,[93-94] proteins,[26] metals,[95-97] and organic materials.[98-99] It is an inexpensive and rapid method for fabricating a large array of nanostructures. Nanolithography approaches which combine chemical synthesis with surface engineering can be applied for studying the effects of spatial confinement for surface-based

chemical reactions.[13, 99] With particle lithography, a dried film of latex or silica spheres is used as a surface mask to designate the placement of molecular adsorbates. After the deposition of a matrix material, the spheres are then removed either by sonication or lift-off, leaving behind hexagonal arrays on surfaces. The exquisite small areas used to be protected by the spheres are available for further spatially confined deposition or reaction of studied materials. Combining particle lithography with molecular self-assembly provides a practical strategy to prepare arrays of organic film-based nanostructures with regular geometries. Millions of nanopatterns can be generated using bench steps.

A close-packed arrangement of monodisperse silica or latex mesospheres is shown in the topography image in Figure 2.15, a. The close-packed mesospheres can be applied as a surface mask for nanolithography. The diameter of the mesospheres are 500 nm as shown in the cursor line profile (Figure 2.15, b.). The diameter of the mesosphere defines the periodicity of the patterned structures on surfaces.

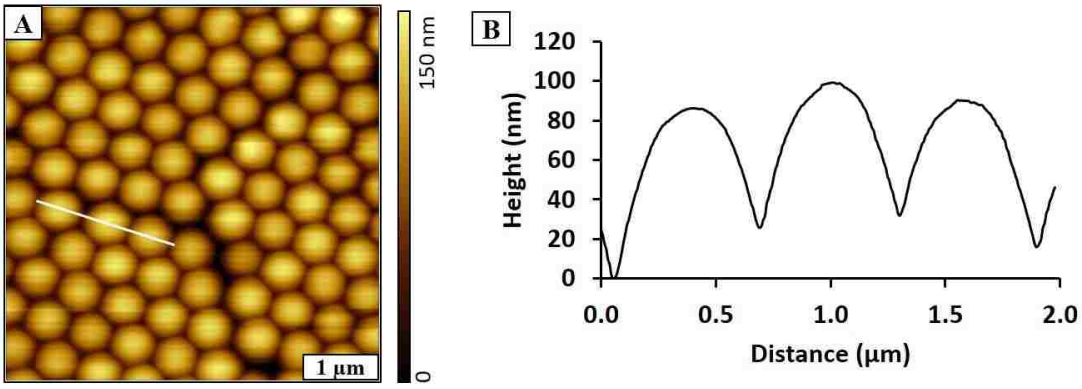

Figure 2.15 Mesosphere template of 300 nm latex used for particle lithography. *(a)* Hexagonal arrangement of the mesospheres is apparent in the AFM topography. *(b)* Height profile taken from the white line in *(a)*.

CHAPTER 3: NANOSCALE LITHOGRAPHY MEDIATED BY SURFACE SELF-ASSEMBLY OF 16-[3,5-BIS(MERCAPTOMETHYL)PHENOXY]HEXADECANOIC ACID ON AU(111) INVESTIGATED WITH SCANNING PROBE MICROSCOPY[3]*

3.1 Introduction

Considerable effort has been directed toward studies of monothiol-based self-assembled monolayers on gold; however, the surface self-assembly of multidentate thiol adsorbates has received far less attention, particularly at the molecular level. The stability of organosulfur-based adsorbates to oxidation, heat, and exposure to light can limit the durability of surface films.[100-109] Multidentate SAMs derived from thiol adsorbates exhibit enhanced thermal and chemical stability compared to those derived from *n*-alkanethiols.[107, 110] Having additional thiol moieties in the headgroup of these adsorbates enables a chelate effect, which improves the stability of the films.[111-112]

Previously, we investigated the surface self-assembly of tridentate 1,1,1-tris(mercaptomethyl)heptadecane with *in situ* studies using atomic force microscopy (AFM).[25] The adsorption of tridentate adsorbates proceeds via a more complex assembly pathway than that of monothiols since the multidentate molecules require successive steps to form S–Au bonds to the surface. The bidentate molecule selected for this study is 16-[3,5-bis(mercaptomethyl)phenoxy]hexadecanoic acid (BMPHA), shown in Scheme 3.1.[113] The design of BMPHA incorporates two thiol groups placed at *meta*- positions of a phenyl moiety, connected by bridging methylene groups. The distance between the two thiol groups (5 Å) was designed to place the two sulfur atoms at binding sites of Au(111) without substantial torsional strain.[100, 114]

* Chapter 3 previously appeared as Zhai, X.; Lee, H. J.; Tian, T.; Lee, T. R.; Garno, J. C., Nanoscale lithography mediated by surface self-assembly of 16-[3,5-bis(mercaptomethyl)phenoxy]hexadecanoic acid on Au(111) investigated by scanning probe microscopy. Molecules 2014, 19 (9), 13010-26. It is reprinted by permission of MDPI Publisher (see page 100).

The molecular backbone of BMPHA consists of a chain of sixteen carbons terminated with carboxylic acid. The acid moiety can be used as a linker moiety for binding proteins[115] or metals.[116] By changing immersion conditions, electrostatic interactions at the interface can produce head-to-head linkages of acid endgroups to form bilayer films.[117]

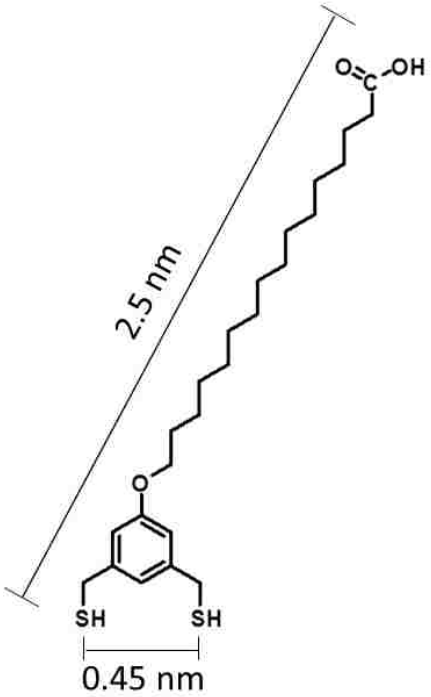

Scheme 3.1 Structure of 16-[3,5-Bis(mercaptomethyl)phenoxy]hexadecanoic acid (BMPHA).

Scanning probe based protocols of nanoshaving and nanografting have been applied to measure the local thickness of organic films,[117-119] for monitoring adsorption kinetics on surfaces,[38, 120] to identify functional groups of *n*-alkanethiols,[121-122] and to confine spatially the deposition of DNA,[123-124] proteins,[115, 125-126] and metals.[116] Nanofabrication based on scanning-probe methods requires steps of rastering the probe to write each pattern individually. A high-throughput approach for nanolithography with organic thin films has been developed that can generate billions of circular nanopatterns at once, using surface masks of close-packed

monodisperse mesospheres. Particle lithography enables the manufacture of billions of regular nanopatterns with well-defined geometries based on solution self-assembly and steps of drying and evaporation.[13, 127] Arrays of regularly-shaped nanostructures provide a foundation for further chemical reactions and are useful for local AFM characterizations. For example, the areas that were masked by mesospheres furnish exposed sites of Au(111) for depositing organothiols to generate multicomponent surface patterns with selected functional groups.

The synthesis of multidentate thiol-based adsorbates offers opportunities for generating robust interfaces of well-defined structure and composition. In our experiments, nanostructures of BMPHA were prepared with closed packed silica spheres on Au(111). Essentially, our strategy was to construct spatially-selective containers of exposed sites of the substrate to direct the subsequent deposition of a second molecule. Samples prepared by nanolithography with organic thin films enable side-by-side comparisons of the surface structures of multidentate adsorbates versus *n*-alkanethiol monolayers (i.e., film thickness, periodicity, surface properties). Surface characterizations were accomplished using *in situ* imaging with AFM to provide fundamental measurements at the molecular level. Scanning probe based lithography experiments employed a liquid sample cell for AFM studies, since fresh reagents can be introduced to the system and step-wise surface changes before and after nanofabrication can be monitored *in situ*. The multidentate SAMs provide a foundation for constructing more complex assemblies at the nanoscale. Side-by-side imaging of the surface structures of BMPHA versus *n*-octadecanethiol were accomplished with AFM. A bilayer of BMPHA was formed on Au(111) by changing the immersion conditions (i.e., concentration and immersion time). The thickness of monolayer and bilayer BMPHA thin films on Au(111) was evaluated by measurements with nanoshaving, nanografting and immersion protocols with particle lithography.

3.2 Materials and methods

3.2.1 Materials

Octadecanethiol was purchased from Sigma Aldrich (St. Louis, MO) and used as received. The new adsorbate of interest, 16-[3,5-bis(mercaptomethyl)phenoxy]hexadecanoic acid (BMPHA) was synthesized as previously reported.[113] Ethanol (200 proof) was obtained from Pharmco-AAper Alcohol and Chemical Co. (Shelbyville, KY) and used as the diluent for preparing thiol solutions. Gold pellets (99.99% purity) were purchased from Ted Pella (Redding, CA).

3.2.2 Preparation of organic thin films on Au(111)

To prepare films of BMPHA for scanning-probe based nanolithography protocols, commercially obtained gold substrates were rinsed with ethanol and submerged in thiol solutions for specifically designated immersion intervals. Films of BMPHA were rinsed with ethanol and then characterized with AFM with protocols of nanoshaving and nanografting. Flame-annealed gold films on mica substrates (150 nm thickness) were purchased from Agilent (Chandler, AZ).

3.2.3 Preparation of template-stripped Au(111)

Template-stripped gold (TSG) films on glass substrates were prepared as reported previously.[128] Gold pellets were deposited in a high-vacuum thermal evaporator (Angstrom Engineering Inc., Kitchener, OR) at 10^{-7} Torr onto freshly cleaved pieces of Ruby muscovite mica (S&J Trading Inc., Glen Oaks, NY). The mica was preheated to 350°C prior to gold deposition using quartz lamps mounted behind the sample holder. A deposition rates of 3 Å/s was used to prepare films of 150 nm overall thickness. After deposition, the gold substrates were annealed at 365°C under vacuum for 30 min and cooled to room temperature. The gold film was glued to glass slides as previously reported by Hegner et al.[129] The gold substrates and glass slides were rinsed with deionized water and placed into a UV-ozone generator for 30 min. Epoxy (EPO-TEK,

Billerica, MA) was mixed (1:1) and immediately deposited onto the glass slides. The glass slide was placed onto the gold surface so that the drop of epoxy formed a thin film without any air bubbles. The samples were then heated in oven at 150°C for 2 h to anneal the epoxy. After cooling to room temperature, the glass pieces were carefully peeled from the mica to form TSG.

3.2.4 Immersion particle lithography with masks of silica mesoparticles

Size-sorted, monodisperse silica mesospheres (500 nm diameter, Thermo-Fisher Scientific, Waltman, MA) were deposited on TSG as surface masks for immersion particle lithography. Aqueous solutions of silica mesospheres were cleaned by centrifugation to remove surfactants or contaminants. A volume of 300 μL of the silica mesosphere solution was placed into a microcentrifuge tube and centrifuged for 20 min at 20,000 rpm. A solid pellet formed at the bottom of the centrifuge tube, and the supernatant was removed and replaced with deionized water. The pellet was resuspended with deionized water by vortex mixing. The washing cycle was repeated four times. Freshly-stripped pieces of TSG were cleaned by rinsing copiously with ethanol. A drop (10–15 μL) of the mesosphere solution was deposited onto the TSG substrates and dried under ambient conditions to form surface masks for nanolithography. The mesosphere masks were annealed by heating at 150°C for 12 h; the heating step enabled the masked substrates to be immersed in solvent solutions for preparing films on TSG. The mesospheres could be removed in a later step by sonication in ethanol. Further details for the procedure of particle lithography with immersion are described with Appendix D.

3.2.5 Atomic force microscopy

Models 5500 and 5420 scanning probe microscopes (Agilent Technologies, Chandler, AZ) equipped with PicoView v1.12 software were used for AFM characterizations. Images were acquired using contact mode in a liquid cell containing ethanolic solutions. Imaging and

nanofabrication were accomplished with silicon nitride tips with an average spring constant of 0.6 N/m (Bruker Instruments, Camarillo, CA). A scan rate of 1 line/s with a typical image force less than 1 nN were used for AFM imaging. A liquid cell made from polycarbonate was used for nanoshaving and nanografting experiments. Digital images were processed and analyzed with Gwyddion v. 2.30.[130]

3.2.6 Scanning probe-based nanolithography (nanoshaving and nanografting)

Nanoshaving and nanografting experiments with SAMs were done as previously described.[28, 131] To accomplish nanoshaving, the probe is swept multiple times across a small region with a higher mechanical force applied to the AFM tip. The sweeping action of the probe is used to remove or displace molecules of the matrix SAM. The area can be characterized *in situ* using the same probe by returning to low force for nondestructive AFM imaging. The amount of force that is required and the number of times needed to cleanly sweep an area needs to be evaluated for each experiment, depending on the sharpness of the probe. Nanoshaving can be done in either ambient air or in a liquid environment. In air, the molecules are displaced to form piles at the edges of the nanoshaved patterns. In liquid media, the shaved molecules can be swept away to produce clean edges at the sides of nanopatterns. Nanografting is accomplished in a liquid environment that contains the selected molecules for patterning. A single sweep of the selected area at high force is used to remove molecules of the matrix SAM simultaneously as molecules from solution self-assemble onto uncovered areas of the substrate. Returning to low force for *in situ* imaging the nanografted patterns can be characterized using the same AFM probe. The fabrication step of nanografting is depicted in Figure 3.1. Advantages of nanoshaving and nanografting are that a liquid environment enables *in situ* studies of surface changes with high

resolution. The nanopatterns that are produced in the fabrication steps can be imaged under low force with the same AFM tip as a tool for imaging and nanofabrication.

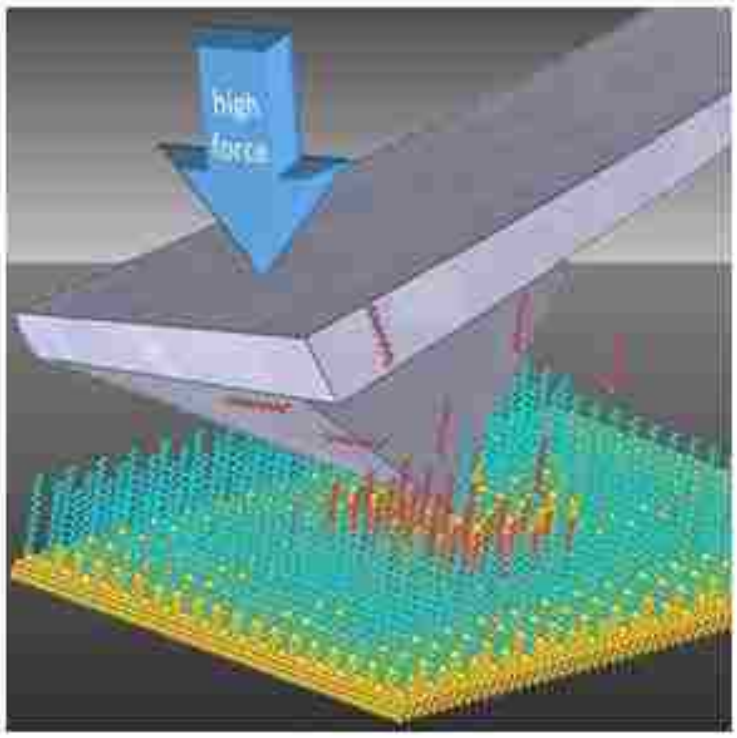

Figure 3.1 Operation of an AFM probe under force to accomplish nanografting.

3.3 Results and discussion

Several protocols with scanning probe microscopy were conducted to investigate the self-assembly and surface morphology of BMPHA on Au(111) in a liquid environment. Our goal was to obtain side-by-side views of the morphology of BMPHA and *n*-alkanethiols films using AFM characterizations of grafted nanopatterns. The known height of *n*-octadecanethiol (ODT) was used as a nanoscale ruler to evaluate the thickness of BMPHA films prepared under selected conditions. Depending on the concentration and immersion intervals, either single or double layers of BMPHA could be generated.

3.3.1 Nanoshaving within a monolayer film of BMPHA

A square nanoshaved pattern (200×200 nm^2) within a SAM of BMPHA is shown in Figure 3.2. The BMPHA film of the matrix area surrounding the nanoshaved hole was formed by 24 h immersion in 0.1 mM solution. The nanoshaved area is the dark square in the topography image (Figure 3.2, a.) and reveals the underlying gold substrate. The irregularly shaped bright patches at the top and bottom of the nanoshaved square are residues of BMPHA removed by the AFM probe. To assess how effective the nanoshaving parameters were for removal of BMPHA, the simultaneously acquired lateral force image is shown in Figure 3.2, b. The bright area of the square nanopattern located at the center of the image indicates the exposed areas of the substrate, which indicates clean removal of BMPHA. The tip-surface interactions mapped in lateral force frames are distinct for the gold surface and carboxylic endgroups of BMPHA. The thickness of the BMPHA film can be evaluated with a local cursor measurement, referencing the uncovered area of the substrate as a baseline at the bottom of the nanoshaved square pattern (Figure 3.2, c.). The thickness of the BMPHA SAM measured 2.0 ± 0.2 nm, which is in close agreement with the value obtained by ellipsometry.[113] A conservative error term of 0.2 nm is reported due to the roughness of the underlying gold substrate, which is based on the height of a single gold terrace step.

Compared to monodentate *n*-alkanethiols, a higher force was required to shave away the multidentate BMPHA layer. For the example in Figure 3.2, the area was swept 20 times with 5 nN applied force. Typically, *n*-alkanethiols can be nanoshaved with 4-6 sweeps at forces between 0.2 and 10 nN depending on the sharpness of the AFM probe. When nanoshaving *n*-alkanethiol SAMs in ethanol, the displaced molecules are often dissolved in the surrounding liquid media so that no residues are present at the edges of the patterns. However, with the bidentate example shown in Figure 3.2, BMPHA molecules formed aggregate assemblies that failed to dissolve fully in

ethanolic media. Intermolecular associations between the carboxylic acid groups and π-π interactions of the aromatic moiety of BMPHA are sufficiently strong to induce aggregation, as indicated by surface residues at the edges of the nanoshaved pattern.

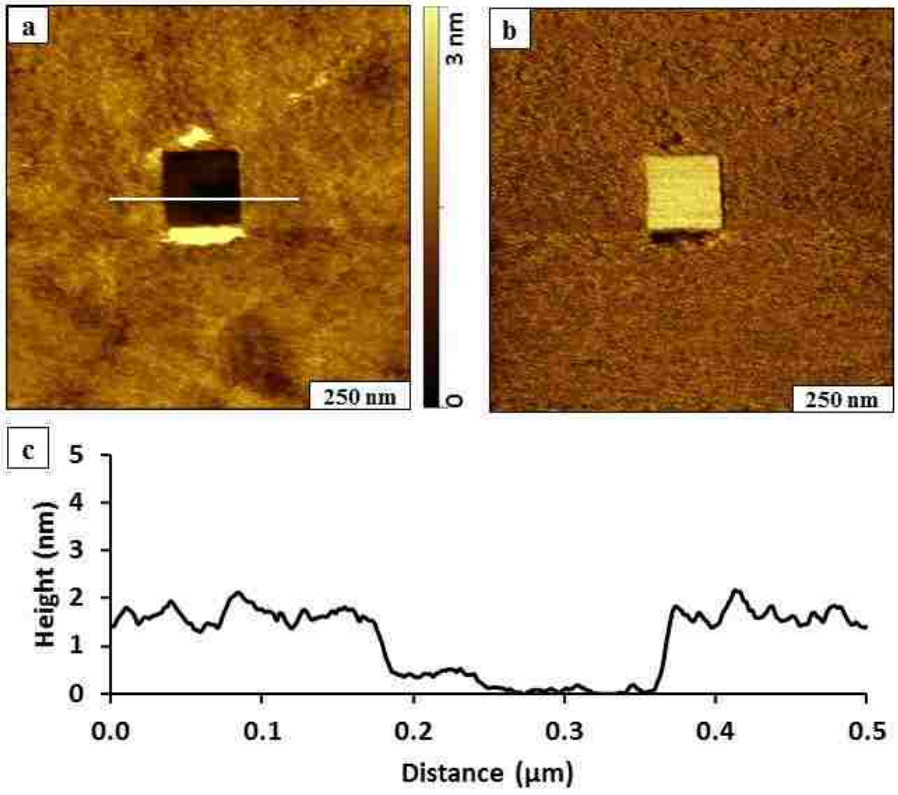

Figure 3.2 Nanoshaving within a BMPHA monolayer. *(a)* Topography view of nanoshaved square; *(b)* corresponding lateral force image; *(c)* height profile for the white line in *(a)*.

3.3.2 Nanografting n-alkanethiols within a monolayer of BMPHA

The thickness and quality of the bidentate BMPHA films were examined further using protocols of nanografting. Films of BMPHA were prepared on Au(111) by immersing a gold substrate into an ethanolic solution (0.1 mM) for 24 h. A nanopattern of *n*-octadecanethiol (ODT) was inscribed within a matrix of BMPHA (Figure 3.3) to enable a side-by-side comparison of the surface morphology. The nanopattern of ODT appears to be slightly shorter in height than the

surrounding areas of BMPHA (Figure 3.3, a.) revealing a recessed square region containing overlapping gold steps. The concurrently acquired lateral force image (Figure 3.3, b.) reveals distinct changes in the surface chemistry for the regions of the ODT nanopattern and BMPHA matrix. The horizontal lines are produced by the left and right raster pattern of the AFM probe. The expected height for a densely packed ODT monolayer is 2.1 nm, assuming a tilt angle of 28°. Residues of BMPHA are piled at the edges of the nanografted pattern and provide a distinct boundary around the inscribed region of ODT; therefore, comparison of the height differences at the pattern edges cannot be used to provide a reliable estimate of the BMPHA film thickness for this example. Comparing the cursor measurement in areas beyond the edges of the nanopattern reveals that the thickness of the BMPHA film is approximately the same as ODT, which would correspond to a monolayer.

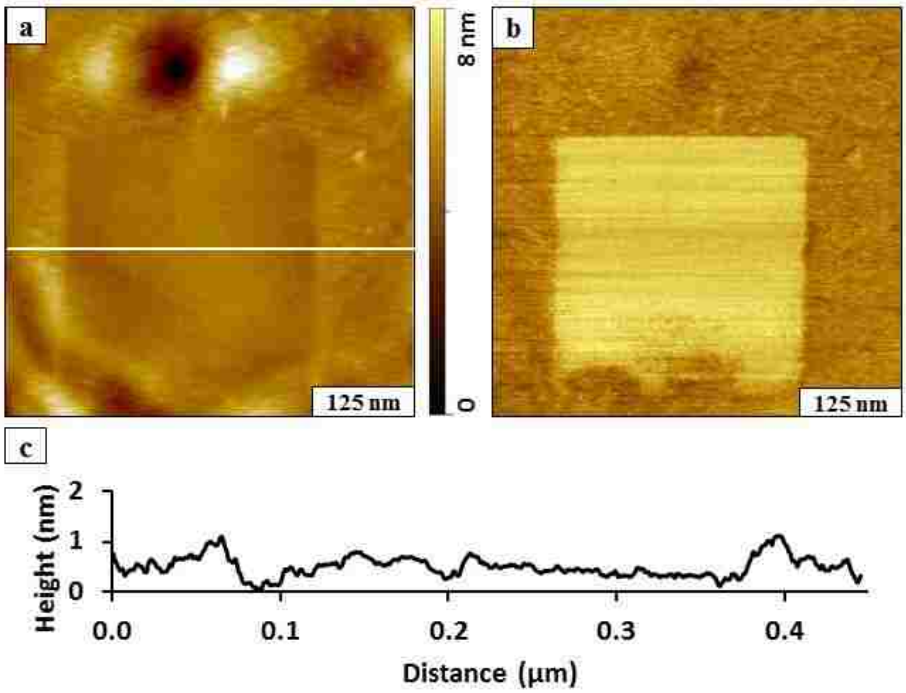

Figure 3.3 Side-by-side comparison of the surface morphology of ODT and a BMPHA monolayer prepared on Au(111). *(a)* Nanografted pattern of ODT (300 × 300 nm^2) viewed with a contact-mode AFM topography image acquired in ethanol; *(b)* corresponding lateral force image; *(c)* cursor profile for the line in (*a).*

The areas of BMPHA appear to have a rougher morphology in the areas surrounding the nanografted ODT pattern (Figure 3.3, a.). A few small adsorbates are present on the BMPHA areas, and the density of BMPHA is consistent with a loosely packed tailgroup assembly.[31] The differences in tip-surface adhesive interactions are quite distinct in the lateral force image of Figure 3.3, b. A monolayer of BMPHA would present carboxylic acid moieties at the surface, whereas the nanopattern of ODT is terminated with methyl groups, which produces distinct changes in color contrast for the lateral force frame.

Protocols of nanoshaving and nanografting can be accomplished within the same experiment by rinsing and exchanging solutions with the AFM liquid sample cell. This protocol requires a stable imaging environment, since it is easy to perturb the sample to displace the tip away from the nanofabricated region. In the next *in situ* experiment, a 200 × 200 nm^2 square of BMPHA molecules was nanografted within a naturally grown BMPHA SAM (Figure 3.4). The nanopattern can be vaguely distinguished near the center of the image, because the bottom corners of the pattern did not fill in completely. Otherwise, the height of the nanografted area matches the height of BMPHA and is not visible in the topography frame. After nanografting, the BMPHA solution was removed and replaced with clean ethanol to enable nanoshaving. A square area (200 × 200 nm^2) was swept at high force to disclose the underlying gold substrate at the left side of the image. The nanoshaved area is easy to distinguish as a dark square at the left side of the topography frame of Figure 3.4, a. Although mostly indistinguishable, the square pattern of BMPHA was nanografted immediately to the right of the nanoshaved pattern. The area in the center of the pattern with a nanografted pattern of BMPHA has the same surface chemistry (-COOH) as the surrounding matrix and cannot be clearly detected in the lateral force image (Figure 3.4, b.). However the nanoshaved square on the left side of the frame is readily identifiable with brighter color.

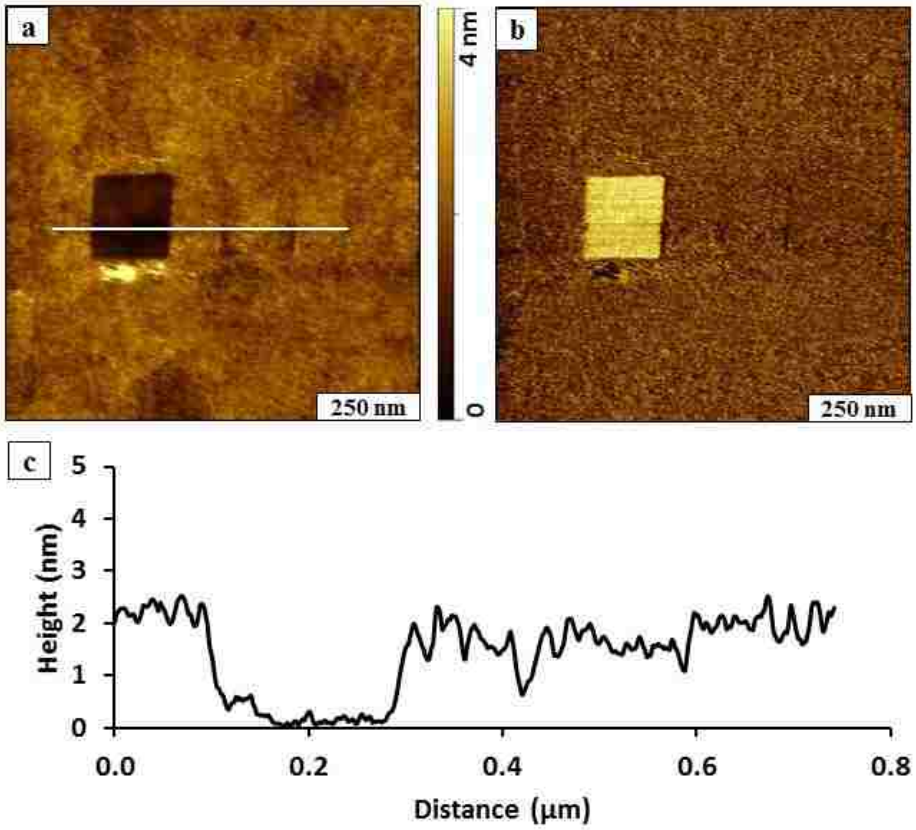

Figure 3.4 Fabrication of a nanoshaved square and nanografted pattern of BMPHA side-by-side within a monolayer film of BMPHA. *(a)* Contact-mode topography image acquired in ethanol; *(b)* lateral force frame; *(c)* cursor profile for the line in (*a)* drawn across both nanopatterns.

Combining protocols of nanografting followed by nanoshaving is particularly useful to test if the nanografting solution interacts to bind to the surface of the matrix layer. A representative line profile across the nanoshaved area of Figure 3.4, a. shows that the thickness of the film measures 2.1 ± 0.2 nm, referencing the bottom of the nanoshaved area as a baseline (Figure 3.4, c.). This thickness corresponds to the expected height for a monolayer of BMPHA; consequently, there is no evidence of adsorption of the nanografting solution to the BMPHA matrix. For the nanografted area, no difference in height was detected for the nanografted patch of BMPHA versus the surrounding BMPHA film. This area can be detected using the vague dark outline of the bottom

corners of the nanografted square. Considering the overall theoretical molecular length of BMPHA (2.53 nm); the tilt angle for a BMPHA monolayer would measure ~34 degrees, assuming that both sulfurs of the bidentate molecule bind to the surface of gold.

3.3.3 Nanografting ODT within a double layer of BMPHA

A double layer film of BMPHA on Au(111) can be produced by changing the experimental parameters of concentration and immersion intervals. A bilayer of BMPHA was formed by immersion of a gold substrate in 5 mM ethanolic solution for 30 h. Nanopatterns were fabricated within a BMPHA bilayer using sequential steps of nanoshaving and nanografting prepared as shown in Figure 3.5. First, a rectangular area (200 × 300 nm^2) was nanoshaved within the BMPHA film. Next, a solution of ODT (1 mM) was injected into the sample cell, and a smaller rectangle was nanografted to the right of the original nanoshaved area. At this concentration, we were unable to detect the growth of ODT within the nanoshaved area over a period of less than one hour. For the rectangular nanopattern on the right side of Figure 3.5, a., an aggregate of residue removed from the nanoshaved area persists near the bottom of the rectangle. The nanografted pattern of ODT has a taller mound of removed adsorbates at the top edge of the feature. Differences in surface adhesion are mapped in the lateral force frame of Figure 3.5, b., revealing different color contrast for the matrix of BMPHA, the nanoshaved area, the nanografted ODT pattern, and adsorbate residues. The patterns exhibit different depths within the BMPHA matrix, as shown with a representative line profile in Figure 3.5, c. The nanofabricated areas have heights that are shorter than the surrounding BMPHA film. The thickness of the BMPHA matrix film measured using the depth of the nanoshaved rectangle is 4.2 ± 0.2 nm, which corresponds to a bilayer. The difference in thickness for the nanografted pattern on the right measured 2.1 ± 0.2 nm, which is consistent

with the known thickness for a monolayer of ODT. Additional examples of nanoshaved and nanografted patterns produced within a BMPHA bilayer are provided in Appendix D. (Figure D1).

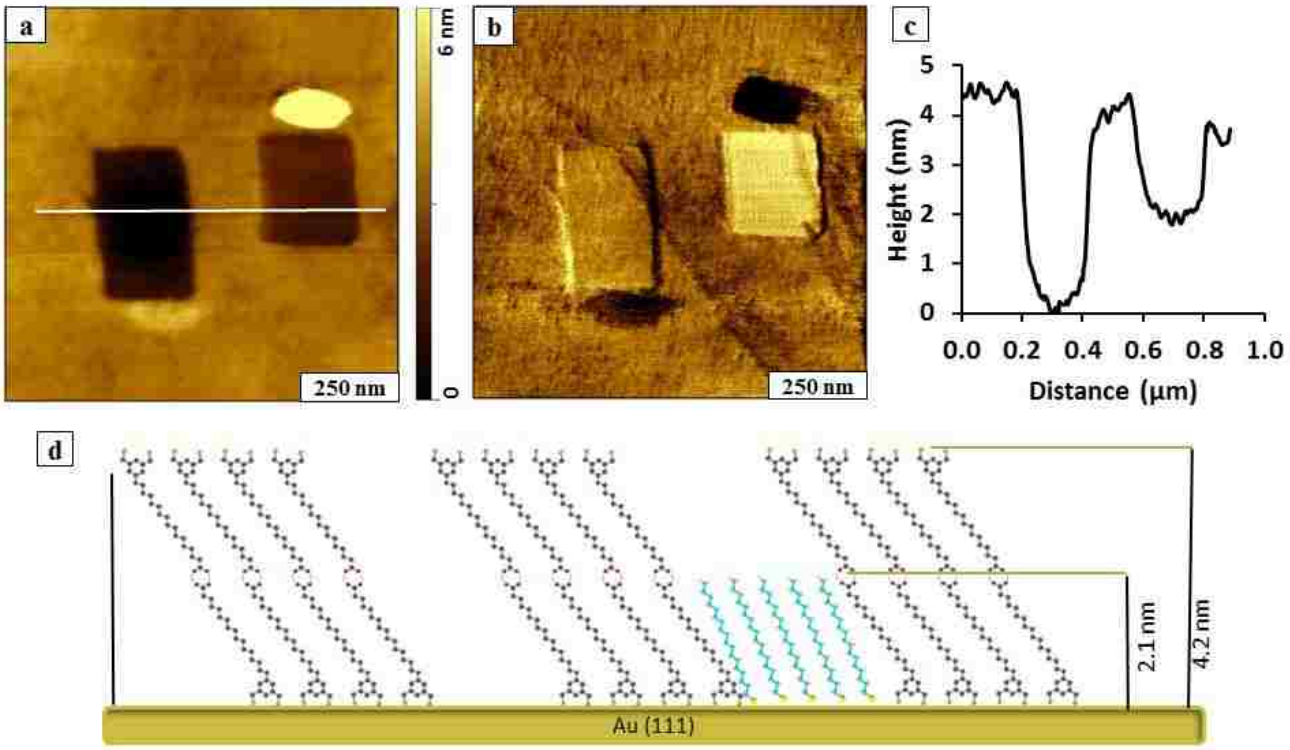

Figure 3.5 A nanoshaved area and nanografted pattern of ODT placed side-by-side within a BMPHA bilayer. *(a)* Topography image; *(b)* lateral force frame; *(c)* cursor profile for (*a)*; *(d)* proposed height model.

A model for the heights of the nanoshaved and nanografted patterns is presented in Figure 3.5, d. In the proposed model, a bilayer is formed by interactions between –COOH functional groups of BMPHA to form a head-to-head arrangement. Previously, double layers were detected with extended immersion or higher concentrations of acid-terminated *n*-alkanethiol SAMs, such as 11-mercaptoundecanoic acid and mercaptohexadecanoic acid.[117] For this model the bilayer of BMPHA presents dithiol moieties at the interface. Notably, no BMPHA bilayer structures were

observed when the SAMs were formed from 1 mM ethanolic BMPHA followed by *ex situ* rinsing with water, THF, and ethanol.

3.3.4 Nanofabrication experiments with BMPHA using immersion particle lithography

Using immersion particle lithography, periodic arrangements of nanostructures were produced through surface self-assembly of BMPHA and ODT on gold. Solution self-assembly of thiol-based molecules on gold substrates enables construction of thin films with well-defined dimensions and composition. Particle lithography enables exquisite design of interfacial chemistry by defining the surface coverage of component molecules.[127, 132] For protocols with BMPHA, a mask of mesospheres was placed on template-stripped gold (TSG). Two immersion steps were used to prepare islands of ODT within a matrix monolayer of BMPHA. In the first immersion step, the masked TSG substrate was submerged in an ethanolic solution of BMPHA to prepare nanoholes. When the mesosphere mask was removed, a periodic arrangement of uncovered areas of substrate is disclosed (Figures 3.6, a.-3.6, c.). The nanoholes were filled in by a second immersion step with ODT (Figures 3.6., d-3.6, f.). This protocol produced circular islands of methyl-terminated ODT surrounded by a matrix monolayer of acid-functionalized BMPHA.

Representative AFM images of samples prepared with the two immersion steps are presented in Figure 3.6; the top panels are views of the nanoholes within BMPHA produced by particle lithography, and the bottom panels were acquired for the same sample after backfilling with ODT. A periodic arrangement of nanoholes is shown in Figure 3.6, a.; the dark circles of the topography frame are areas of uncovered substrate and can be more clearly distinguished in the lateral force frame (Figure 3.6, a'.). There are approximately 25 nanoholes within the $3 \times 3\ \mu m^2$ area, which would scale to an approximate surface density of 10^8 nanostructures/cm^2. The spacing between nanopatterns measures 500 nm, matching the diameter of the silica mesospheres used for

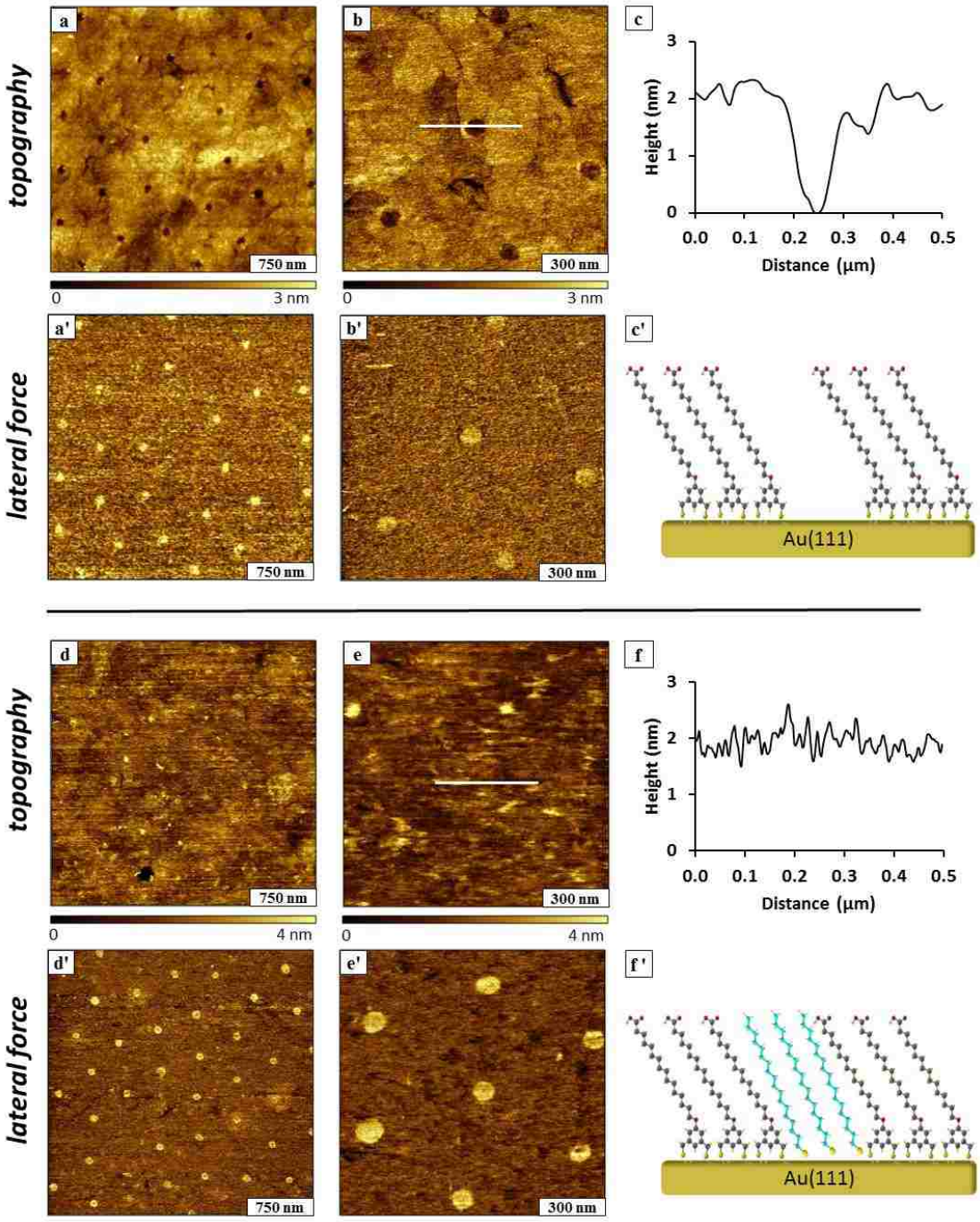

Figure 3.6 Nanopatterns prepared with ODT and BMPHA using immersion particle lithography. *(a)* Nanoholes within BMPHA; *(a')* lateral force image; *(b)* successive zoom-in topograph; *(b')* lateral force image; *(c)* cursor profile for the line shown in ***b***; *(c')* structural model of BMPHA nanostructures. *(d)* Nanoholes filled with ODT; *(d')* corresponding lateral force frame; *(e)* zoom-in view of ODT nanopatterns; *(e')* lateral force image; *(f)* cursor profile for the line in (*e*); *(f')* chemical model of backfilled ODT within BMPHA.

patterning. With immersion particle lithography, the sizes of the nanoholes are exquisitely small because the areas where the beads make physical contact are much smaller than the periodicity of the mesosphere surface mask. The shape of the nanoholes is more clearly revealed in zoom-in views of Figures 3.6, b. and 3.6, b'. Six sites of nanoholes are shown within the 1.2 × 1.2 μm^2 frame, defining the areas where the mesospheres were displaced. The topography frames also resolve the shapes of the edges of steps and terraces of the gold substrate beneath the BMPHA film. The depth of the nanoholes measures 2.1 ± 0.2 nm, shown with a representative cursor profile in Figure 3.6, c. A side-view model for a monolayer of BMPHA with areas of uncovered gold is shown in Figure 3.6, c'.

The nanoholes were backfilled with ODT by immersing the sample in a solution of 1 mM ODT in ethanol for 24h. Changes in surface morphology are readily apparent after backfilling, the locations of the circular holes are no longer visible in the topography frames of Figures 3.6, d and 3.6, e. Since ODT and BMPHA are similar in height, there is no clear height difference revealed in the topographs, as shown with an example cursor profile in Figure 3.6, f. However, the simultaneously acquired lateral force frames disclose distinct differences in color contrast for the –COOH groups of BMPHA compared to methyl-terminated ODT. Lateral force images enable visualization of the locations and sizes of the ODT nanopatterns in Figures 3.6, d'. and 3.6e'. Using the lateral force frames, the surface coverage of methyl and acid headgroups was determined to be ~5%.

Immersion particle lithography was similarly applied for making islands of ODT within a bilayer film of BMPHA (Figure 3.7). The bilayer was produced by using higher concentration of 4 mM BMPHA immersed for 30 h. Approximately 60 nanoholes of uncovered TSG are visible within a BMPHA bilayer for a 5 × 5 μm^2 area, as shown in Figures 3.7, a. and 3.7, a'. The diameter

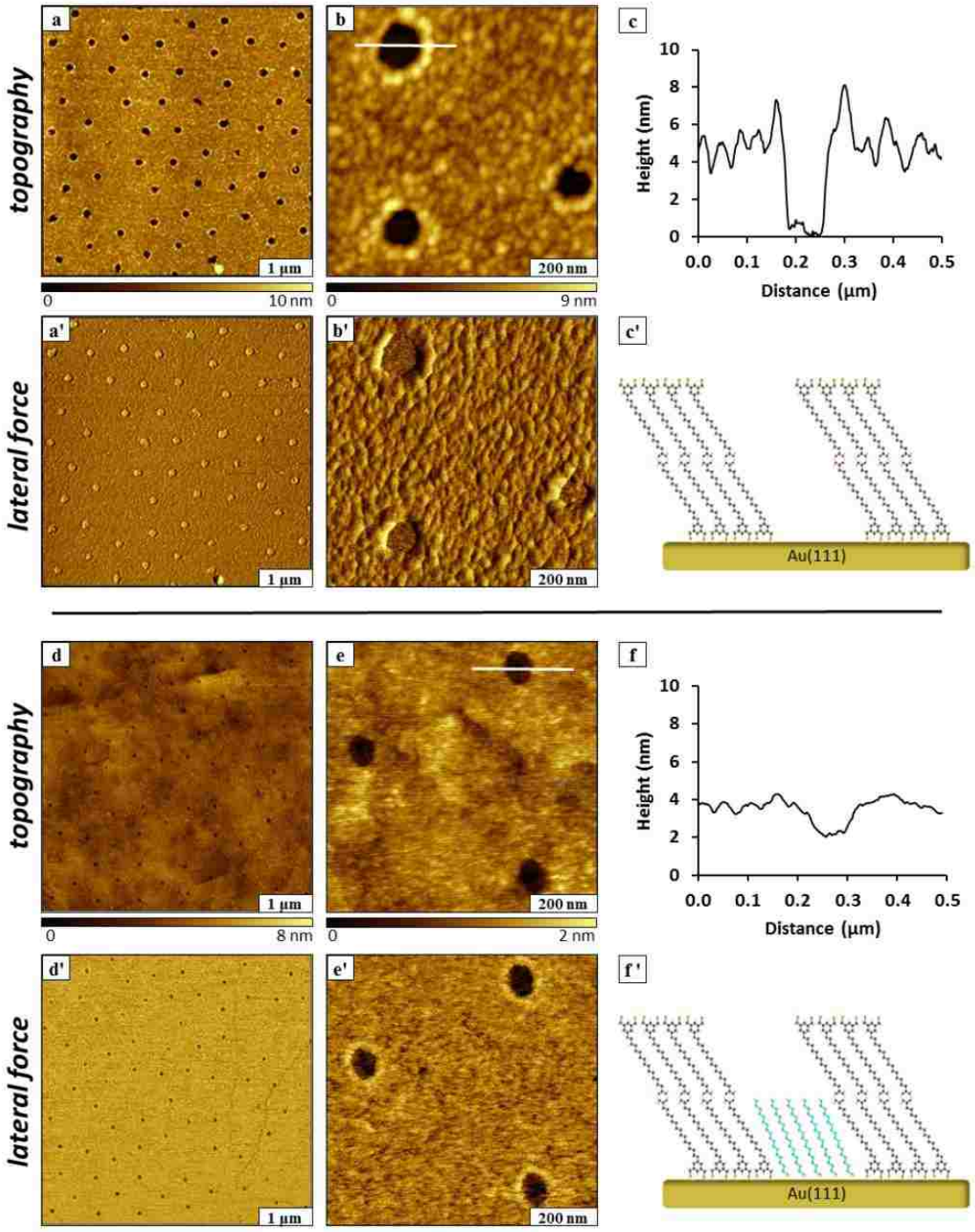

Figure 3.7 Nanopatterns prepared in a bilayer of BMPHA using immersion particle lithography. *(a)* Nanoholes exposing TSG within a BMPHA bilayer; *(a')* corresponding lateral force image; *(b)* zoom-in view; *(b')* lateral force image; *(c)* cursor profile for the line shown in ***b***; *(c')* chemical model of BMPHA bilayer. *(d)* Nanoholes filled in with ODT; *(d')* corresponding lateral force frame; *(e)* zoom-in view of ODT backfilled nanopatterns; *(e')* lateral force image; *(f)* cursor profile for the line in (*e)*; *(f')* chemical model of backfilled ODT within a bilayer of BMPHA.

of the nanoholes measures 110 ± 10 nm, with a surface coverage of 5%. A close-up view of three nanoholes is shown in Figures 3.7, b. and 3.7, b'., revealing a somewhat rougher texture at the surface of the BMPHA bilayer. The reference features of the underlying gold substrate cannot be distinguished in Figure 3.7, b. as was apparent for the monolayer film of BMPHA (Figures 3.7, a. and 3.7, b.). One might predict that a bilayer film would be less densely packed than a monolayer, and the surface morphology revealed in Figure 6, b. indicates that the packing density of the BMPHA bilayer has changed in comparison to a monolayer film. The depth of nanoholes formed within the BMPHA was measured to be 5.0 ± 1.2 nm (Figure 3.7, c.). This distance is slightly longer than expected for a double layer of BMPHA, possibly attributable to adsorbates on the surface of the bilayer. A model of the side-view of the BMPHA bilayer is presented in Figure 3.7, c'., showing head-to-head interactions between carboxylic acid groups that associate to form the double layer structure.

After backfilling the nanoholes with ODT, the patterns still appear as holes within the matrix film of the BMPHA bilayer (Figures 3.7, d. and 3.7, e.). Images shown in the lower half of Figure 3.7 were acquired after 24 h immersion in 1 mM ODT in ethanol. The rougher texture of the BMPHA bilayer appears to be smoother because of additional steps of rinsing and sonication to remove loose adsorbates. Features of the underlying gold substrate such as step edges can be vaguely resolved for areas of the BMPHA bilayer in the zoom-in view of Figure 3.7, e. Chemical maps of the areas of nanopatterns with methyl headgroups are provided by the lateral force images (Figures 3.7, d'. and 3.7, e'.). The depth of backfilled nanoholes within BMPHA multilayer was measured to be 1.8 ± 0.2 nm (Figure 3.7, f.), which closely matches the expected difference in thickness between a BMPHA bilayer and ODT. The measurement of nanopattern depths

extrapolates to a local thickness of 3.9 ± 0.2 nm for a BMPHA bilayer. The proposed model for the height of the double layer pattern is shown in Figure 3.7, f'.

3.4 Conclusions

Protocols for AFM-based nanolithography as well as immersion particle lithography were used to evaluate the morphology and thickness of bidentate BMPHA on Au(111). The established thickness of monodentate ODT was used as a reference for *in situ* measurements of film thickness. Either monolayer or bilayer films of BMPHA can be formed on Au(111) by controlling the parameters of solution concentration and the duration of immersion in ethanolic solution. The thickness of monolayer films of BMPHA measured 2.0 ± 0.2 nm, which is consistent with previous measurements reported using ellipsometry. Assuming that both thiols of BMPHA bind to gold, this value would correspond to a tilt angle of 34° from the surface normal. Head-to-head dimerization between interfacial carboxylic groups can produce bilayers of BMPHA, as has previously been demonstrated for *n*-alkanethiols with carboxylic acid groups. Both monolayer and bilayer films of BMPHA could be generated using immersion particle lithography. Periodic island nanopatterns of ODT were grown within nanoholes of BMPHA, constructed with a successive step of sample immersion in SAM solution. Future directions for this research will be to develop protocols to compare the long-term stability of bidentate versus monodentate structures using nanofabricated test structures.

CHAPTER 4: CONDUCTIVE-PROBE MEASUREMENTS WITH NANODOTS OF FREE-BASE AND METALLATED PORPHYRINS

4.1 Introduction

As potential building blocks of the miniaturized electronics, the conductive properties of porphyrin assemblies are relevant for potential applications. The well-developed synthetic routes can be employed to design the molecular structure of porphyrins, such as the placement and nature of the substituents and central metal ions.[133-137] Porphyrins have been investigated as potential building blocks in miniaturized electronics and photovoltaics.[68, 138-141]

Investigations of the conductivity of porphyrins have focused mainly on single molecules using scanning tunneling microscopy (STM).[142-147] However, conductive probe-atomic force microcopy (CP-AFM) has become a practical tool for characterizing the conductive properties of organic films and assemblies in ambient conditions.[145, 148-154] Early studies focused on applying CP-AFM to detect the conductivity of thiol self-assembled monolayers (SAMs).[61, 154-156] An advantage of using CP-AFM to measure the conductive properties of organic films in comparison to STM studies is to avoid the effect of the gap between the tip and the sample.[154, 157] For AFM measurements, the tip is placed in direct contact with the sample, whereas STM measurements are made in non-contact mode, with the probe located a short distance from the sample. With AFM, a metal coated AFM probe is used as the top electrode which is placed at defined locations to record current-voltage (I-V) curves, while maintaining a controlled contact force and area between the tip and the sample.

Among studies of the conductive properties for porphyrins, nanorods, nanowire and nanotubes were successfully synthesized and characterized.[133, 158-162] Studies of the conductivity of porphyrin nanorods were reported by Schmab, et al.[161, 163] Meso-tetrakis(4-sulfonatophney) porphine ($TPPS_4$) was used to form nanorods with a well-defined height of 3.8 ± 0.3 nm and

lengths ranging from 0.2 to 2 μm. The photoconductivity of the nanorods formed with $TPPS_4$ was characterized using an electrometer. The conductivity of nanorods of $TPPS_4$ was studied using scanning tunneling microscopy in a UHV environment by Friesen, et al.[162] The charge-carrier mobility of multiple wire-like porphyrin nanostructures formed with octaethylporphyrin containing selected metals was investigated by So, et al.[164] The conductivities of zinc(II) metalloporphyrins were evaluated using single-wall carbon nanotubes for conductive probe atomic force microscope (CP-AFM) measurements by Tanaka, et al.[68]

A limitation for improving the sensitivity of scanning-probe based conductive measurements is the availability of well-defined test platforms of sample materials. Porphyrins are difficult to pattern, because when assembled on surfaces the molecules do not form chemisorbed or covalent bonds with metal substrates. Rather, porphyrins tend to self-associate and bind together in a stacked arrangement to form overlapping layers of molecules to adopt a coplanar, physisorbed configuration on surfaces.[165-166] Emerging practical approaches for preparing regularly shaped nanostructures with particle lithography have been demonstrated with organothiols and organosilanes.[13, 167] We have developed a strategy to use alkanethiol nanopatterns prepared by particle lithography to spatially confine and define the locations for porphyrin deposition.

For approaches based on particle lithography, samples can be prepared with a surface mask of monodisperse latex or silica mesospheres. After the particles are removed, exposed sites of the substrate are available for further steps of chemical reactions.[167-169] Combining solution immersion with particle lithography provides a practical strategy to prepare arrays of porphyrin nanostructures. Millions of nanopores can be generated within organothiol or organosilane SAMs.[3, 26, 96, 170] The nanopores provide a spatially-confined nano-sized container for depositing porphyrins. The array of porphyrin nanodots enable multiple test structures for reproducible CP-

AFM measurements. A Pt coated AFM tip serves as the top electrode and the Au(111) substrate is the bottom electrode for measuring the conductivity through the nanodots. Methyl-terminated dodecanethiol was used as a resistive matrix surrounding the nanodots, minimizing non-specific adsorption over areas between nanopores.

In this report, CP-AFM was used to measure the conductivity of porphyrin nanodots prepared within a resistive matrix of dodecanethiol on Au(111). The molecules selected are 5,10,15,20-tetraphenyl-21H,23H-porphyrin cobalt(II) (TPC) and 5,10,15,20-tetraphenyl-21H,23H-porphyrin (TPP), as symmetric model structures of free-base and metallated porphyrins.

4.2 Materials and methods

4.2.1 Materials

Reagents such as 5,10,15,20-tetraphenyl-21H,23H-porphine cobalt(II) (TPC), 5,10,15,20-tetraphenyl-21H,23H-porphine (TPP) ,1-dodecanethiol and dichloromethane were purchased from Sigma Aldrich (St. Louis, MO) and used as received. Ethanol (200 proof) was obtained from Pharmco-AAper Alcohol and Chemical Co. (Shelbyville, KY) and used as the diluent for preparing solutions of alkanethiols. Dichloromethane was purchased from Sigma Aldrich (St. Louis, MO) for dissolving porphyrins. Gold pellets (99.99% purity) were purchased from Ted Pella (Redding, CA). Ruby muscovite mica was purchased from S&J Trading Inc., (Glen Oaks,NY).

4.2.2 Preparation of porphyrin solutions

To prepare porphyrin solutions for making patterns of nanostructures on substrates, TPC and TPP were dissolved in dichloromethane (10^{-3} M) and then diluted with ethanol to a concentration of 10^{-7} M. Samples of each porphyrin were prepared by immersing the substrate in dilute solutions for 30 h.

4.2.3 Preparation of template-stripped Au(111)

The process for preparing template-stripped gold (TSG) is described in a previous publication.[3] A thin layer (150 nm) of gold was thermally deposited onto mica at 10^{-7} Torr using a high-vacuum thermal evaporator (Angstrom Engineering Inc., Kitchener, OR). Freshly cleaved Ruby muscovite mica was preheated to 350°C prior to gold deposition using quartz lamps at the back of the sample holder. The gold pellets were thermally evaporated and deposited onto mica at 10^{-7} Torr with a deposition rate of 3 Å/s. After deposition, the gold films were annealed at 365°C in vacuum for 30 min and then cooled to room temperature before removal from the deposition chamber. The method for mechanical stripping was previously described by Hegner et al.[129] First, the gold substrates and glass slides were cleaned with deionized water and placed into a UV-ozone generator for 30 min. Epoxy (EPO-TEK, Billerica, MA) was applied onto the cleaned glass slides and then attached onto the gold to make a glass-gold-mica "sandwich." The sample was then heated in oven at 150°C for 2 h to anneal the epoxy. After annealing, the glass pieces were carefully peeled from the mica to produce TSG with atomically flat surfaces.

4.2.4 Preparation of Porphyrin Nanostructures using Immersion Particle Lithography

The nanopore templates within thiol self-assemble monolayers (SAMs) were made with the procedures described previously.[3] Surface masks for immersion particle lithography were made by depositing monodisperse silica mesospheres (500 nm diameter, Thermo-Fisher Scientific, Waltman, MA) onto freshly stripped TSG. For cleaning the mesospheres, 300 μL of a suspension of silica mesospheres was transferred into a plastic microcentrifuge tube and centrifuged for 20 min at 20,000 rpm. A solid pellet of the mesospheres formed at the bottom of the centrifuge tube. The supernatant was decanted and then deionized water was added to the centrifuge tube for rinsing. The mesospheres were resuspended into deionized water by vortex mixing. The rinsing

step was repeated four times. A volume of 15 μL of the mesosphere suspension was deposited onto TSG and dried in ambient conditions to form surface masks. Before immersing into thiol solutions, the surface masks were placed into an oven at 150°C for 12 h. This step is important for preventing the silica mesospheres from being displaced the substrate when immersed in solution. The samples were cooled to room temperature (25°C), then immersed into a 10^{-3} M ethanolic dodecanethiol solution for 24 h. Dodecanethiol SAMs formed on the exposed areas of the TSG surfaces around the areas protected by the mesospheres. Next, the mesospheres were removed in a subsequent step by sonication in ethanol. Nanopores were fabricated within a matrix film of dodecanethiol. The center-to-center spacing between the nanopores matches the diameter of the mesosphere masks (i.e. 500 nm). In the final step, the nanopores were submerged into a 10^{-7} M solution of TPC or TPP in dichloromethane/ethanol (1:10000 vol.) for 30 h to produce porphyrin nanodots. Samples were rinsed with ethanol and dried under argon. The uncovered areas of Au(111) that had been masked by mesospheres provided well-defined surface sites for directing the subsequent attachment and growth of porphyrin nanodots.

4.2.5 Atomic force microscopy

A 5420 scanning probe microscopy (Keysight Technologies, Santa Rosa, CA) installed with PicoView v1.12 software was used for scanning probe studies. Images were acquired using tapping mode in ambient conditions. Imaging was accomplished with rectangular shaped, ultrasharp silicon tips that have an aluminum reflex coating, with a spring constant of 48 N/m (Nanoscience Instruments, Phoenix, AZ). The scan rate was 1 line/s. Electrical measurements on porphyrin nanodots were performed with the same instrument equipped with conductive nose assembly (0.1 nA/V sensitivity) and a conductive sample plate. Conductive tips with platinum

coating (PPP-CONTPt, Nanosensors, Neuchatel, Switzerland) were used to acquire I-V curves. Gwyddion v. 2.32 was used to process and analyze the digital images.[130]

4.3 Results and discussion

Porphyrins with and without a central metal ion were patterned, 5,10,15,20-tetraphenyl-21H,23H-porphyrin (TPP) and 5,10,15,20-tetraphenyl-21H,23H-porphyrin cobalt(II) (TPC) using steps of solution immersion of a gold substrate masked with silicon mesospheres. Protocols for patterning porphyrin nanodots and nanorods on Au(111) were based on immersion particle lithography. Individual nanodots of porphyrins were spatially isolated into well-defined, nanoscale arrangements within a templating film of a nanopatterned thiol monolayer with particle lithography. The nanodots of TPP and TPC are attached to areas of gold substrate, surrounded by an insulating film of dodecanethiol. Nanopores within a methyl-terminated alkanethiol matrix were filled with porphyrin nanodots by immersing the substrates with dodecanethiol nanopatterns into solutions of TPP or TPC. The porphyrin nanodots were not completely monodisperse, and exhibited sufficient differences in dimensions at the nanoscale to enable size-dependent I-V measurements.

4.3.1 Substrates with dodecanethiol nanopatterns formed on Au(111)

Example images of the arrangement of nanopores within a matrix of dodecanethiols are presented in Figure 4.1. Broad regions of the sample exhibit areas of uncovered circles of gold in a periodic arrangement. A methyl-terminated self-assembled monolayer (SAM) formed surrounding the 500 nm mesospheres on Au(111) after 20h immersion into a solution of dodecanethiol. When the surface mask of 500 nm mesospheres was rinsed away nanopores within dodecanethiol were generated as shown in Figure 4.1.

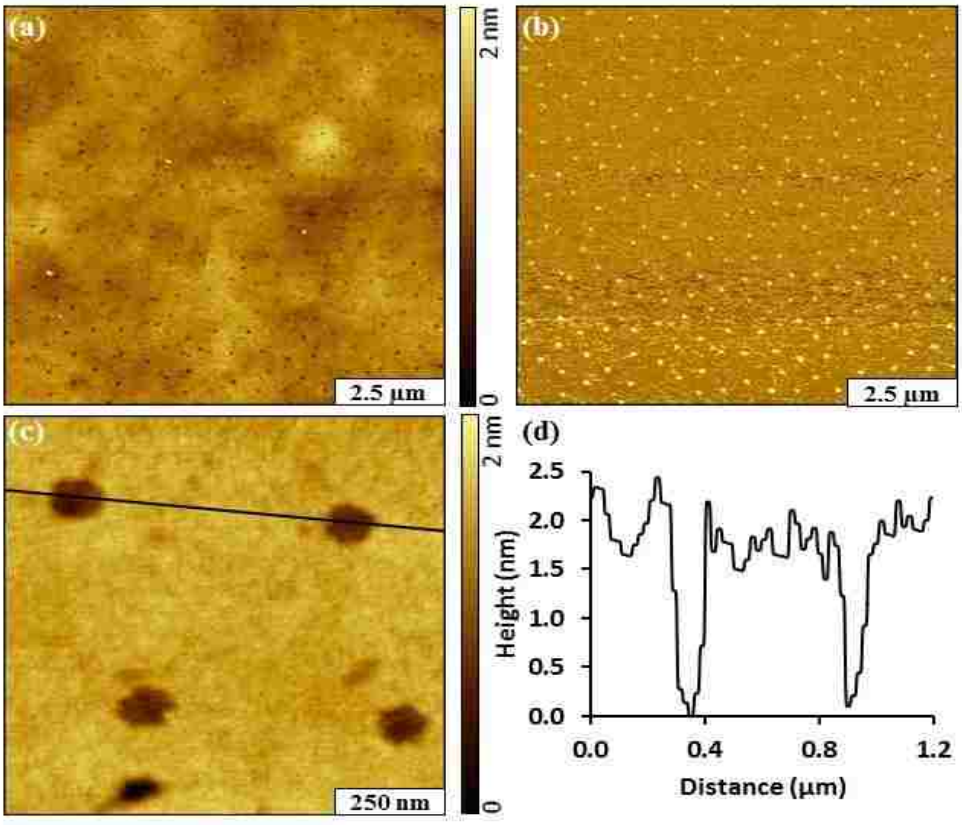

Figure 4.1 Nanopores within dodecanethiol formed on Au(111). *(a)* Topography and *(b)* corresponding phase image; *(c)* zoom-in view; *(d)* cursor profile for the line in (*c).*

A periodic arrangement of nanopores is observed throughout areas of the sample in Figure 4.1, a. The nanopores arrange in a hexagonal pattern reflecting the way the mesospheres arranged on surface. The periodicity of the nanopores measures 500 nm, which corresponds to the size of the silica mesospheres used as surface mask. Within a 10 × 10 μm^2 frame, there are 223 nanopores scaling to a surface density of 10^8 nanopores/cm^2. The overall area of the uncovered nanopores measured ~1 % of the entire frame. The differences in surface chemistry between the nanopores and surrounding matrix are evidenced with the simultaneously acquired phase image (Figure 4.1, b.). Brighter contrast indicates the region of uncovered gold substrates within the nanopores. The actual shapes of the nanopores is revealed in a zoom-in view (Figure 4.1, c.). Circular shaped

nanopores provide a template area for further steps of patterning TPP and TPC. The depth of the holes measured 1.7 ± 0.2 nm, shown with a representative cursor profile in Figure 4.1, d.

4.3.2 Nanopatterned dots of porphyrin

The areas of uncovered gold substrate within the methyl-terminated thiol SAM were used as nano-sized containers to deposit TPP and TPC. Millions of nanostructures on the surface test platforms enable the evaluation of the reproducibility of multiple measurements, as well as the visualization of whether the sample was damaged by electrical pulses during I-V measurements. The morphologies of the nanostructures formed either by TPP or TPC were characterized by tapping mode AFM in ambient conditions. Dot-like surface structures of porphyrins formed primarily within the nanopores, indicating that the methyl-terminated SAM was an effective resist.

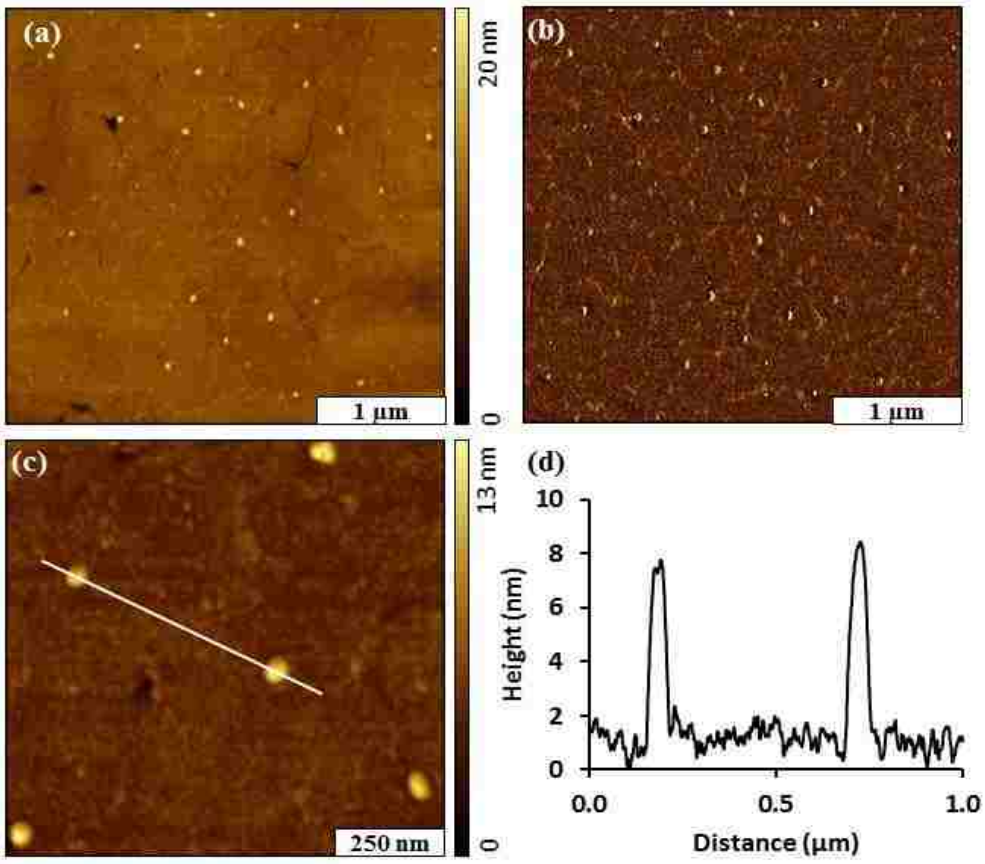

Figure 4.2 Nanodots of TPP within dodecanethiol (representative views). *(a)* Topography and *(b)* corresponding phase image; *(c)* zoom-in view; *(d)* height profile across two nanodots in (*c).*

An array of nanodots of TPP (Figure 4.2) was formed by immersion of a nanopore template in 10^{-7} M solution for 30 h. The TPP nanodots are arranged in a hexagonal pattern with a few areas of missed nanopores. A few defects of gold substrate under the thiol SAM are resolved in the broader areas of the topography image of Figure 4.2, a. At the nanoscale, characteristics of the Au(111) substrate such as roughness, scars and gold terraces affect the packing of the mesospheres used for particle lithography to create a few defects. The distance between neighboring nanodots measure 500 nm, which is the diameter of the silica spheres used for particle lithography. Further details of the size, placement and shapes of the TPP nanodots are presented in the corresponding phase image (Figure 4.2, b.). A close-up of the nanodots is viewed in the topography image of Figure 4.2, c. The nanodots measure in 8 nm in height and are spaced 500 nm apart (Figure 4.2, d.). The nanostructures provide an excellent test platform for further studies with conductive probe AFM, because there are multiple, isolated nanocrystals for replicate measurements.

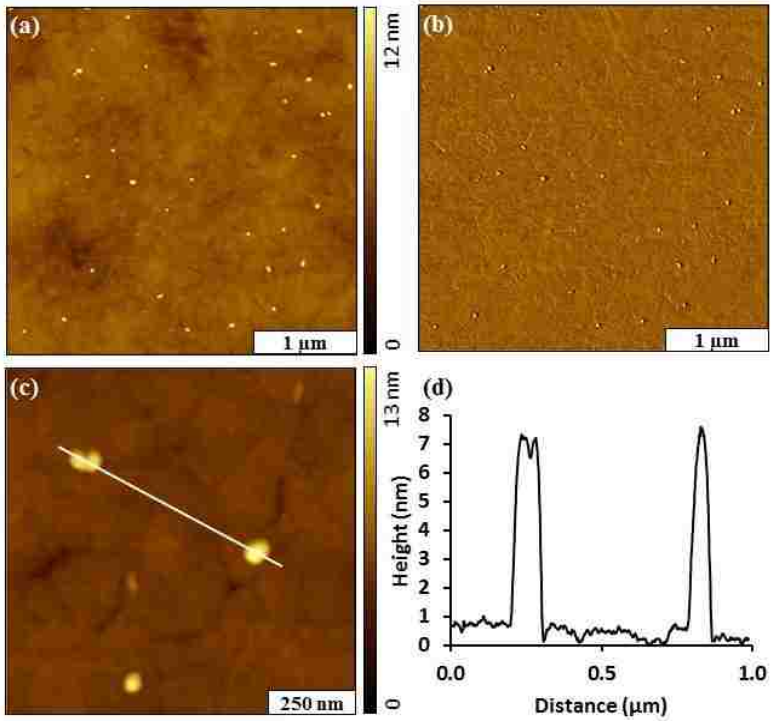

Figure 4.3 Nanodots of TPC within dodecanethiol. *(a)* Topography and *(b)* corresponding phase image; *(c)* zoom-in view; *(d)* height profile across two nanodots in (*c).*

An array of TPC nanodots also was formed by immersion of a nanopatterned dodecanethiol/Au template in a 10^{-7} M solution of TPC for 30 h. The overall shapes and surface arrangement of TPC nanodots is indistinguishable from that of the TPP sample. Nanodots of TPC formed inside the nanopores (Figure 4.3), and mostly did not assemble on the areas of dodecanethiol. The distance between neighboring nanodots measures 500 nm, which is the diameter of the silica mesospheres used to fabricate the dodecanethiol template. The selectivity of the TPC binding to the areas of the nanopores is evident in the simultaneously acquired phase image (Figure 4.3, b.). The areas of dodecanethiol appear to be free of adsorbates or nanoparticles. The detailed morphology of a few TPC nanodots is shown in Figure 4.3, c. The example nanodots measure 7 ± 0.5 nm in height (Figure 4.3, d.).

Within the same sample, the sizes of the TPP and TPC nanodots are slightly polydisperse, at the nanoscale. This is because the surface template of nanopores within dodecanethiol was not perfect at such small dimension. Slight imperfections in the sizes of the mesospheres or substrate defects cannot be perfectly controlled at the scale of less than 10 nm. The sizes of nanodots formed by TPP or TPC are compared in Figure 4.4. The average height of the TPP nanodots measured 6.4 ± 1.5 nm while the TPC nanodots measured 7.4 ± 3.1 nm. With a two sample t-test, the heights of the TPP and TPC nanodots are not significantly different with equal viabilities. The thickness of the nanodots measured ~ 7 nm, indicating multiple layers of porphyrin were deposited within the nanopores. The dimensions correspond approximately to 3-5 layers or stacks of porphyrins in a coplanar arrangement. The methyl-terminated areas of the surrounding matrix of dodecanethiol provide an effective resist layer, minimizing the non-specific adsorption of porphyrins in areas surrounding the nanoholes. Porphyrins have a planar structure that tends to bind to flat surface in a stacked arrangement, with the macrocycle of the molecules oriented parallel to the substrate. The

nature of surface attachment is physisorption, which is a relatively weak attachment for nanopatterning protocols. There are strong π-π interactions that drive macrocycles to bind together in a stacked arrangement, like a stack of coins.

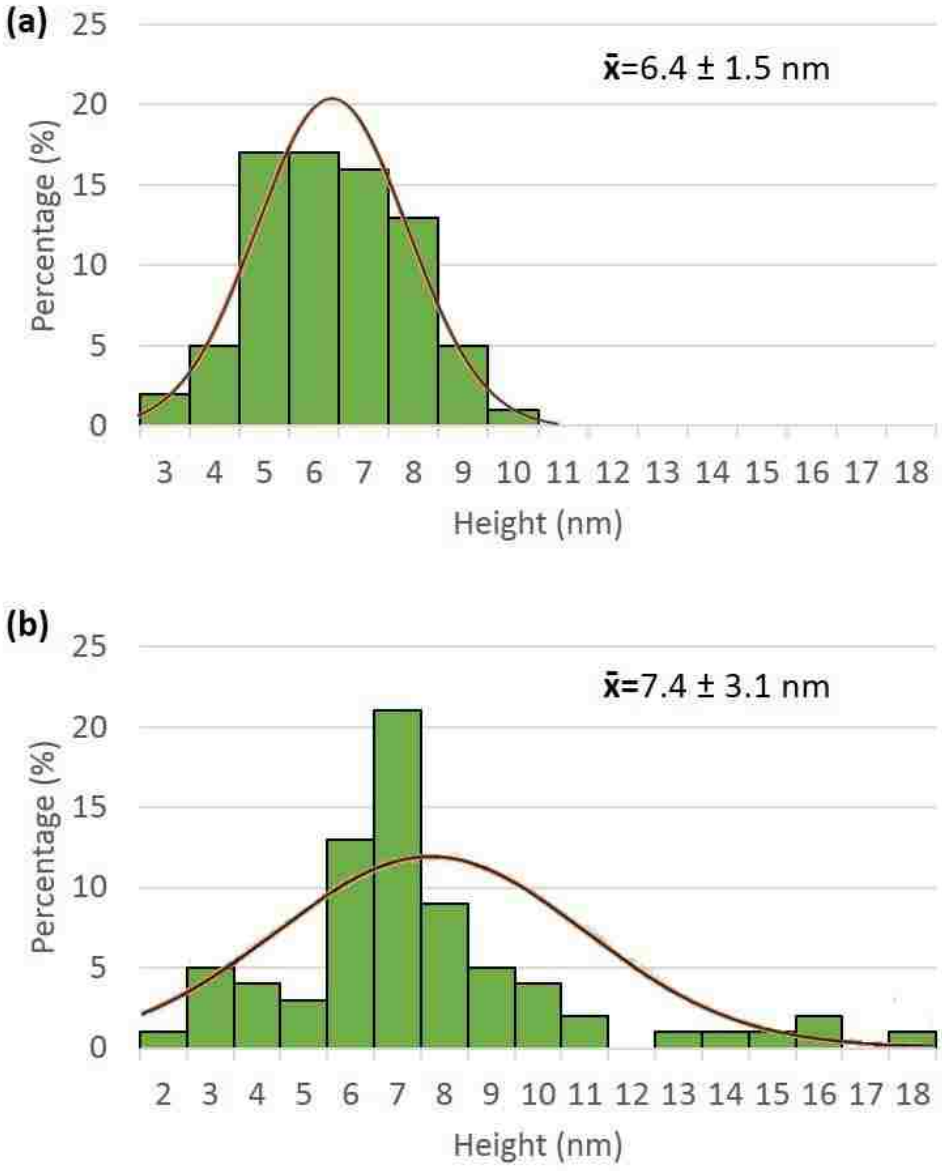

Figure 4.4 Heights of the nanodots of TPP and TPC. *(a)* Size distribution of TPP nanodots (*n*=76). *(b)* Height of TPC nanodots (*n*=73). The solid lines represent Gaussian fits of the data.

4.3.3 Conductive measurements with porphyrin nanostructures

The conductivity of the nanodots was measured in the vertical direction through the layers of porphyrin using conductive probe AFM. A platinum coated AFM tip was used as an electrode and was placed on the nanodots to establish a closed circuit loop with the gold substrate for the current flowing through the nanodot. A single measurement was made for each nanodot, because the surface contact became oxidized after applying voltage. As a test, we evaluated the changes in measurements with multiple successive measurements, and have included example I-V spectra in Apendix E, Figures E1 and E2.

Representative I-V curves of TPP nanodots and TPC nanodots are shown in Figure 4.5. To minimize the impact of the loading force and geometry of the tip on the current through the nanostructures,[61, 171] the same tip was used to collect all the I-V curves with controlled load less than 1 nN. The TPP nanodots exhibit a typical I-V profile of a semi-conductive material (Figure 4.5, a.). The maximum current measured through the TPP nanodot is 3 nA at 10 V. The current gradually decreases to zero when the voltage decreases from 10 V to 4 V in both negative and positive ranges. In between -4 V to +4 V, the TPP nanodots are relatively nonconductive. In contrast, the TPC nanodots show better conductivity in a relatively small voltage range, which is -2 V to +2 V. In this range, the maximum current through a TPC nanodot measured 10 nA at 2 V. The cobalt core in the molecular structure has a significant role in the conductive properties. The current gradually decreases to zero when the voltage was decreased from 2 V to 0 V in both the negative and positive ranges. The TPC nanodots with a cobalt ion coordinated to the macrocycle (Figure 4.5, b.) has a more conductive, wire-like profile than the semiconductive free-base porphyrin, TPP (Figure 4.5, a.). The magnitude of the measured currents and voltages are quite distinct depending on whether the nanodots contain a metal ion.

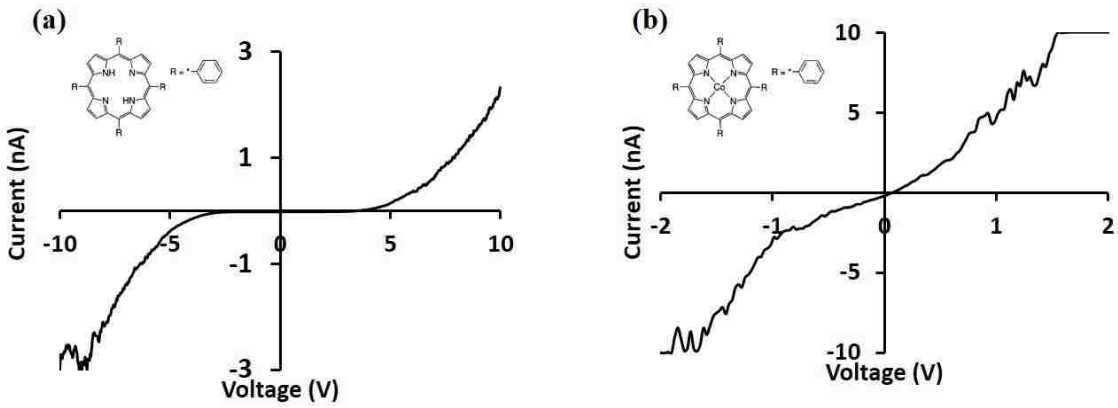

Figure 4.5 Example I-V curves for individual nanodots of *(a)* TPP and *(b)* TPC.

The porphyrin nanodots are an excellent model surface structure for conductive probe measurements. The sizes of the nanodots have slight variability at the nanoscale, which enables size-dependent analysis. Further example I-V curves collected from the TPP and TPC nanodots are presented in Appendix E, Figure E3.

Further analysis of the effects of the size of nanodots can be evaluated, as shown in Figure 6. The heights of the nanodots were plotted versus conductance measurements from 78 TPC nanodots. The heights of the nanodots ranged from 2 to 20 nm. A clear trend is apparent that shows greater conductance for taller nanostructures of TPC.

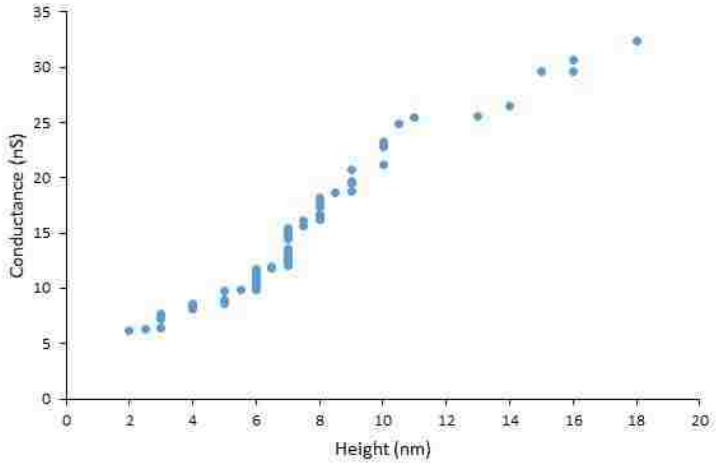

Figure 4.6 Heights versus the measured conductance of the TPC nanodots. (n = 78)

The conductance of the TPC nanodots was measured from the slopes of I-V curves. The conductivity of the nanodot formed by TPC molecules can be expressed as the slope of the linear portions of the plot. The conductivities observed from the three linear regions of a representative plot for TPC measured 1.18 S/m from 2 nm to 7 nm; 2.96 S/m from 7 nm to 11 nm; and 1.04 S/m for the range from 13 nm to 18 nm.

4.4 Conclusions

A new test platform is introduced for making conductive probe measurements of regularly-shaped, small clusters of porphyrins. Periodic arrays of nanodots of porphyrins were prepared in nanopores formed within dodecanethiol/Au(111). Dot-like nanostructures of porphyrins with and without a metal center were self-assembled within nanopores prepared by immersion particle lithography. The conductivity profiles were measured and compared using CP-AFM for 3-10 nm nanodots of cobalt-coordinated and free-base porphyrins. Distinct I-V profiles were exhibited with TPC and TPP nanodots that were chosen as model systems. The key difference between the structures of the two selected porphyrins is the cobalt core. For TPP nanodots, profiles that are typical of semi-conductive films were observed. With cobalt-coordinated TPC nanodots, wire-like conductive profiles were exhibited. As might be predicted, the conductivity of TPC nanodots is greater than that of TPP nanodots. The approach described demonstrates the feasibility for sensitive measurements of the conductivity of multiple, replicate nanodots with CP-AFM.

CHAPTER 5: DISTANCE-DEPENDENT MEASUREMENTS OF THE CONDUCTANCE OF PORPHYRIN NANORODS STUDIED WITH CONDUCTIVE-PROBE ATOMIC FORCE MICROSCOPY

5.1 Introduction

Porphyrin molecules and associated derivatives are building blocks in molecular electronics, photovoltaic materials, and supramolecular designs.[172] Nanorods of porphyrins have potential for applications including energy and electron transfer,[135,173] chemical catalysis,[174] chemical sensors,[175] optical devices,[137] electronic devices,[173] biological light-harvesting structures,[173] gas storage, field-effect devices[173] and chiroptical systems.[175] The applications originate from the unique characteristics of porphyrins that include rigid and planar geometries, readily tailored spectroscopic and photochemical properties, multifunctionality, biocompatibility,[175] and the ability to serve as an electron donor.[135] The conductive properties of porphyrins and derived nanostructures have not been fully characterized or modeled.

Methods of surface fabrication with porphyrin nanorods include surfactant-assisted self-assembly (SAS),[173] ionic self-assembly (ISA),[176-177] mixed porphyrin self-assembly,[178] sonication-assisted self-assembly,[135] and metal coordination-assisted self-assembly. Among the studies reported for porphyrin nanorods, rod-like aggregates derived from meso-tetra(4-sulfonatophenyl) porphyrin ($TPPS_4$) are a well-studied example because of it is a biomimetic analog of photosynthesis systems.[163, 176, 179-188] The heights and lengths of the $TPPS_4$ nanorods range from several nanometers and from dozens of nanometers in diameter and up to several micrometers in length[163, 174, 181, 187-188] The size and shapes of the nanorods derived from $TPPS_4$ are due to a combination of molecular interactions including, Coulombic interactions, π-π interactions and intermolecular electrostatics.[189]

A self-assembled monolayer (SAM) of dodecanethiol on Au(111) was selected as an insulating layer between the porphyrin nanorods and the gold substrate for the CP-AFM measurements.[190-192] A surface template of nanoholes was fabricated within a dodecanethiol SAM with immersion particle lithography.[3] We have developed protocols with immersion particle lithography to prepare arrays of nanoholes within organic thin films on surfaces such as gold, mica and silicon.[3, 13, 50, 99, 193] Typically, when a surface coated with mesoparticles is immersed in solutions, the particles are displaced. Therefore, an annealing step is critical for immersion particle lithography. The nanoholes formed within a SAM furnish spatially confined areas for growing porphyrin nanorods with one end connected to the gold surface. The surface-bound patterns provide an excellent measuring platform for evaluating conductivity along the length of porphyrin nanorods. In this report, the feasibility of making distance-dependent conductance measurements along the length of isolated nanorods is evaluated with CP-AFM for test platforms of TPP and TPC nanorods.

A simple metallic porphyrin structure, 5,10,15,20-Tetraphenyl-21H,23H-porphine cobalt(II) (TPC), and the metal-free analogue 5,10,15,20-Tetraphenyl-21H,23H-porphine (TPP) were selected to construct rod-like nanostructures on template stripped gold (TSG) for measurements using conductive probe-atomic force microscopy (CP-AFM). The structures of TPP and TPC are shown in Scheme 5.1. The driving force for self-assembled nanorods of TPP or TPC is mainly dependent on single interactions i.e. π- π interactions.[135] Unlike the $TPPS_4$ nanostructures, which aggregate in solution,[194] the TPP and TPC nanorod structures formed on the surface of the substrate. The nanorod aggregates could be considered as model structures for gaining insight into lateral conductance of rod-like electronic building blocks in nanoscale with assistance of CP-AFM.

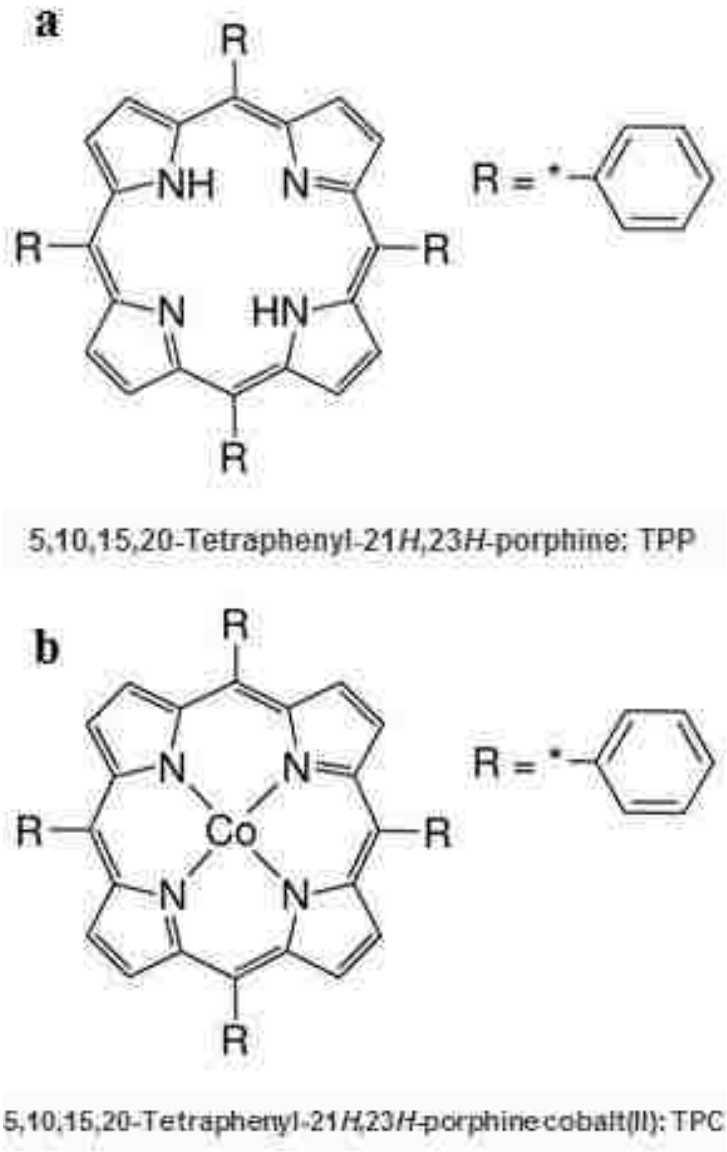

Scheme 5.1 Structures of *(a)* 5,10,15,20-tetraphenyl-21H,23H-porphyrin (TPP) and *(b)* 5,10,15,20-tetraphenyl-21H,23H-porphyrin cobalt(II) (TPC).

The self-assembled monolayer (SAM) of 1-dodecanethiol on Au(111) surface was selected as the insulator layer between the porphyrin nanorods and the gold electrode for the conductive measurement in lateral direction because of the high resistance in nanoscale measurement.[70, 191] A periodic nanopore template was fabricated within a 1-dodecanethiol SAM by immersion particle lithography.[3] Immersion particle lithography is widely employed to fabricate periodic nanopore

patterns in organic thin films on surfaces such as TSG and silicon wafer.[3, 13, 50, 99, 195] The periodic nanopores on TSG surface offer spatially confined nanoareas for porphyrin nanorods to grow. With one end connected to the gold surface and the rest of the nanorod lying on the electrical insulated species, thiolate thin film, a measuring template for conductivity along the long axis of porphyrin nanorod is constructed. A platinum coated AFM tip can be applied to the other end of nanorod. With a bias voltage applied to either the gold surface or coated AFM tip, conductive measurements of porphyrin nanorods can be collected with a controlled mechanical load. By taking advantage of periodic nanopore templates, our work provides a practical simple method of measuring the current along the long axis of a porphyrin nanorods, compared to the methods developed using nanometer sized gap (nanogaps),[196] break junctions,[197] carbon nanotubes/nanowires.[68]

Distinct conductive behavior was found between TPC and TPP nanorods. The TPC nanorods presented semi-conductive behavior in the testing voltage range with different conductance values under negative and positive biases. The TPP nanorods showed a rectifier behavior with an increased conductance value towards the end connected to the gold surface along the axial direction in positive bias. In addition, the height and length of the nanorods formed by different porphyrin molecules are compared. TPC nanorods are shorter in height and longer in diameter in terms of morphology. Considering the feasibility of techniques that we employed in this study, the lateral conductive measurements of the isolated nanorods on nanopore templates with assistance of CP-AFM may be further studied with other porphyrins with different metal atoms who can form extended superstructures.

5.2 Materials and methods

5.2.1 Materials

5,10,15,20-tetraphenyl-21H,23H-porphine cobalt(II) (TPC), 5,10,15,20-tetraphenyl-21H,23H-porphine (TPP) ,1-dodecanethiol and dichloromethane were purchased from Sigma Aldrich (St. Louis, MO) and used as received. Ethanol (200 proof) was obtained from Pharmco-AAper Alcohol and Chemical Co. (Shelbyville, KY) and used as the diluent for preparing 1-dodecanethiol solutions. Dichloromethane was purchased from Sigma Aldrich (St. Louis, MO) for dissolving porphyrins. Gold pellets (99.99% purity) were purchased from Ted Pella (Redding, CA). Ruby muscovite mica was purchased from S&J Trading Inc., (Glen Oaks, NY).

5.2.2 Preparation of porphyrin solutions

To prepare porphyrin solutions for making nanoaggregates on Au(111) substrates, TPC and TPP were separately dissolved in dichloromethane at the concentration of 10^{-3} M before they were diluted into 10^{-5} M with ethanol. The nanorods of each porphyrin were prepared by immersing the substrates into final solutions for 42 h. The nanoaggregates of TPP shown in Figure S1were made by depositing aged final solution on the substrates.

5.2.3 Preparation of template-stripped Au(111)

Template-stripped gold (TSG) films were prepared using thermal evaporation as previously described.[3] In brief, gold slugs were deposited onto freshly cleaved Ruby muscovite mica substrates in a high-vacuum thermal chamber (Angstrom Engineering Inc., Kitchener, OR) at 10^{-7} mm Hg. Prior to gold deposition, the mica substrates were preheated to 350°C using quartz lamps mounted at the back of the sample holder. The deposition rate of gold was 3 Å/s for the final thickness of 150 nm. After deposition, the gold substrates were annealed at 365°C under vacuum of 10^{-7} mm Hg for 30 min and then cooled to room temperature. The gold films were glued to glass

slides using epoxy as previously reported by Hegner et al.[129] The gold substrates and glass slides were cleaned by rinsing with deionized water followed by 30 min treatment in a UV-ozone generator. Epoxy was mixed (1:1 by weight) and immediately applied onto the cleaned glass slides. The glass slides were placed onto the gold surfaces with a thin layer of epoxy formed between the glass and gold surfaces without any air bubbles. The mica-gold-glass sandwiches were then heated in oven at 150°C for 2 h to anneal the epoxy. After cooling to room temperature, the glass pieces were mechanically removed from the mica surfaces to obtain TSG.

5.2.4 Preparation of Porphyrin Nanostructures within Thiol Nanoholes

Immersion particle lithography was used to prepare arrays of nanoholes on Au(111) as previously reported.[3] Silica mesospheres (500 nm diameter) were cleaned by centrifugation to remove surfactants or charge stabilizers. A 300 μL aqueous suspension of silica mesospheres with the concentration of 2% was transferred into a microcentrifuge tube and centrifuged for 20 min at 20,000 rpm. A solid pellet formed at the bottom of the centrifuge tube, and the supernatant was decanted. The centrifuge tube was refilled with deionized water and the pellet was resuspended by vortex mixing. The washing cycle of mesospheres was repeated four times. Cleaned silica mesospheres (20 μL) were deposited onto freshly striped TSG as surface masks for subsequent steps of solution immersion. The surface masks of silica spheres were dried under ambient conditions, then heated at 150°C for 12 h. The heating step helps prevent the mesospheres from being displaced from the surface during immersion in solutions. The samples were cooled to room temperature (25°C), then immersed into a dodecanethiol ethanolic solution (10^{-3} M) for 24 h. Self-assembled monolayers (SAMs) of dodecanethiol formed on the exposed areas of the TSG surfaces surrounding the areas protected by the mesospheres. Next, the mesospheres were removed by sonication in ethanol. Arrays of nanoholes were fabricated within the dodecanethiol SAM.

The samples of nanoholes formed on Au(111) were submerged in a 10^{-7} M solution of TPC or TPP for 42 h to obtain porphyrin nanorods. In the final step, the samples of porphyrin nanostructures were rinsed with ethanol to remove loosely bound aggregates, then dried in air. The uncovered areas of Au(111) that had been masked by mesospheres provided well-defined surface sites for directing the subsequent attachment and growth of porphyrin nanorods.

5.2.5 Atomic force microscopy

A Keysight 5420 scanning probe microscope (Keysight Technologies, Santa Rosa, CA) with PicoView v1.12 software was used for scanning probe characterizations. Images were acquired using tapping mode in ambient conditions. Imaging was accomplished with rectangular shaped ultrasharp silicon tips (Nanoscience Instruments, Phoenix, AZ) that have an aluminum reflex coating, with a spring constant of 48 N/m. The scan rate was 1 line/s. Electrical measurements with porphyrins were done with the same instrument equipped with conductive nose assembly (0.1 nA/V sensitivity) and conductive sample plate. Conductive tips (PPP-CONTPt, Nanosensors, Neuchatel, Switzerland) with a platinum coating were used to take the I-V profiles. Topography and phase images were processed with Gwyddion v. 2.32, which is an open-source software available from internet.[130]

5.3 Results and discussion

Nanorods of porphyrins were prepared on a template of nanoholes within a dodecanethiol film on Au(111) using steps of immersion particle lithography. A description of the method for preparing patterns of nanorods is outlined in Supporting Information, Figure S1. Model structures of 5,10,15,20-tetraphenyl-21H,23H-porphyrin cobalt(II) (TPC), and the metal-free analog 5,10,15,20-tetraphenyl-21H,23H-porphyrin (TPP) were selected for studies with CP-AFM. The structures of TPP and TPC are shown in Scheme 5.1.

The morphology of the nanorods formed by either TPP or TPC were characterized by tapping mode AFM in ambient conditions (Figure 5.1). Individual porphyrin nanorods are visible throughout the surface, predominantly binding at sites of the gold nanoholes. Characteristics of

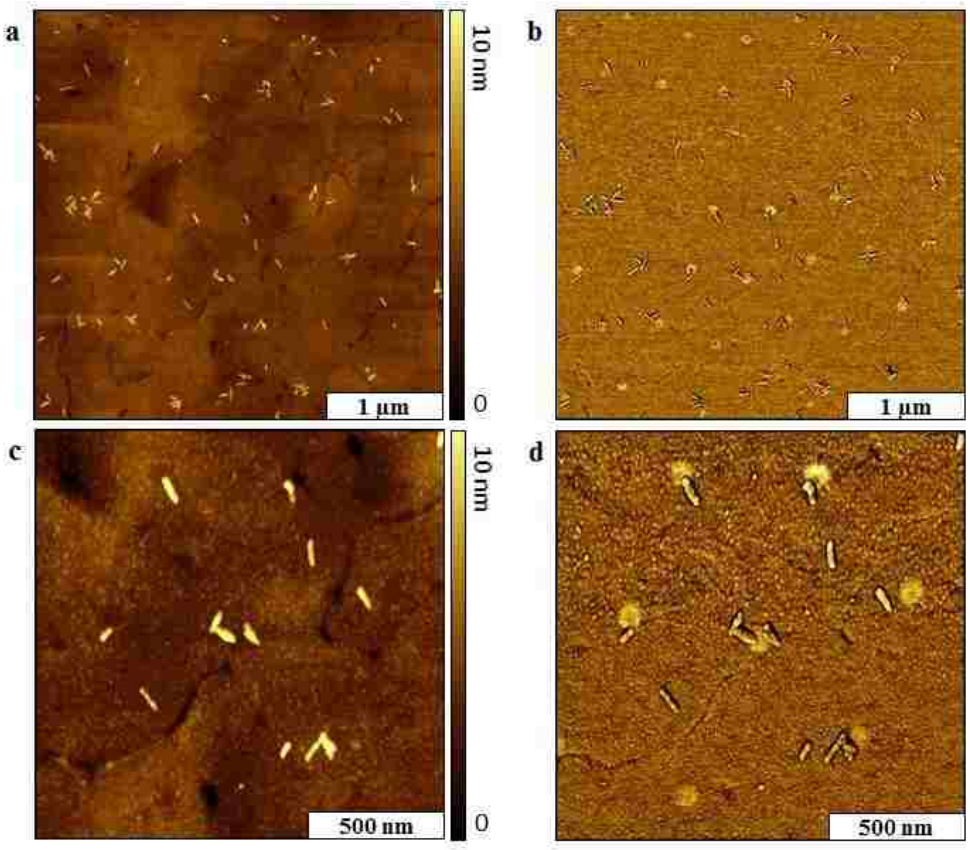

Figure 5.1 Nanorods of TPP grown in nanoholes within dodecanethiol. *(a)* Arrangement of nanorods shown with a topography image; *(b)* simultaneously acquired phase image; *(c)* localization of nanorods within nanopores (topography view); *(d)* corresponding phase image.

the gold surface, such as domain boundaries, scars and holes, are apparent in the background of the topography images (Figures 5.1, a. and 5.1, c.). The periodic arrangement of nanoholes can be discerned as bright circular dots in the corresponding phase images (Figures 5.1, b. and 5.1, d.). The nanoholes are uncovered areas of substrate where the silica mesospheres were displaced. The distance between neighboring nanoholes is 500 nm as determined by the diameter of the monodisperse mesospheres used as surface mask. The nanoholes were protected from deposition

of dodecanethiol by the mesospheres, and areas surrounding the nanoholes present methyl groups of the dodecanethiol SAM that was used as a resist. The nanoholes are exquisitely small (~100 nm in diameter, and 1.5 nm in depth) and are designed to define spatial selectivity for depositing porphyrins.[132]

In most of the nanoholes, one or more nanorod is present and connected to an area of bare gold. A few of the nanorods are present on the SAM matrix areas, which most likely grow in defect areas. Closer details of the nanorods are revealed in Figures 5.1, c. and 5.1, d. Among the seven nanoholes, five of them contain TPP nanorods. Two of the nanoholes are unfilled and four free nanorods are lying on areas of the SAM. We hypothesize that the nanorods of porphyrins were directly grown at the areas of bare Au(111) during the immersion process, since shorter immersion times lead to shorter nanostructures of nanodots. To evaluate if nanorods formed in solution, a drop of similarly aged TPP solution was deposited onto the surface. Nanorods did not form on the surface. (Appendix F, Figure F, 2.). The drop-deposition experiment indicates that the nanorods did not form in solution during the immersion step, but rather that the rod-like shapes grew from the surface over a time period of 42 h.

The nanopatterning process for preparing nanorods was repeated with TPC using the same concentration of the porphyrin solution and 42 h immersion period. Rod-shaped nanostructures of TPC were also reproducibly grown from the gold surface (Appendix F, Figure F, 3.). The dimensions of a TPC nanorod can be derived from cursor profiles taken in the longitudinal and orthogonal directions. The size distribution of the nanorods were compared for TPP and TPC (Appendix F, Figure F, 4.). The dimensions of the TPP nanorods were measured from 64 cursor profiles from several areas of a sample. The average length of the TPP nanorods is 160 ± 41 nm. The average height of the TPP nanorods measured 6 ± 1 nm. The dimensions of TPC nanorods

were collected from 82 measurements from several areas of a sample. The TPC nanorods measured 130 ± 49 nm, with heights of 3 ± 1 nm. The shape of AFM probes influences the sizes that measured, particularly for lateral dimensions. Sharper probes produce more accurate measurements.

A representative TPP nanorod is shown in Figure 5.2. The nanorod has one end connected to the area of a nanohole. The rest of the nanorod is lying on the dodecanethiol SAM which serves as an insulating matrix. The placement of the nanorod within the nanohole is also visible in the corresponding phase image (Figure 5.2, b.). The size of the individual nanorod from the cursor line profiles indicates a length of 160 nm and height of 6.6 nm.

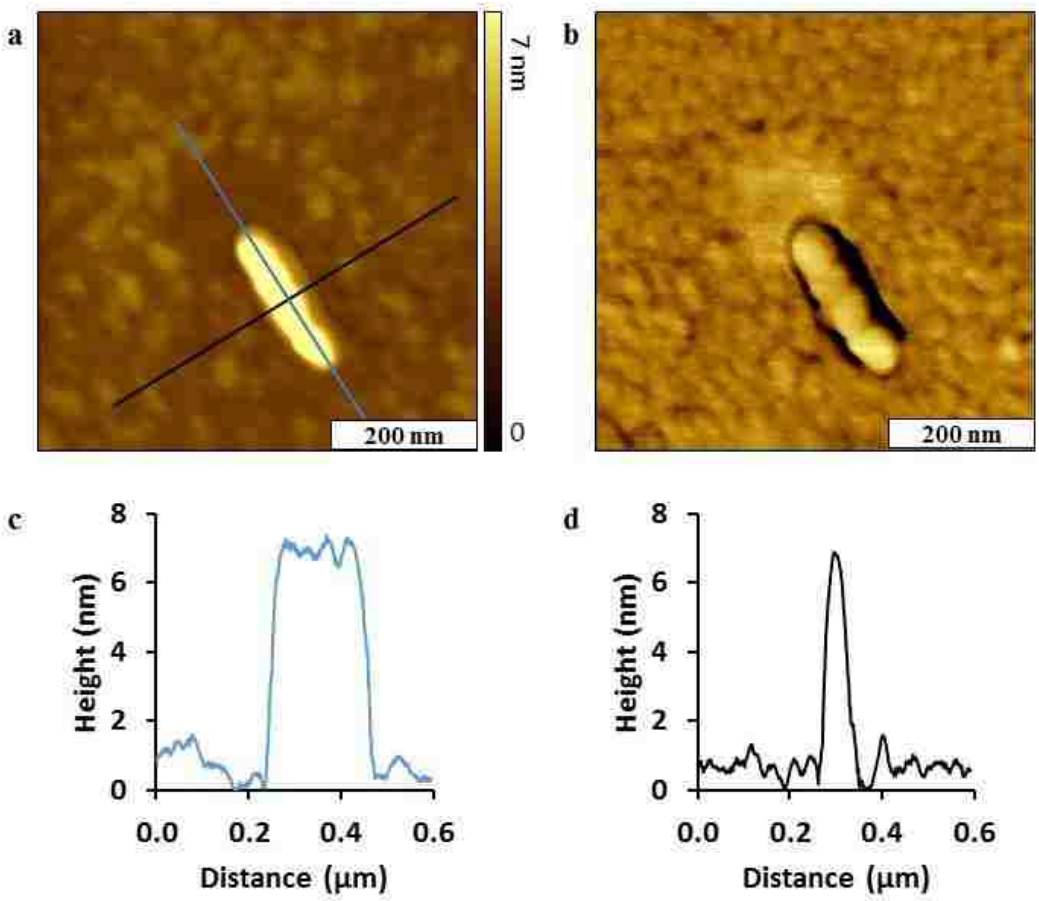

Figure 5.2 Close-up of an individual TPP nanorod. *(a)* Topography image; *(b)* corresponding phase image; *(c)* cursor profile of a transverse section of a nanorod; *(d)* cursor profile of a longitudinal section of a nanorod.

The conductivity along the length of the nanorods was measured using CP-AFM. A platinum coated AFM tip was placed at selected points along the nanorod with a controlled load to measure the distance-dependent current. Three testing points were selected along the nanorod to collect the I-V curves (Figure 5.3, a.). The points selected include each end of the porphyrin where one end is in contact with the matrix SAM and the other is in direct contact with the gold substrate. One test point was located between the two ends. At each of the three sites the voltage was swept from -10 to +10 V and the resulting current was measured (Figure 5.3, b.).

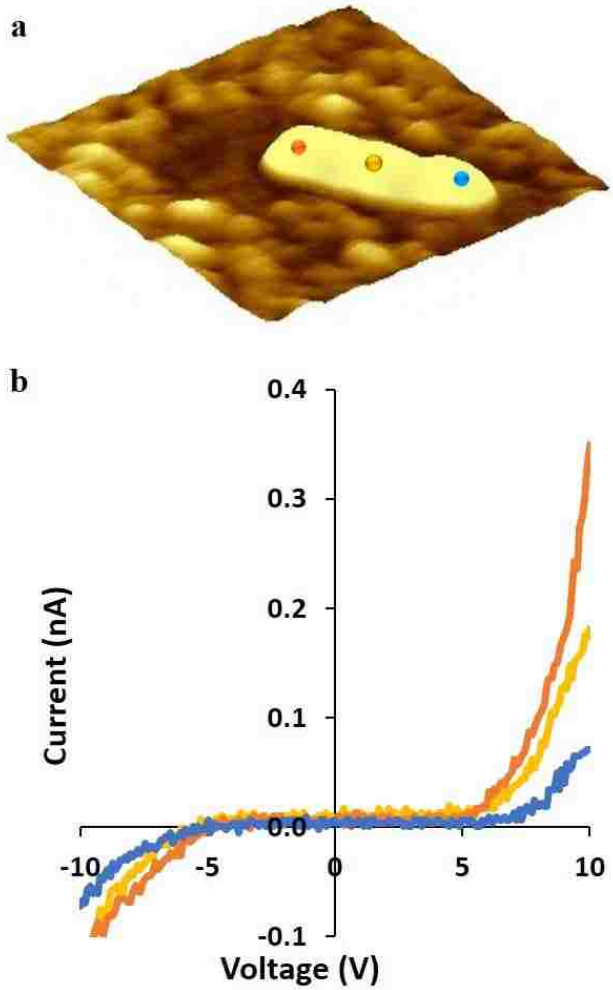

Figure 5.3 Distance-dependent measurements of conductivity along a TPP nanorod. *(a)* A TPP nanorod localized in a nanohole. The colored dots indicate the testing points on the nanorod where I-V curves were collected; *(b)* I-V curves collected from selected locations along the TPP nanorod shown in corresponding colors.

Trends of the conductive properties correspond to the testing positions. Current-voltage curves indicate an increase in conductance as the tip is moved closer towards the Au surface. The current at 10 V increases along the horizontal direction of the TPP nanorod. In reverse, the conductance of the nanorod decreases as a function of the testing distance. The highest current at -10 V remained same during this experiment. The onset of the turn on current occurs at a lower voltages as the tip is moved closer to the end of the TPP nanorod that is attached to gold.

Similar measurements were done for a cobalt-coordinated TPC nanorod localized on a nanopore. The morphology of an individual TPC nanorod on a nanopore is shown in Figure 5.4. The defect of the gold substrate under the thin dodecanethiol SAM can be seen in both topography and the corresponding phase images (Figures 5.4, a. and 5.4, b.). In the phase image, the bare gold area of the nanopore can be discerned as a dark circle. The dimensions of the TPC nanorod measured 230 nm in length and the height is 16 nm (Figure 5.4, c.).

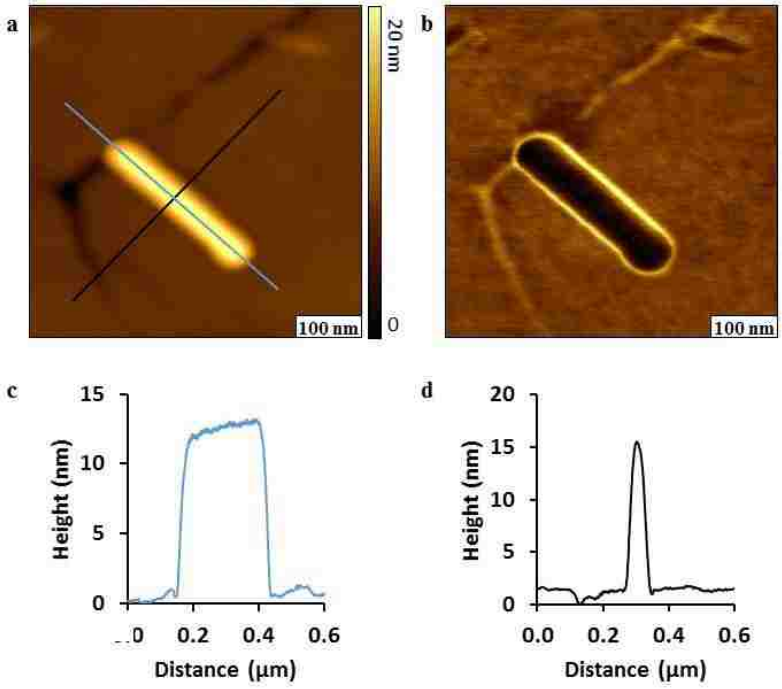

Figure 5.4 Close-up of an individual TPC nanorod. *(a)* An individual TPC nanorod shown with a topography image; *(b)* corresponding phase image; *(c)* cursor profile of a transverse section of the nanorod; *(d)* cursor profile of a longitudinal section.

Conductive measurements were conducted on the TPC nanorod with CP-AFM (Figure 5.5). Six testing points along the TPC nanorod were chosen for the I-V curves shown in Figure 5.5a. Distinct differences of the I-V profiles were observed for the TPC nanorods (Figure 5.5, b.) compared to TPP (Figure 5.3, b.). In the -2.4 v to +2.4 v range, semi-conductive profiles are shown for each of the six I-V curves shown in Figure 5.5, b. The conductance measured from the positive voltage range is larger than that measured from the negative voltage range. The highest currents are -10 nA and +10 nA at -2.4 V and +2.4 V, respectively. The metallic core in the cobalt-coordinated TPC is greater compared to the TPP nanorod.

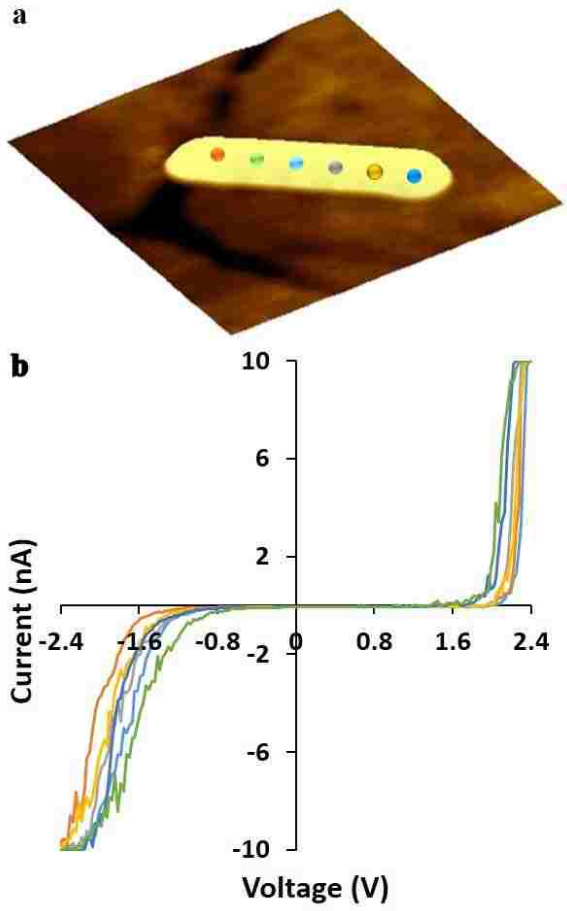

Figure 5.5 Distance-dependent measurements of conductivity along a TPC nanorod. *(a)* A TPC nanorod localized within a nanopore. The points on the nanorod represent the testing sites where the I-V curves were collected; *(b)* I-V curves collected from selected locations on TPC nanorod shown in corresponding colors.

To evaluate the conductive behavior of the two types of nanorods, the conductance at selected testing points on TPC and TPP nanorods were calculated. (The conductance was measured as the slope of the linear parts of each I-V curve.) Since both TPC and TPP have semi-conductive profiles, the conductance was categorized for the negative and positive regions of the curves (Table 5.1). The values of the TPP nanorods are expressed in the pico Siemens range which is a thousand times lower than that of the TPC nanorods. A general trend is revealed as the tip is moved along the length of the nanorods, in which the conductance increases as the probe is moved further away from the gold substrate. When one considers the larger size of the coated AFM probe, it appears that there is spatial overlap when six or more measurements are taken side-by-side. The values acquired in the positive voltage side are higher than the values acquired from the negative voltage side.

Table 5.1 Conductance measurements at selected points along TPP and TPC nanorods.

Measuring	TPP		TPC	
Point[a]	Negative Bias (pS)	Positive Bias (pS)	Negative Bias (nS)	Positive Bias (nS)
1	6	6	10	51
2	12	32	11	74
3	28	32	12	80
4	14	51	14	32
5	23	59	10	51
6	25	92	10	51

[a] Numbers 1 to 6 indicate the measuring points from the end away from the gold surface (1) to the end in contact with the gold surface (6).

The feasibility of measuring conductance along the length of nanorods with CP-AFM was demonstrated, facilitated by the localization of the nanorods on uncovered areas of gold substrates. Arrays of TPP and TPC nanopores ensured multiple, reproducible measurements with I-V profiles. The properties of porphyrins at the nanoscale furnish important information for future applications.

5.4 Conclusions

Rod-shaped nanostructures of TPP and TPC were placed within nanoholes fabricated within a dodecanethiol SAM prepared by immersion particle lithography. The geometry of the nanorods enables multiple, distance-dependent measurements of nanoscale conductance using CP-AFM. The nanorods of TPP exhibit conductive profiles of an insulating material. Nanorods of TPC show semi-conductive behavior in the longitudinal direction with the onset of the turn-on currents shifting to zero volts as the testing point approaches the end in contact with gold electrode. The strategies described herein enable measurements with a reproducible surface test platform for future studies to characterize more complex molecules.

CHAPTER 6: CONCLUSIONS AND FUTURE PROSPECTUS

Nanofabrication based on scanning probe lithography and particle lithography were developed and applied to create nanostructures within organothiol SAMs on Au(111) surfaces. Well studied *n*-alkanethiols were used as an internal reference for locally measuring the orientation of a newly designed multidentate thiol on Au(111). Structural templates fabricated within organothiol SAMs with assist of closed packed monodisperse spheres as surface mask were used to spatially confine the aggregation of porphyrins at the nanoscale for conductive measurements with AFM. Particle lithography offers the advantages of high throughput, and reproducibility for fabricating dimension tunable nanostructures. Patterned surfaces were used to chemically define the attachment of designed nanomaterials. With the advanced scanning probe measurements, properties of samples were measured at molecular level. Although the discussion and results presented in this dissertation focused on selected nanomaterials, the applicability of the methods is more generic. The techniques developed in this dissertation will be applicable to investigations of the properties of thin films and surface self-assembly for studies in the future.

6.1 Self-assembly of bidentate thiol on Au(111) studied with AFM

Protocols for AFM-based nanolithography as well as immersion particle lithography were used to evaluate the morphology and thickness of bidentate BMPHA on Au(111). The established thickness of monodentate ODT was used as a reference for *in situ* measurements of film thickness. Either monolayer or bilayer films of BMPHA can be formed on Au(111) by controlling the parameters of solution concentration and the duration of immersion in ethanolic solution. The thickness of monolayer films of BMPHA measured 2.0 ± 0.2 nm, which is consistent with previous measurements reported using ellipsometry. Assuming that both thiols of BMPHA bind to gold, this value would correspond to a tilt angle of 34° from the surface normal. Head-to-head

dimerization between interfacial carboxylic groups can produce bilayers of BMPHA, as has previously been demonstrated for *n*-alkanethiols with carboxylic acid groups. Both monolayer and bilayer films of BMPHA could be generated using immersion particle lithography. Periodic island nanopatterns of ODT were grown within nanoholes of BMPHA, constructed with a successive step of sample immersion in SAM solution. Future directions for this research will be to develop protocols to compare the long-term stability of bidentate versus monodentate structures using nanofabricated test structures.

6.2 Measurement of spatially confined nanoclusters of porphyrins using CP-AFM

A new surface test platform was introduced for making conductive probe measurements of regularly-shaped, small clusters of porphyrins. Periodic arrays of nanodots of porphyrins were prepared in nanopores formed within dodecanethiol/Au(111). Dot-like nanostructures of porphyrins with and without a metal center were self-assembled within nanopores prepared by immersion particle lithography. The conductivity profiles were measured and compared using CP-AFM for 3-10 nm nanodots of cobalt-coordinated and free-base porphyrins. Distinct I-V profiles were exhibited with TPC and TPP nanodots that were chosen as model systems. The key difference between the structures of the two selected porphyrins is the cobalt core. For TPP nanodots, profiles that are typical of semi-conductive films were observed. With cobalt-coordinated TPC nanodots, wire-like conductive profiles were exhibited. As might be predicted, the conductivity of TPC nanodots was shown to be greater than that of TPP nanodots. The approach described demonstrates the feasibility for sensitive measurements of the conductivity of multiple, replicate nanodots with CP-AFM.

6.3 Nanorods derived from porphyrins characterized with CP-AFM

Rod-like nanostructures formed by TPP and TPC molecules were attached to gold nanopores within a 1-dodecanethiol template fabricated by immersion particle lithography. The nanorods of TPP present rectifier conductive profiles in the longitudinal direction. In addition, the nanorods of TPC have shown semi-conductive behavior in the longitudinal direction with the onset of the turn-on currents shifting to zero volts when the testing point approaches to the end in contact with gold electrode. The strategy outlined in this study may be flexible enough to construct nanofabricated building blocks for molecular electronics and to provide a platform to electronically characterize more complex structures.

6.4 Future prospectus

Organic thin films are crucial for the production of biosensors,[198-200] corrosion-resistant surfaces,[201-202] medical[203] and electronic devices.[204] Platforms for emerging technologies will require robust organic films that are resistant to environmental effects such as heat and oxidation. For example, diazonium salts provide thin films with higher thermal and oxidative stability than thiol-based self-assembled monolayers (SAMs). The stability of multilayers derived from alkyldiazonium salts has been demonstrated.[205-207] Polyphenylene multilayers derived through the grafting of aryldiazonium salts have demonstrated stability at temperatures up to 700 K under ultra-high vacuum and remain stable in laboratory air for months.[208] Investigations of photografting reactions at the molecular level can help to fine tune the quality of the organic films and to achieve better control of surface reactions.

6.4.1 Design of a transparent AFM sample cell for liquid imaging

Protocols will be developed for *in situ* studies in liquid media to enable time-lapse AFM imaging. Liquid environments expand the capabilities of AFM protocols that will provide insight

into dynamic processes at the molecular level. Liquid imaging provides intrinsic advantages for AFM studies, particularly for conducting in situ investigations of chemical or biochemical reactions. Strong capillary interactions between the tip and sample that are present in ambient air can be reduced or eliminated in liquid media.[209] Liquid media helps to improve the resolution of AFM experiments since the amount of force applied between the tip and sample can be greatly reduced.[210] The investigation of surface changes throughout the course of chemical self-assembly reactions have been monitored with AFM in liquid media.[211] Injecting solutions into a liquid sample cell enables protocols for AFM-based nanografting.[212]

A transparent sample cell will be designed to enable irradiation of samples. A prototype sample cell that enables irradiation of the sample with visible light from a fiber optic cable below the sample stage is shown in Figure 6.1, which is made of machined polycarbonate. A glass sample

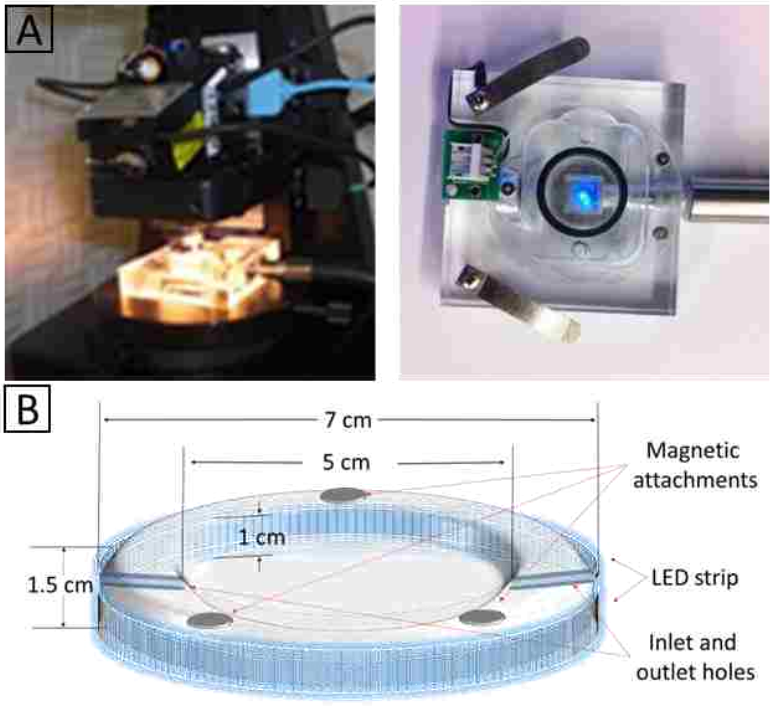

Figure 6.1 Designs for home-built AFM sample stages. *(a)* Home-constructed sample stage for AFM photoimaging (prototype). A prism is embedded within a transparent polycarbonate block to direct light through the sample. *(b)* Design for proposed sample cell to be machined in glass or quartz material.

stage will need to be constructed for irradiation of samples from the side or top of the stage to enable *in situ* studies for protocols with photocatalytic surface reactions. The design of a glass sample cell is shown in Figure 6.1, b. The transparent sample cell will include a circular reservoir for the reagent solution, approx. 7 cm in diameter with a thickness of 1.5 cm. Two holes will be drilled in the sides of the sample container (1 mm diameter) for connecting tubing. Plastic tubing is used to introduce reagents or for rinsing protocols for reaction steps. A light strip from a light-emitting diode (LED) source encapsulates the sample cell as a light source. This will ensure that the light intensity of irradiation is evenly dispersed within the entire cell. Three magnetic pellets are embedded at the edge of the sample cell for mounting the stage onto an AFM scanner.

6.4.2 Studies of the mechanism and kinetics of photocatalytic reactions on Au(111)

While the kinetics and mechanisms of film growth of SAMs derived from *n*-alkanethiols have been well-studied,[213] analogous investigations of the surface assembly of photografted diazonium salts on surfaces have not yet been reported. To understand more completely the surface structure and assembly process of photografting diazonium salts, studies of surface reactions will be accomplished with time-lapse AFM, within a liquid environment. By using a transparent cell for liquid AFM studies, fresh reagents can be introduced to the system to enable monitoring of surface changes over time (Figure 6.2). My strategy will be to use dilute solutions of reagents to carefully control the reaction conditions and to localize the sites of reactions to well-defined, discrete local areas of the surface obtained with nanofabrication protocols.

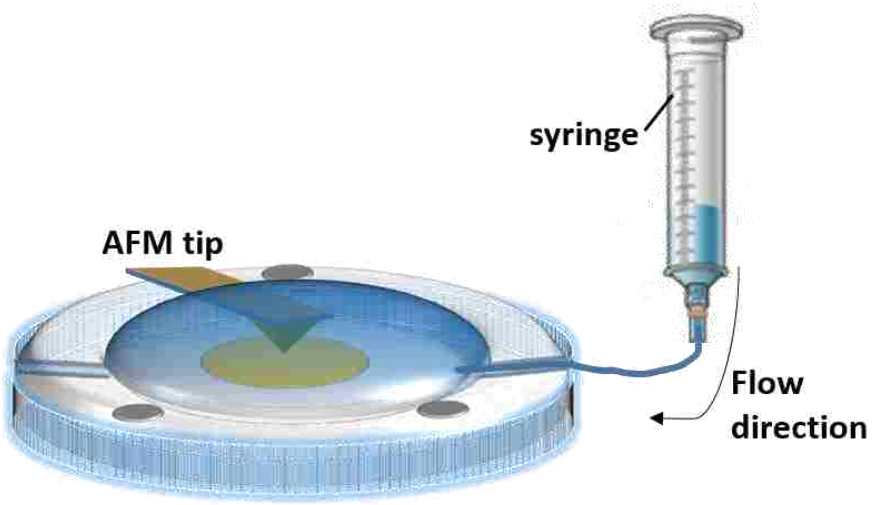

Figure 6.2 Setup for time-lapse AFM in liquids.

The surface will be imaged in liquid before injecting a solution of diazonium salts. After injecting a solution of diazonium salt with $Ru(bpy)_3^{2+}$,which is the photocatalyst into the sample cell, visible light will be turned on. The free radical is generated by activated $Ru(bpy)_3^{2+}$. Configuration changes of adsorbates on surfaces will be observed in a time-lapse fashion. The thickness of the adsorbates can be measured precisely at the nanoscale. Kinetic trends for the adsorption of free radical will be expressed with the increases in surface coverage as time progresses. From the rate of surface change, interactions between neighboring molecules will be disclosed from AFM images captured over time.

Photografting of diazonium salts onto gold surfaces provides an excellent model reaction for studies of photocatalytic reactions. In situ studies with AFM protocols will uncover mechanistic aspects of thin film growth and guide the design of methods for photografting other molecules, such as (primary alkyl halides, phthalimide esters, diaryliodonium salts and aryl iodides). Evidence suggests a solid link between the mechanism and kinetics of surface reactions with the properties of thin films.

Methods for direct *in situ* observation and measurement of how molecules react with surfaces offer interesting and valuable opportunities for chemical research. Invention of an AFM liquid cell for imaging reactions initiated by photocatalysis offers a new approach for nanoscale studies of the mechanisms and kinetics of surface reactions that has not previously been reported. Protocols with nanoshaving and nanografting will be developed to gain insight into the growth and physical characteristics of organic thin films.

REFERENCES

1. Binnig, G.; Rohrer, H., Scanning tunneling microscopy. *Helv. Phys. Acta* **1982,** *55* (6), 726-735.

2. Binnig, G.; Quate, C. F.; Gerber, C., Atomic force microscope. *Phys. Rev. Lett.* **1986,** *56* (9), 930-933.

3. Zhai, X.; Lee, H. J.; Tian, T.; Lee, T. R.; Garno, J. C., Nanoscale lithography mediated by surface self-assembly of 16-[3,5-bis(mercaptomethyl)phenoxy]hexadecanoic acid on Au(111) investigated by scanning probe microscopy. *Molecules* **2014,** *19* (9), 13010-26.

4. Samori, P., Scanning probe microscopies beyond imaging. *J. Mater. Chem.* **2004,** *14* (9), 1353-1366.

5. Dokukin, M. E.; Sokolov, I., Quantitative mapping of the elastic modulus of soft materials with HarmoniX and PeakForce QNM AFM modes. *Langmuir* **2012,** *28* (46), 16060-71.

6. Li, J. R.; Lewandowski, B. R.; Xu, S.; Garno, J. C., Detecting the Magnetic Response of Iron Oxide Capped Organosilane Nanostructures Using Magnetic Sample Modulation and Atomic Force Microscopy. *Anal. Chem.* **2009,** *81* (12), 4792-4802.

7. Fonseca, L.; Perez-Murano, F.; Calaza, C.; Rubio, R.; Santander, J.; Figueras, E.; Gracia, I.; Cane, C.; Moreno, M.; Marco, S., AFM thermal imaging as an optimization tool for a bulk micromachined thermopile. *Sensor Actuat. a-Phys.* **2004,** *115* (2-3), 440-446.

8. Drew, M. E.; Konicek, A. R.; Jaroenapibal, P.; Carpick, R. W.; Yamakoshi, Y., Nanocrystalline diamond AFM tips for chemical force spectroscopy: fabrication and photochemical functionalization. *J. Mater. Chem.* **2012,** *22* (25), 12682-12688.

9. Giessibl, F. J., Advances in atomic force microscopy. *Rev. Mod. Phys.* **2003,** *75* (3), 949-983.

10. Meyer, G.; Amer, N. M., Novel Optical Approach to Atomic Force Microscopy. *Appl. Phys. Lett.* **1988,** *53* (12), 1045-1047.

11. Binnig, G.; Smith, D. P. E., Single-tube three-dimensional scanner for scanning tunneling microscopy. *Rev. Sci. Instrum.* **1986,** *57* (8), 1688.

12. Cappella, B.; Dietler, G., Force-distance curves by atomic force microscopy. *Surf. Sci. Rep.* **1999,** *34* (1–3), 1-104.

13. Saner, C. K.; Lusker, K. L.; Lejeune, Z. M.; Serem, W. K.; Garno, J. C., Self-assembly of octadecyltrichlorosilane: Surface structures formed using different protocols of particle lithography. *Beilstein J. Nanotechnol.* **2012,** *3*, 114-22.

14. Möller, C.; Allen, M.; Elings, V.; Engel, A.; Müller, D. J., Tapping-Mode Atomic Force Microscopy Produces Faithful High-Resolution Images of Protein Surfaces. *Biophys. J.* **1999,** *77* (2), 1150-1158.

15. Magonov, S. N.; Elings, V.; Whangbo, M. H., Phase imaging and stiffness in tapping-mode atomic force microscopy. *Surf. Sci.* **1997,** *375* (2–3), L385-L391.

16. Cleveland, J. P.; Anczykowski, B.; Schmid, A. E.; Elings, V. B., Energy dissipation in tapping-mode atomic force microscopy. *Appl. Phys. Lett.* **1998,** *72* (20), 2613.

17. Tamayo, J.; García, R., Deformation, Contact Time, and Phase Contrast in Tapping Mode Scanning Force Microscopy. *Langmuir* **1996,** *12* (18), 4430-4435.

18. Tamayo, J.; García, R., Effects of elastic and inelastic interactions on phase contrast images in tapping-mode scanning force microscopy. *Appl. Phys. Lett.* **1997,** *71* (16), 2394.

19. Tamayo, J.; Humphris, A. D. L.; Miles, M. J., Piconewton regime dynamic force microscopy in liquid. *Appl. Phys. Lett.* **2000,** *77* (4), 582.

20. Tamayo, J.; Humphris, A. D. L.; Owen, R. J.; Miles, M. J., High-Q Dynamic Force Microscopy in Liquid and Its Application to Living Cells. *Biophys. J.* **2001,** *81* (1), 526-537.

21. Moreno-Herrero, F.; Colchero, J.; Gómez-Herrero, J.; Baró, A. M., Atomic force microscopy contact, tapping, and jumping modes for imaging biological samples in liquids. *Phys. Rev. E* **2004,** *69* (3).

22. Lyles, V.; Serem, W.; Yu, J.-J.; Garno, J., Surface Characterization Using Atomic Force Microscopy (AFM) in Liquid Environments. In *Surface Science Techniques*, Bracco, G.; Holst, B., Eds. Springer Berlin Heidelberg: 2013; Vol. 51, pp 599-620.

23. Tartibi, M.; Liu, Y. X.; Liu, G. Y.; Komvopoulos, K., Single-cell mechanics – An experimental–computational method for quantifying the membrane–cytoskeleton elasticity of cells. *Acta Biomater.* **2015,** *27*, 224-235.

24. Butt, H.-J.; Cappella, B.; Kappl, M., Force measurements with the atomic force microscope: Technique, interpretation and applications. *Surf. Sci. Rep.* **2005,** *59* (1–6), 1-152.

25. Tian, T.; Singhana, B.; Englade-Franklin, L. E.; Zhai, X.; Lee, T. R.; Garno, J. C., Surface assembly and nanofabrication of 1,1,1-tris(mercaptomethyl)heptadecane on Au(111) studied with time-lapse atomic force microscopy. *Beilstein J. Nanotechnol.* **2014,** *5*, 26-35.

26. Englade-Franklin, L. E.; Saner, C. K.; Garno, J. C., Spatially selective surface platforms for binding fibrinogen prepared by particle lithography with organosilanes. *Interface focus* **2013,** *3* (3), 20120102.

27. Liu, Y. X.; Karsai, A.; Anderson, D. S.; Silva, R. M.; Uyeminami, D. L.; Van Winkle, L. S.; Pinkerton, K. E.; Liu, G.-y., Single-Cell Mechanics Provides an Effective Means To Probe in Vivo Interactions between Alveolar Macrophages and Silver Nanoparticles. *J. Phys. Chem. B* **2015,** *119* (49), 15118-15129.

28. Xu, S.; Liu, G.-Y., Nanometer-Scale Fabrication by Simultaneous Nanoshaving and Molecular Self-Assembly. *Langmuir* **1997,** *13*, 127-129.

29. Pina, C. M.; Pimentel, C.; García-Merino, M., High resolution imaging of the dolomite (104) cleavage surface by atomic force microscopy. *Surf. Sci.* **2010,** *604* (21–22), 1877-1881.

30. Xu, S.; Miller, S.; Laibinis, P. E.; Liu, G.-y., Fabrication of Nanometer Scale Patterns within Self-Assembled Monolayers by Nanografting. *Langmuir* **1999,** *15* (21), 7244-7251.

31. Fukuma, T.; Kobayashi, K.; Matsushige, K.; Yamada, H., True molecular resolution in liquid by frequency-modulation atomic force microscopy. *Appl. Phys. Lett.* **2005,** *86* (19), 193108.

32. Asakawa, H.; Fukuma, T., The molecular-scale arrangement and mechanical strength of phospholipid/cholesterol mixed bilayers investigated by frequency modulation atomic force microscopy in liquid. *Nanotechnology* **2009,** *20* (26), 264008.

33. Fukuma, T., Subnanometer-Resolution Frequency Modulation Atomic Force Microscopy in Liquid for Biological Applications. *Jpn. J. Appl. Phys.* **2009,** *48* (8), 08JA01.

34. Rosa, L. G.; Liang, J., Atomic force microscope nanolithography: dip-pen, nanoshaving, nanografting, tapping mode, electrochemical and thermal nanolithography. *J. Phys.-Condes. Matter* **2009,** *21* (48), 18.

35. Tian, T.; LeJeune, Z.; Serem, W.; Yu, J.-J.; Garno, J., Nanografting: A Method for Bottom-up Fabrication of Designed Nanostructures. In *Tip-Based Nanofabrication*, Tseng, A. A., Ed. Springer New York: 2011; pp 167-205.

36. Brown, T. T.; LeJeune, Z. M.; Liu, K.; Hardin, S.; Li, J. R.; Rupnik, K.; Garno, J. C., Automated Scanning Probe Lithography With n-Alkanethiol Self-Assembled Monolayers on Au(111): Application for Teaching Undergraduate Laboratories. *Jala-J Lab Autom* **2011,** *16* (2), 112-125.

37. Brown, T.; LeJeune, Z. M.; Liu, K.; Li, J. R.; Gurno, J. C., CHED 129-Automated scanning probe lithography with n-alkanethiol self assembled monolayers on Au(111). *Abstr. Pap. Am. Chem. S.* **2009,** *238*.

38. Xu, S.; Laibinis, P. E.; Liu, G. Y., Accelerating the kinetics of thiol self-assembly on gold - A spatial confinement effect. *J. Am. Chem. Soc.* **1998,** *120* (36), 9356-9361.

39. Piner, R. D.; Zhu, J.; Xu, F.; Hong, S.; Mirkin, C. A., "Dip-Pen" Nanolithography. *Science* **1999,** *283* (5402), 661-663.

40. Amro, N. A.; Xu, S.; Liu, G.-y., Patterning Surfaces Using Tip-Directed Displacement and Self-Assembly. *Langmuir* **2000,** *16* (7), 3006-3009.

41. Chen, P.-C.; Liu, G.; Zhou, Y.; Brown, K. A.; Chernyak, N.; Hedrick, J. L.; He, S.; Xie, Z.; Lin, Q.-Y.; Dravid, V. P.; O'Neill-Slawecki, S. A.; Mirkin, C. A., Tip-Directed Synthesis of Multimetallic Nanoparticles. *J. Am. Chem. Soc.* **2015,** *137* (28), 9167-9173.

42. Garcia, R., Local Oxidation Nanolithography. In *Alternative Lithography*, Sotomayor Torres, C., Ed. Springer US: 2003; pp 213-233.

43. Weng, L.; Zhang, L.; Chen, Y. P.; Rokhinson, L. P., Atomic force microscope local oxidation nanolithography of graphene. *Appl. Phys. Lett.* **2008,** *93* (9), 093107.

44. Maynor, B. W.; Li, J.; Lu, C.; Liu, J., Site-Specific Fabrication of Nanoscale Heterostructures: Local Chemical Modification of GaN Nanowires Using Electrochemical Dip-Pen Nanolithography. *J. Am. Chem. Soc.* **2004,** *126* (20), 6409-6413.

45. Paxton, W. F.; Spruell, J. M.; Stoddart, J. F., Heterogeneous Catalysis of a Copper-Coated Atomic Force Microscopy Tip for Direct-Write Click Chemistry. *J. Am. Chem. Soc.* **2009,** *131* (19), 6692-6694.

46. King, W. P.; Kenny, T. W.; Goodson, K. E.; Cross, G. L. W.; Despont, M.; Durig, U. T.; Rothuizen, H.; Binnig, G.; Vettiger, P., Design of atomic force microscope cantilevers for combined thermomechanical writing and thermal reading in array operation. *J. Microelectromech. S.* **2002,** *11* (6), 765-774.

47. Liu, G.-y.; Salmeron, M. B., Reversible Displacement of Chemisorbed n-Alkanethiol Molecules on Au(111) Surface: An Atomic Force Microscopy Study. *Langmuir* **1994,** *10* (2), 367-370.

48. Xiao, X.-D.; Liu, G.-y.; Charych, D. H.; Salmeron, M., Preparation, Structure, and Mechanical Stability of Alkylsilane Monolayers on Mica. *Langmuir* **1995,** *11* (5), 1600-1604.

49. Rosa, L. G.; Jiang, J.; Lima, O. V.; Xiao, J.; Utreras, E.; Dowben, P. A.; Tan, L., Selective nanoshaving of self-assembled monolayers of 2-(4-pyridylethyl)triethoxysilane. *Mater. Lett.* **2009,** *63* (12), 961-964.

50. Verberne-Sutton, S. D.; Quarels, R. D.; Zhai, X.; Garno, J. C.; Ragains, J. R., Application of visible light photocatalysis with particle lithography to generate polynitrophenylene nanostructures. *J. Am. Chem. Soc.* **2014,** *136* (41), 14438-44.

51. Shao, J.; Josephs, E. A.; Lee, C.; Lopez, A.; Ye, T., Electrochemical Etching of Gold within Nanoshaved Self-Assembled Monolayers. *ACS Nano* **2013,** *7* (6), 5421-5429.

52. Greene, M. E.; Kinser, C. R.; Kramer, D. E.; Pingree, L. S. C.; Hersam, M. C., Application of scanning probe microscopy to the characterization and fabrication of hybrid nanomaterials. *Microsc. Res. Techniq.* **2004,** *64* (5-6), 415-434.

53. Meuse, C. W., Infrared Spectroscopic Ellipsometry of Self-Assembled Monolayers. *Langmuir* **2000,** *16* (24), 9483-9487.

54. Godin, M.; Williams, P. J.; Tabard-Cossa, V.; Laroche, O.; Beaulieu, L. Y.; Lennox, R. B.; Grütter, P., Surface Stress, Kinetics, and Structure of Alkanethiol Self-Assembled Monolayers. *Langmuir* **2004,** *20* (17), 7090-7096.

55. Kim, J.; Uchida, H.; Honda, N.; Hashizume, N.; Hashimoto, Y.; Kim, H.; Nishimura, K.; Inoue, M., Tip-Height-Controlled Removal of Alkanethiol Self-Assembled Monolayer on Au(111) Surface. *Jpn. J. Appl. Phys.* **2003,** *42* (Part 1, No. 7B), 4770-4772.

56. Liu, M.; Amro, N. A.; Liu, G. Y., Nanografting for surface physical chemistry. *Annu. Rev. Phys. Chem.* **2008,** *59*, 367-386.

57. Murrell, M. P.; Welland, M. E.; O'Shea, S. J.; Wong, T. M. H.; Barnes, J. R.; McKinnon, A. W.; Heyns, M.; Verhaverbeke, S., Spatially resolved electrical measurements of SiO2 gate oxides using atomic force microscopy. *Appl. Phys. Lett.* **1993,** *62* (7), 786.

58. Oshea, S. J.; Atta, R. M.; Murrell, M. P.; Welland, M. E., Conducting Atomic-Force Microscopy Study of Silicon Dioxide Breakdown. *J. Vac. Sci. Technol. B* **1995,** *13* (5), 1945-1952.

59. Klein, D. L.; Mceuen, P. L., Conducting Atomic-Force Microscopy of Alkane Layers on Graphite. *Appl. Phys. Lett.* **1995,** *66* (19), 2478-2480.

60. Olbrich, A.; Ebersberger, B.; Boit, C., Conducting atomic force microscopy for nanoscale electrical characterization of thin SiO[sub 2]. *Appl. Phys. Lett.* **1998,** *73* (21), 3114.

61. Leatherman, G.; Durantini, E. N.; Gust, D.; Moore, T. A.; Moore, A. L.; Stone, S.; Zhou, Z.; Rez, P.; Liu, Y. Z.; Lindsay, S. M., Carotene as a molecular wire: Conducting atomic force microscopy. *J. Phys. Chem. B* **1999,** *103* (20), 4006-4010.

62. Lang, K. M.; Hite, D. A.; Simmonds, R. W.; McDermott, R.; Pappas, D. P.; Martinis, J. M., Conducting atomic force microscopy for nanoscale tunnel barrier characterization. *Rev. Sci. Instrum.* **2004,** *75* (8), 2726-2731.

63. Ishida, T.; Mizutani, W.; Aya, Y.; Ogiso, H.; Sasaki, S.; Tokumoto, H., Electrical conduction of conjugated molecular SAMs studied by conductive atomic force microscopy. *J. Phys. Chem. B* **2002,** *106* (23), 5886-5892.

64. Kim, J.; Cho, S.; Choi, S.; Baek, S.; Lee, D.; Kim, O.; Park, S. M.; Ree, M., Novel electrical properties of nanoscale thin films of a semiconducting polymer: Quantitative current-sensing AFM analysis. *Langmuir* **2007,** *23* (17), 9024-9030.

65. Fumagalli, L.; Ferrari, G.; Sampietro, M.; Casuso, I.; Martinez, E.; Samitier, J.; Gomila, G., Nanoscale capacitance imaging with attofarad resolution using ac current sensing atomic force microscopy. *Nanotechnology* **2006,** *17* (18), 4581-7.

66. Gosvami, N.; Lau, K. H. A.; Sinha, S. K.; O'Shea, S. J., Effect of end groups on contact resistance of alkanethiol based metal-molecule-metal junctions using current sensing AFM. *Appl. Surf. Sci.* **2006,** *252* (11), 3956-3960.

67. Dai, H. J.; Wong, E. W.; Lieber, C. M., Probing electrical transport in nanomaterials: Conductivity of individual carbon nanotubes. *Science* **1996,** *272* (5261), 523-526.

68. Tanaka, H.; Yajima, T.; Matsumoto, T.; Otsuka, Y.; Ogawa, T., Porphyrin molecular nanodevices wired using single-walled carbon nanotubes. *Adv. Mater.* **2006,** *18* (11), 1411-+.

69. Kelley, T. W.; Frisbie, C. D., Point contact current-voltage measurements on individual organic semiconductor grains by conducting probe atomic force microscopy. *J. Vac. Sci. Technol. B* **2000,** *18* (2), 632-635.

70. Wold, D. J.; Frisbie, C. D., Formation of metal-molecule-metal tunnel junctions: Microcontacts to alkanethiol monolayers with a conducting AFM tip. *J. Am. Chem. Soc.* **2000,** *122* (12), 2970-2971.

71. Wold, D. J.; Frisbie, C. D., Fabrication and characterization of metal-molecule-metal junctions by conducting probe atomic force microscopy. *J. Am. Chem. Soc.* **2001,** *123* (23), 5549-5556.

72. Cui, X. D.; Primak, A.; Zarate, X.; Tomfohr, J.; Sankey, O. F.; Moore, A. L.; Moore, T. A.; Gust, D.; Harris, G.; Lindsay, S. M., Reproducible measurement of single-molecule conductivity. *Science* **2001,** *294* (5542), 571-574.

73. Kelley, T. W.; Granstrom, E. L.; Frisbie, C. D., Conducting probe atomic force microscopy: A characterization tool for molecular electronics. *Adv. Mater.* **1999,** *11* (3), 261-+.

74. Ramachandran, G. K.; Tomfohr, J. K.; Li, J.; Sankey, O. F.; Zarate, X.; Primak, A.; Terazono, Y.; Moore, T. A.; Moore, A. L.; Gust, D.; Nagahara, L. A.; Lindsay, S. M., Electron Transport Properties of a Carotene Molecule in a Metal−(Single Molecule)−Metal Junction. *J. Phys. Chem. B* **2003,** *107* (25), 6162-6169.

75. Lee, H. J.; Lee, J.; Park, S.-M., Electrochemistry of Conductive Polymers. 45. Nanoscale Conductivity of PEDOT and PEDOT:PSS Composite Films Studied by Current-Sensing AFM. *J. Phys. Chem. B* **2010,** *114* (8), 2660-2666.

76. Giersig, M.; Mulvaney, P., PREPARATION OF ORDERED COLLOID MONOLAYERS BY ELECTROPHORETIC DEPOSITION. *Langmuir* **1993,** *9* (12), 3408-3413.

77. Ulman, A., Formation and structure of self-assembled monolayers. *Chem. Rev.* **1996,** *96* (4), 1533-1554.

78. Schreiber, F., Structure and growth of self-assembling monolayers. *Prog. Surf. Sci.* **2000,** *65* (5-8), 151-256.

79. Duwez, A. S., Exploiting electron spectroscopies to probe the structure and organization of self-assembled monolayers: a review. *J. Electron Spectrosc.* **2004,** *134* (2-3), 97-138.

80. Chinwangso, P.; Jamison, A. C.; Lee, T. R., Multidentate Adsorbates for Self-Assembled Monolayer Films. *Accounts Chem. Res.* **2011,** *44* (7), 511-519.

81. Bain, C. D.; Troughton, E. B.; Tao, Y. T.; Evall, J.; Whitesides, G. M.; Nuzzo, R. G., Formation of Monolayer Films by the Spontaneous Assembly of Organic Thiols from Solution onto Gold. *J. Am. Chem. Soc.* **1989,** *111* (1), 321-335.

82. Porter, M. D.; Bright, T. B.; Allara, D. L.; Chidsey, C. E. D., Spontaneously Organized Molecular Assemblies .4. Structural Characterization of Normal-Alkyl Thiol Monolayers on Gold by Optical Ellipsometry, Infrared-Spectroscopy, and Electrochemistry. *J. Am. Chem. Soc.* **1987,** *109* (12), 3559-3568.

83. Poirier, G. E.; Tarlov, M. J.; Rushmeier, H. E., Two-Dimensional Liquid Phase and the px.sqroot.3 Phase of Alkanethiol Self-Assembled Monolayers on Au(111). *Langmuir* **1994,** *10* (10), 3383-3386.

84. Srisombat, L.; Jamison, A. C.; Lee, T. R., Stability: A key issue for self-assembled monolayers on gold as thin-film coatings and nanoparticle protectants. *Colloid Surface A* **2011,** *390* (1-3), 1-19.

85. Zhang, S. S.; Leem, G.; Srisombat, L. O.; Lee, T. R., Rationally designed ligands that inhibit the aggregation of large gold nanoparticles in solution. *J. Am. Chem. Soc.* **2008,** *130* (1), 113-120.

86. Biener, M. M.; Biener, J.; Friend, C. M., Revisiting the S-Au(111) interaction: Static or dynamic? *Langmuir* **2005,** *21* (5), 1668-1671.

87. Bruno, G.; Babudri, F.; Operamolla, A.; Bianco, G. V.; Losurdo, M.; Giangregorio, M. M.; Hassan Omar, O.; Mavelli, F.; Farinola, G. M.; Capezzuto, P.; Naso, F., Tailoring Density and Optical and Thermal Behavior of Gold Surfaces and Nanoparticles Exploiting Aromatic Dithiols. *Langmuir* **2010,** *26* (11), 8430-8440.

88. Ramachandra, S.; Polo, F.; Edafe, F.; Schuermann, K. C.; Nijhuis, C. A.; Belser, P.; Reus, W. F.; Whitesides, G. M.; De Cola, L., Luminescent acetylthiol derivative tripodal osmium(II) and iridium(III) complexes: Spectroscopy in solution and on surfaces. *Pure. Appl. Chem.* **2011,** *83* (4), 779-799.

89. Sakata, T.; Maruyama, S.; Ueda, A.; Otsuka, H.; Miyahara, Y., Stable immobilization of an oligonucleotide probe on a gold substrate using tripodal thiol derivatives. *Langmuir* **2007,** *23* (5), 2269-2272.

90. Wei, L.; Padmaja, K.; Youngblood, W. J.; Lysenko, A. B.; Lindsey, J. S.; Bocian, D. F., Diverse Redox-Active Molecules Bearing Identical Thiol-Terminated Tripodal Tethers for Studies of Molecular Information Storage. *J. Org. Chem.* **2003,** *69* (5), 1461-1469.

91. Hirayama, D.; Takimiya, K.; Aso, Y.; Otsubo, T.; Hasobe, T.; Yamada, H.; Imahori, H.; Fukuzumi, S.; Sakata, Y., Large photocurrent generation of gold electrodes modified with 60 fullerene-linked oligothiophenes bearing a tripodal rigid anchor. *J. Am. Chem. Soc.* **2002,** *124* (4), 532-533.

92. Weidner, T.; Ballav, N.; Siemeling, U.; Troegel, D.; Walter, T.; Tacke, R.; Castner, D. G.; Zharnikov, M., Tripodal Binding Units for Self-Assembled Monolayers on Gold: A Comparison of Thiol and Thioether Headgroups. *J. Phys. Chem. C* **2009,** *113* (45), 19609-19617.

93. Lewandowski, B. R.; Kelley, A. T.; Singleton, R.; Li, J.-R.; Lowry, M.; Warner, I. M.; Garno, J. C., Nanostructures of Cysteine-Coated CdS Nanoparticles Produced with "Two-Particle" Lithography. *J. Phys. Chem. C* **2009,** *113* (15), 5933-5940.

94. Lusker, K. L.; Li, J.-R.; Garno, J. C., Nanostructures of Functionalized Gold Nanoparticles Prepared by Particle Lithography with Organosilanes. *Langmuir* **2011,** *27* (21), 13269-13275.

95. Zhang, X. Y.; Yonzon, C. R.; Van Duyne, R. P., Nanosphere lithography fabricated plasmonic materials and their applications. *J. Mater. Res.* **2006,** *21* (5), 1083-1092.

96. Isa, L.; Kumar, K.; Müller, M.; Grolig, J.; Textor, M.; Reimhult, E., Particle Lithography from Colloidal Self-Assembly at Liquid−Liquid Interfaces. *ACS Nano* **2010,** *4* (10), 5665-5670.

97. Chan, G. H.; Zhao, J.; Hicks, E. M.; Schatz, G. C.; Van Duyne, R. P., Plasmonic properties of copper nanoparticles fabricated by nanosphere lithography. *Nano Lett.* **2007,** *7* (7), 1947-1952.

98. Verberne-Sutton, S. D.; Quarels, R. D.; Zhai, X.; Garno, J. C.; Ragains, J. R., Application of Visible Light Photocatalysis with Particle Lithography To Generate Polynitrophenylene Nanostructures. *J. Am. Chem. Soc.* **2014,** *136* (41), 14438-14444.

99. Tian, T.; LeJeune, Z. M.; Garno, J. C., Directed surface assembly of 4-(chloromethyl)phenyltrichlorosilane: self-polymerization within spatially confined sites of Si(111) viewed by atomic force microscopy. *Langmuir* **2013,** *29* (22), 6529-36.

100. Chinwangso, P.; Jamison, A. C.; Lee, T. R., Multidentate Adsorbates for Self-Assembled Monolayer Films. *Acc. Chem. Res.* **2011,** *44* (7), 511-519.

101. Carbonell, L.; Whelan, C. M.; Kinsella, M.; Maex, K., A thermal stability study of alkane and aromatic thiolate self-assembled monolayers on copper surfaces. *Superlattices Microst.* **2004,** *36* (1-3), 149-160.

102. Ebbens, S.; Hutt, D.; Liu, C., The Thermal Stability of Alkanethiol Self-Assembled Monolayers on Copper for Fluxless Soldering Applications. *IEEE Trans Compon Pack T* **2010,** *33* (2), 251-259.

103. Hakamada, M.; Takahashi, M.; Furukawa, T.; Tajima, K.; Yoshimura, K.; Chino, Y.; Mabuchi, M., Electrochemical stability of self-assembled monolayers on nanoporous Au. *Phys. Chem. Chem. Phys.* **2011,** *13* (26), 12277-12284.

104. Ito, E.; Kang, H.; Lee, D.; Park, J. B.; Hara, M.; Noh, J., Spontaneous desorption and phase transitions of self-assembled alkanethiol and alicyclic thiol monolayers chemisorbed on Au(1 1 1) in ultrahigh vacuum at room temperature. *J. Colloid. Interf. Sci.* **2013,** *394*, 522-529.

105. Li, J.; Ang, X. F.; Lee, K. H.; Romanato, F.; Wong, C. C., In-Situ Monitoring of the Thermal Desorption of Alkanethiols with Surface Plasmon Resonance Spectroscopy (SPRS). *J Nanosci. Nanotechnol.* **2010,** *10* (7), 4624-4628.

106. Ramin, L.; Jabbarzadeh, A., Odd-Even Effects on the Structure, Stability, and Phase Transition of Alkanethiol Self-Assembled Monolayers. *Langmuir* **2011,** *27* (16), 9748-9759.

107. Srisombat, L.-o.; Zhang, S.; Lee, T. R., Thermal Stability of Mono-, Bis-, and Tris-Chelating Alkanethiol Films Assembled on Gold Nanoparticles and Evaporated "Flat" Gold. *Langmuir* **2010,** *26* (1), 41-46.

108. Stettner, J.; Winkler, A., Characterization of Alkanethiol Self-Assembled Monolayers on Gold by Thermal Desorption Spectroscopy. *Langmuir* **2010,** *26* (12), 9659-9665.

109. Subramanian, S.; Sampath, S., Enhanced thermal stability and structural ordering in short chain n-alkanethiol monolayers on gold probed by vibrational spectroscopy and EQCM. *Anal. Bioanal. Chem.* **2007,** *388* (1), 135-145.

110. Srisombat, L. O.; Park, J. S.; Zhang, S.; Lee, T. R., Preparation, characterization, and chemical stability of gold nanoparticles coated with mono-, bis-, and tris-chelating alkanethiols. *Langmuir* **2008,** *24* (15), 7750-7754.

111. Srisombat, L.; Jamison, A. C.; Lee, T. R., Stability: A key issue for self-assembled monolayers on gold as thin-film coatings and nanoparticle protectants. *Colloids Surf. A* **2011,** *390* (1-3), 1-19.

112. Zhang, S. S.; Leem, G.; Srisombat, L. O.; Lee, T. R., Rationally designed ligands that inhibit the aggregation of large gold nanoparticles in solution. *J. Am. Chem. Soc.* **2008,** *130* (1), 113-120.

113. Lee, H. J.; Jamison, A. C.; Yuan, Y.; Li, C.-H.; Rittikulsittichai, S.; Rusakova, I.; Lee, T. R., Robust Carboxylic Acid-Terminated Organic Thin Films and Nanoparticle Protectants Generated from Bidentate Alkanethiols. *Langmuir* **2013,** *29* (33), 10432-10439.

114. Garg, N.; Lee, T. R., Self-Assembled Monolayers Based on Chelating Aromatic Dithiols on Gold. *Langmuir* **1998,** *14*, 3815-3819.

115. Wadu-Mesthrige, K.; Amro, N. A.; Garno, J. C.; Xu, S.; Liu, G.-Y., Fabrication of nanometer-sized protein patterns using AFM and selective immobilization. *Biophys. J.* **2001,** *80*, 1891-1899.

116. Garno, J. C.; Zangmeister, C. D.; Batteas, J. D., Directed electroless growth of metal nanostructures on patterned self-assembled monolayers. *Langmuir* **2007,** *23*, 7874-7879.

117. Kelley, A. T.; Ngunjiri, J. N.; Serem, W. K.; Lawrence, S. O.; Yu, J. J.; Crowe, W. E.; Garno, J. C., Applying AFM-Based Nanofabrication for Measuring the Thickness of Nanopatterns: The Role of Head Groups in the Vertical Self-Assembly of omega-Functionalized n-Alkanethiols. *Langmuir* **2010,** *26* (5), 3040-3049.

118. Yu, J. H.; Ngunjiri, J. N.; Kelley, A. T.; Gano, J. C., Nanografting versus Solution Self-Assembly of alpha,omega-Alkanedithiols on Au(111) Investigated by AFM. *Langmuir* **2008,** *24* (20), 11661-11668.

119. Brower, T. L.; Garno, J. C.; Ulman, A.; Liu, G.-Y.; Yan, C.; Golzhauser, A.; Grunze, M., Self-assembled multilayers of 4,4'-dimercaptobiphenyl formed by Cu(II) oxidation. *Langmuir* **2002,** *18*, 6207-6216.

120. Torun, B.; Ozkaya, B.; Grundmeier, G., Atomic Force Microscopy (AFM)-Based Nanografting for the Study of Self-Assembled Monolayer Formation of Organophosphonic Acids on Al2O3 Single-Crystal Surfaces. *Langmuir* **2012,** *28* (17), 6919-6927.

121. Te Riet, J.; Smit, T.; Gerritsen, J. W.; Cambi, A.; Elemans, J. A. A. W.; Figdor, C. G.; Speller, S., Molecular Friction as a Tool to Identify Functionalized Alkanethiols. *Langmuir* **2010,** *26* (9), 6357-6366.

122. te Riet, J.; Smit, T.; Coenen, M. J. J.; Gerritsen, J. W.; Cambi, A.; Elemans, J. A. A. W.; Speller, S.; Figdor, C. G., AFM topography and friction studies of hydrogen-bonded bilayers of functionalized alkanethiols. *Soft Matter* **2010,** *6* (15), 3450-3454.

123. Liu, M.; Amro, N. A.; Chow, C. X.; Liu, G.-Y., Production of Nanostructures of DNA on Surfaces. *Nano Lett.*. **2002,** *2*, 863-867.

124. Liang, J.; Castronovo, M.; Scoles, G., DNA as Invisible Ink for AFM Nanolithography. *J. Am. Chem. Soc.* **2011,** *134*, 39-42.

125. Case, M. A.; McLendon, G. L.; Hu, Y.; Vanderlick, T. K.; Scoles, G., Using Nanografting to Achieve Directed Assembly of de novo Designed Metalloproteins on Gold. *Nano Lett.* **2003,** *3*, 425-429.

126. Ngunjiri, J. N.; Garno, J. C., AFM-based lithography for nanoscale protein assays. *Anal. Chem.* **2008,** *80*, 1361-1369.

127. Li, J. R.; Garno, J. C., Elucidating the Role of Surface Hydrolysis in Preparing Organosilane Nanostructures via Particle Lithography. *Nano Lett.* **2008,** *8*, 1916-1922.

128. Bu, D.; Mullen, T. J.; Liu, G.-y., Regulation of Local Structure and Composition of Binary Disulfide and Thiol Self-Assembled Monolayers Using Nanografting. *ACS Nano* **2010,** *4* (11), 6863-6873.

129. Hegner, M.; Wagner, P.; Semenza, G., Ultralarge atomically flat template-stripped Au surfaces for scanning probe microscopy. *Surf. Sci.* **1993,** *291* (1–2), 39-46.

130. Necas, D.; Klapetek, P., Gwyddion: an open-source software for SPM data analysis. *Cent. Eur. J. Phys.* **2012,** *10* (1), 181-188.

131. Xu, S.; Miller, S.; Laibinish, P. E.; Liu, G.-Y., Fabrication of Nanometer Scale Patterns within Self-Assembled Monolayers by Nanografting. *Langmuir* **1999,** *15*, 7244-7251.

132. Li, J.-R.; Lusker, K. L.; Yu, J.-J.; Garno, J. C., Engineering the Spatial Selectivity of Surfaces at the Nanoscale Using Particle Lithography Combined with Vapor Deposition of Organosilanes. *ACS Nano* **2009,** *3* (7), 2023-2035.

133. Aragones, A. C.; Darwish, N.; Saletra, W. J.; Perez-Garcia, L.; Sanz, F.; Puigmarti-Luis, J.; Amabilino, D. B.; Diez-Perez, I., Highly conductive single-molecule wires with controlled orientation by coordination of metalloporphyrins. *Nano Lett.* **2014,** *14* (8), 4751-6.

134. Bhupathiraju, N. V.; Rizvi, W.; Batteas, J. D.; Drain, C. M., Fluorinated porphyrinoids as efficient platforms for new photonic materials, sensors, and therapeutics. *Organic & biomolecular chemistry* **2015,** *14* (2), 389-408.

135. Hasobe, T., Photo- and electro-functional self-assembled architectures of porphyrins. *Phys. Chem. Chem. Phys.* **2012,** *14* (46), 15975-87.

136. Ladomenou, K.; Nikolaou, V.; Charalambidis, G.; Coutsolelos, A. G., "Click"-reaction: An alternative tool for new architectures of porphyrin based derivatives. *Coord. Chem. Rev.* **2016,** *306*, 1-42.

137. Medforth, C. J.; Wang, Z.; Martin, K. E.; Song, Y.; Jacobsen, J. L.; Shelnutt, J. A., Self-assembled porphyrin nanostructures. *Chem. Commun.* **2009,** (47), 7261-7277.

138. Dyer, M. S.; Robin, A.; Haq, S.; Raval, R.; Persson, M.; Klimeš, J., Understanding the Interaction of the Porphyrin Macrocycle to Reactive Metal Substrates: Structure, Bonding, and Adatom Capture. *ACS Nano* **2011,** *5* (3), 1831-1838.

139. Wan, Y.; Stradomska, A.; Fong, S.; Guo, Z.; Schaller, R. D.; Wiederrecht, G. P.; Knoester, J.; Huang, L., Exciton Level Structure and Dynamics in Tubular Porphyrin Aggregates. *J. Phys. Chem. C* **2014,** *118* (43), 24854-24865.

140. Cai, J.; Chen, H.; Huang, J.; Wang, J.; Tian, D.; Dong, H.; Jiang, L., Controlled self-assembly and photovoltaic characteristics of porphyrin derivatives on a silicon surface at solid-liquid interfaces. *Soft Matter* **2014,** *10* (15), 2612-8.

141. Jurow, M.; Schuckman, A. E.; Batteas, J. D.; Drain, C. M., Porphyrins as Molecular Electronic Components of Functional Devices. *Coord. Chem. Rev.* **2010,** *254* (19-20), 2297-2310.

142. Vijayaraghavan, S.; Ecija, D.; Auwarter, W.; Joshi, S.; Seufert, K.; Seitsonen, A. P.; Tashiro, K.; Barth, J. V., Selective Supramolecular Fullerene-Porphyrin Interactions and Switching in Surface-Confined C-60-Ce(TPP)(2) Dyads. *Nano Lett.* **2012,** *12* (8), 4077-4083.

143. Grill, L.; Rieder, K. H.; Moresco, F.; Stojkovic, S.; Gourdon, A.; Joachim, C., Exploring the interatomic forces between tip and single molecules during STM manipulation. *Nano Lett.* **2006,** *6* (12), 2685-2689.

144. Battacharyya, S.; Kibel, A.; Kodis, G.; Liddell, P. A.; Gervaldo, M.; Gust, D.; Lindsay, S., Optical Modulation of Molecular Conductance. *Nano Lett.* **2011,** *11* (7), 2709-2714.

145. Xi, W.; Zhang, W.; An, B. K.; Burn, P. L.; Davis, J. J., Tunnelling conductance of vectorial porphyrin monolayers. *J. Mater. Chem.* **2008,** *18* (26), 3109-3120.

146. Yan, S. C.; Ding, Z. J.; Xie, N.; Gong, H. Q.; Sun, Q.; Guo, Y.; Shan, X. Y.; Meng, S.; Lu, X. H., Turning on and off the Rotational Oscillation of a Single Porphine Molecule by Molecular Charge State. *ACS Nano* **2012,** *6* (5), 4132-4136.

147. Joshi, S.; Bischoff, F.; Koitz, R.; Ecija, D.; Seufert, K.; Seitsonen, A. P.; Hutter, J.; Diller, K.; Urgel, J. I.; Sachdev, H.; Barth, J. V.; Auwarter, W., Control of Molecular Organization and Energy Level Alignment by an Electronically Nanopatterned Boron Nitride Template. *ACS Nano* **2014,** *8* (1), 430-442.

148. Siles, P. F.; Bufon, C. C. B.; Grimm, D.; Jalil, A. R.; Mende, C.; Lungwitz, F.; Salvan, G.; Zahn, D. R. T.; Lang, H.; Schmidt, O. G., Morphology and local transport characteristics of metalloporphyrin thin films. *Org. Electron* **2014,** *15* (7), 1432-1439.

149. Wang, X. Y.; Wang, G. C.; Lewis, K. M., High rectification ratios of Fe-porphyrin molecules on Au facets. *Mater. Chem. Phys.* **2012,** *136* (1), 190-195.

150. Mou, C. Y.; Yuan, W. L.; Tsai, I. S.; O'Rear, E. A.; Barraza, H., Conductance measurement by two-line probe method of polypyrrole nano-films formed on mica by admicellar polymerization. *Thin Solid Films* **2008,** *516* (23), 8752-8756.

151. Bumm, L. A.; Arnold, J. J.; Dunbar, T. D.; Allara, D. L.; Weiss, P. S., Electron transfer through organic molecules. *J. Phys. Chem. B* **1999,** *103* (38), 8122-8127.

152. Wold, D. J.; Frisbie, C. D., Fabrication and characterization of metal-molecule-metal junctions by conducting probe atomic force microscopy. *J. Am. Chem. Soc.* **2001,** *123* (23), 5549-5556.

153. Salmeron, M.; Neubauer, G.; Folch, A.; Tomitori, M.; Ogletree, D. F.; Sautet, P., Viscoelastic and Electrical-Properties of Self-Assembled Monolayers on Au(111) Films. *Langmuir* **1993,** *9* (12), 3600-3611.

154. Wold, D. J.; Frisbie, C. D., Formation of metal-molecule-metal tunnel junctions: Microcontacts to alkanethiol monolayers with a conducting AFM tip. *J. Am. Chem. Soc.* **2000,** *122* (12), 2970-2971.

155. Cui, X. D.; Zarate, X.; Tomfohr, J.; Sankey, O. F.; Primak, A.; Moore, A. L.; Moore, T. A.; Gust, D.; Harris, G.; Lindsay, S. M., Making electrical contacts to molecular monolayers. *Nanotechnology* **2002,** *13* (1), 5-14.

156. Wold, D. J.; Haag, R.; Rampi, M. A.; Frisbie, C. D., Distance Dependence of Electron Tunneling through Self-Assembled Monolayers Measured by Conducting Probe Atomic Force Microscopy: Unsaturated versus Saturated Molecular Junctions. *J. Phys. Chem. B* **2002,** *106* (11), 2813-2816.

157. Ferreira, Q.; Alcacer, L.; Morgado, J., Stepwise preparation and characterization of molecular wires made of zinc octaethylporphyrin complexes bridged by 4,4'-bipyridine on HOPG. *Nanotechnology* **2011,** *22* (43), 435604.

158. Hoang, M. H.; Kim, Y.; Kim, S. J.; Choi, D. H.; Lee, S. J., High-Performance Single-Crystal-Based Organic Field-Effect Transistors from pi-Extended Porphyrin Derivatives. *Chem.-Eur. J.* **2011,** *17* (28), 7772-7776.

159. Kang, B. K.; Aratani, N.; Lim, J. K.; Kim, D.; Osuka, A.; Yoo, K. H., Electrical transport properties and their reproducibility for linear porphyrin arrays. *Mat. Sci. Eng. C.-Bio. S.* **2006,** *26* (5-7), 1023-1027.

160. Yoon, D. H.; Lee, S. B.; Yoo, K. H.; Kim, J.; Lim, J. K.; Aratani, N.; Tsuda, A.; Osuka, A.; Kim, D., Electrical conduction through linear porphyrin arrays. *J. Am. Chem. Soc.* **2003,** *125* (36), 11062-11064.

161. Schwab, A. D.; Smith, D. E.; Bond-Watts, B.; Johnston, D. E.; Hone, J.; Johnson, A. T.; de Paula, J. C.; Smith, W. F., Photoconductivity of Self-Assembled Porphyrin Nanorods. *Nano Lett.* **2004,** *4* (7), 1261-1265.

162. Friesen, B. A.; Wiggins, B.; McHale, J. L.; Mazur, U.; Hipps, K. W., Differing HOMO and LUMO Mediated Conduction in a Porphyrin Nanorod. *J. Am. Chem. Soc.* **2010,** *132* (25), 8554-8556.

163. Schwab, A. D.; Smith, D. E.; Rich, C. S.; Young, E. R.; Smith, W. F.; de Paula, J. C., Porphyrin Nanorods. *J. Phys. Chem. B* **2003,** *107* (41), 11339-11345.

164. So, M. H.; Roy, V. A. L.; Xu, Z. X.; Chui, S. S. Y.; Yuen, M. Y.; Ho, C. M.; Che, C. M., Controlled Self-Assembly of Functional Metal Octaethylporphyrin 1D Nanowires by Solution-Phase Precipitative Method. *Chem.-Asian J.* **2008,** *3* (11), 1968-1978.

165. Lu, G.; Chen, Y.; Zhang, Y.; Bao, M.; Bian, Y.; Li, X.; Jiang, J., Morphology Controlled Self-Assembled Nanostructures of Sandwich Mixed (Phthalocyaninato)(Porphyrinato) Europium Triple-Deckers. Effect of Hydrogen Bonding on Tuning the Intermolecular Interaction. *J. Am. Chem. Soc.* **2008,** *130* (35), 11623-11630.

166. Laschat, S.; Baro, A.; Steinke, N.; Giesselmann, F.; Hägele, C.; Scalia, G.; Judele, R.; Kapatsina, E.; Sauer, S.; Schreivogel, A.; Tosoni, M., Diskotische Flüssigkristalle: Von der maßgeschneiderten Synthese zur Kunststoffelektronik. *Angewandte Chemie* **2007,** *119* (26), 4916-4973.

167. Li, J. R.; Garno, J. C., Nanostructures of Octadecyltrisiloxane Self-Assembled Monolayers Produced on Au(111) Using Particle Lithography. *ACS Appl. Mater. Inter.* **2009,** *1* (4), 969-976.

168. Lusker, K. L.; Yu, J.-J.; Garno, J. C., Particle Lithography with Vapor Deposition of Organosilanes: A Molecular Toolkit for Studying Confined Surface Reactions in Nanoscale Liquid Volumes. *Thin Solid Films* **2011,** *7* (519), 5223-5229.

169. Tian, T.; LeJeune, Z. M.; Garno, J. C., Directed surface assembly of 4-(chloromethyl)-phenyltrichlorosilane: Self-polymerization within spatially-confined sites of Si(111) viewed by atomic force microscopy. *Langmuir* **2013,** *29*, 6529-6536.

170. Lu, L.; Lahasky, S. H.; Zhang, D.; Garno, J. C., Directed Growth of Polymer Nanorods Using Surface-Initiated Ring-Opening Polymerization of N-Allyl N-Carboxyanhydride. *ACS Appl. Mater. Inter.* **2016,** *8* (6), 4014-22.

171. Loiacono, M. J.; Granstrom, E. L.; Frisbie, C. D., Investigation of charge transport in thin, doped sexithiophene crystals by conducting probe atomic force microscopy. *J. Phys. Chem. B* **1998,** *102* (10), 1679-1688.

172. Yan, S.; Ding, Z.; Xie, N.; Gong, H.; Sun, Q.; Guo, Y.; Shan, X.; Meng, S.; Lu, X., Turning on and off the Rotational Oscillation of a Single Porphine Molecule by Molecular Charge State. *ACS Nano* **2012,** *6* (5), 4132-4136.

173. Adinehnia, M.; Mazur, U.; Hipps, K. W., Predicting the Size Distribution in Crystallization of TSPP:TMPyP Binary Porphyrin Nanostructures in a Batch Desupersaturation Experiment. *Cryst. Growth Des.* **2014,** *14* (12), 6599-6606.

174. Guo, P.; Chen, P.; Liu, M., One-dimensional porphyrin nanoassemblies assisted via graphene oxide: sheetlike functional surfactant and enhanced photocatalytic behaviors. *ACS Appl. Mater. Inter.* **2013,** *5* (11), 5336-45.

175. Guo, P.; Zhao, G.; Chen, P.; Lei, B.; Jiang, L.; Zhang, H.; Hu, W.; Liu, M., Porphyrin Nanoassemblies via Surfactant-Assisted Assembly and Single Nanofiber Nanoelectronic Sensors for High-Performance H2O2 Vapor Sensing. *ACS Nano* **2014,** *8* (4), 3402-3411.

176. Arai, Y.; Segawa, H., J-aggregation of protonated meso-tetrakis(sulfonatothienyl)porphyrin isomers: morphological selection of self-assembled nanostructures from structurally similar zwitterionic porphyrins. *Chem. Commun. (Camb.)* **2010,** *46* (24), 4279-81.

177. Arai, Y.; Tsuzuki, K.; Segawa, H., Homogeneously mixed porphyrin J-aggregates with rod-shaped nanostructures via zwitterionic self-assembly. *Phys. Chem. Chem. Phys.* **2012,** *14* (3), 1270-6.

178. Lee, J. H.; Lee, S. J., Microscopic crystalline rods from the self-assembly of mixed porphyrin building blocks. *Inorg. Chem. Commun.* **2011,** *14* (6), 1014-1017.

179. Wan, Y.; Stradomska, A.; Fong, S.; Guo, Z.; Schaller, R. D.; Wiederrecht, G. P.; Knoester, J.; Huang, L., Exciton Level Structure and Dynamics in Tubular Porphyrin Aggregates. *J. Phys. Chem. C* **2014,** *118* (43), 24854-24865.

180. Rotomskis, R.; Augulis, R.; Snitka, V.; Valiokas, R.; Liedberg, B., Hierarchical Structure of TPPS4 J-Aggregates on Substrate Revealed by Atomic Force Microscopy. *J. Phys. Chem. B* **2004,** *108* (9), 2833-2838.

181. Jacobsen, J. L.; Berget, P. E.; Varela, M. C.; Vu, T.; Schore, N. E.; Martin, K. E.; Shelnutt, J. A.; Santos, L. M.; Medforth, C. J., Synthesis and nanostructures of 5,10,15,20-tetrakis(4-piperidyl)porphyrin. *Tetrahedron* **2013,** *69* (48), 10507-10515.

182. Mongwaketsi, N.; Khamlich, S.; Klumperman, B.; Sparrow, R.; Maaza, M., Synthesis and characterization of porphyrin nanotubes/rods for solar radiation harvesting and solar cells. *Physica B: Condensed Matter* **2012,** *407* (10), 1615-1619.

183. Vlaming, S. M.; Augulis, R.; Stuart, M. C. A.; Knoester, J.; van Loosdrecht, P. H. M., Exciton Spectra and the Microscopic Structure of Self-Assembled Porphyrin Nanotubes. *J. Phys. Chem. B* **2009,** *113* (8), 2273-2283.

184. Arai, Y.; Segawa, H., Cl- complexation induced H- and J-aggregation of meso-tetrakis(4-sulfonatothienyl)porphyrin diacid in aqueous solution. *J. Phys. Chem.. B* **2011,** *115* (24), 7773-80.

185. Li, A.; Zhao, L.; Hao, J.; Ma, R.; An, Y.; Shi, L., Aggregation behavior of the template-removed 5,10,15,20-tetrakis(4-sulfonatophenyl)porphyrin chiral array directed by poly(ethylene glycol)-block-poly(L-lysine). *Langmuir* **2014,** *30* (16), 4797-805.

186. Rich, C. C.; McHale, J. L., Resonance Raman Spectra of Individual Excitonically Coupled Chromophore Aggregates. *J. Phys. Chem. C* **2013,** *117* (20), 10856-10865.

187. Arai, Y.; Segawa, H., Significantly enhanced adsorption of bulk self-assembling porphyrins at solid/liquid interfaces through the self-assembly process. *J. Phys. Chem. B* **2012,** *116* (45), 13575-81.

188. Rong, Y.; Chen, P.; Liu, M., Self-assembly of water-soluble TPPS in organic solvents: from nanofibers to mirror imaged chiral nanorods. *Chem. Commun. (Camb.)* **2013,** *49* (89), 10498-500.

189. Reddy, M. H.; Al-Shammari, R. M.; Al-Attar, N.; Kennedy, E.; Rogers, L.; Lopez, S.; Senge, M. O.; Keyes, T. E.; Rice, J. H., Micro- or nanorod and nanosphere structures derived from a series of phenyl-porphyrins. *Phys. Chem. Chem. Phys.* **2014,** *16* (9), 4386-93.

190. Wold, D. J.; Frisbie, C. D., Formation of Metal−Molecule−Metal Tunnel Junctions: Microcontacts to Alkanethiol Monolayers with a Conducting AFM Tip. *J. Am. Chem. Soc.* **2000,** *122* (12), 2970-2971.

191. Bumm, L. A.; Arnold, J. J.; Dunbar, T. D.; Allara, D. L.; Weiss, P. S., Electron Transfer through Organic Molecules. *J. Phys. Chem. B* **1999,** *103* (38), 8122-8127.

192. Wold, D. J.; Frisbie, C. D., Fabrication and Characterization of Metal−Molecule−Metal Junctions by Conducting Probe Atomic Force Microscopy. *J. Am. Chem. Soc.* **2001,** *123* (23), 5549-5556.

193. Brownfield, A. L.; Causey, C. P.; Mullen, T. J., Influence of Solvent on Octadecyltrichlorosilane Nanostructures Fabricated Using Particle Lithography. *J. Phys. Chem. C* **2015,** *119* (22), 12455-12463.

194. Schwab, A. D.; Smith, D. E.; Rich, C. S.; Young, E. R.; Smith, W. F.; de Paula, J. C., Porphyrin Nanorods. *J. Phys. Chem. B* **2003,** *107* (41), 11339-11345.

195. Brownfield, A. L.; Causey, C. P.; Mullen, T. J., Influence of Solvent on Octadecyltrichlorosilane Nanostructures Fabricated Using Particle Lithography. *J. Phys. Chem. C* **2015,** *119* (22), 12455-12463.

196. Bezryadin, A.; Dekker, C.; Schmid, G., Electrostatic trapping of single conducting nanoparticles between nanoelectrodes. *Appl. Phys. Lett.* **1997,** *71* (9), 1273.

197. Perrin, M. L.; Verzijl, C. J. O.; Martin, C. A.; Shaikh, A. J.; Eelkema, R.; van EschJan, H.; van Ruitenbeek, J. M.; Thijssen, J. M.; van der Zant, H. S. J.; Dulic, D., Large tunable image-charge effects in single-molecule junctions. *Nat Nano* **2013,** *8* (4), 282-287.

198. Wang, Y. T.; Zhou, Y. X.; Sokolov, J.; Rigas, B.; Levon, K.; Rafailovich, M., A potentiometric protein sensor built with surface molecular imprinting method. *Biosens Bioelectron* **2008,** *24* (1), 162-166.

199. Chen, H.; Heng, C. K.; Puiu, P. D.; Zhou, X. D.; Lee, A. C.; Lim, T. M.; Tan, S. N., Detection of Saccharomyces cerevisiae immobilized on self-assembled monolayer (SAM) of alkanethiolate using electrochemical impedance spectroscopy. *Anal. Chim. Acta* **2005,** *554* (1-2), 52-59.

200. Evrard, D.; Lambert, F.; Policar, C.; Balland, V.; Limoges, B., Electrochemical Functionalization of Carbon Surfaces by Aromatic Azide or Alkyne Molecules: A Versatile Platform for Click Chemistry. *Chem.-Eur. J.* **2008,** *14* (30), 9286-9291.

201. Azzaroni, O.; Cipollone, M.; Vela, M. E.; Salvarezza, R. C., Protective properties of dodecanethiol layers on copper surfaces: The effect of chloride anions in aqueous environments. *Langmuir* **2001,** *17* (5), 1483-1487.

202. Brunoro, G.; Frignani, A.; Colledan, A.; Chiavari, C., Organic films for protection of copper and bronze against acid rain corrosion. *Corros. Sci.* **2003,** *45* (10), 2219-2231.

203. van Bommel, K. J. C.; Friggeri, A.; Mateman, D.; Geurts, F. A. J.; van Leerdam, K. G. C.; Verboom, W.; van Veggel, F. C. J. M.; Reinhoudt, D. N., Self-assembled monolayers on gold for the fabrication of radioactive stents. *Adv. Funct. Mater.* **2001,** *11* (2), 140-146.

204. Venkataraman, L.; Klare, J. E.; Tam, I. W.; Nuckolls, C.; Hybertsen, M. S.; Steigerwald, M. L., Single-molecule circuits with well-defined molecular conductance. *Nano Lett.* **2006,** *6* (3), 458-462.

205. Chehimi, M. M.; Hallais, G.; Matrab, T.; Pinson, J.; Podvorica, F. I., Electro- and Photografting of Carbon or Metal Surfaces by Alkyl Groups. *J. Phys. Chem. C* **2008,** *112* (47), 18559-18565.

206. Combellas, C.; Kanoufi, F.; Osman, Z.; Pinson, J.; Adenier, A.; Hallais, G., Electrografting of the cyanomethyl radical onto carbon and metal surfaces. *Electrochim. Acta* **2011,** *56* (3), 1476-1484.

207. Berisha, A.; Combellas, C.; Hallais, G.; Kanoufi, F.; Pinson, J.; Podvorica, F. I., Photochemical Grafting and Patterning of Metallic Surfaces by Organic Layers Derived from Acetonitrile. *Chem. Mater.* **2011,** *23* (15), 3449-3459.

208. Pinson, J.; Podvorica, F., Attachment of organic layers to conductive or semiconductive surfaces by reduction of diazonium salts. *Chem. Soc. Rev.* **2005,** *34* (5), 429-439.

209. Piner, R. D.; Hong, S.; Mirkin, C. A., Improved imaging of soft materials with modified AFM tips. *Langmuir* **1999,** *15* (17), 5457-5460.

210. Hansma, P. K.; Cleveland, J. P.; Radmacher, M.; Walters, D. A.; Hillner, P. E.; Bezanilla, M.; Fritz, M.; Vie, D.; Hansma, H. G.; Prater, C. B.; Massie, J.; Fukunaga, L.; Gurley, J.; Elings, V., Tapping Mode Atomic-Force Microscopy in Liquids. *Appl. Phys. Lett.* **1994,** *64* (13), 1738-1740.

211. Xu, S.; Cruchon-Dupeyrat, S. J. N.; Garno, J. C.; Liu, G. Y.; Jennings, G. K.; Yong, T. H.; Laibinis, P. E., In situ studies of thiol self-assembly on gold from solution using atomic force microscopy. *J. Chem. Phys.* **1998,** *108* (12), 5002-5012.

212. Liu, G. Y., Nanofabrication of self-assembled monolayers using scanning probe lithography. *Abstr. Pap. Am. Chem. S.* **2000,** *220*, U431-U431.

213. Schwartz, D. K., Mechanisms and kinetics of self-assembled monolayer formation. *Annu. Rev. Phys. Chem.* **2001,** *52* (1), 107-137.

APPENDIX A: LETTER OF PERMISSION

Xianglin Zhai

From: Molecules Editorial Office / MDPI <molecules@mdpi.com>
Sent: Thursday, January 21, 2016 7:25 PM
To: Xianglin Zhai
Subject: Re: permission request

Dear Dr. Zhai,

Thank you very much for your inquiry regarding the copyright of material that has been published in our journal.

Since the article you asked about is licensed under a Creative Commons-BY license, you can freely use the figure if the authors of the article created it themselves - of course under the premise that you cite the article when using the figure.

For further information about the CC-BY license and our copyright, please visit:
http://www.mdpi.com/about/openaccess

<http://www.mdpi.com/about/openaccess>

Regarding the citation: there is no need to write "reprinted with permission etc." since you don't need a permission with CC BY - simply cite the original paper of the figure in your bibliographic references of your thesis like any normal citation.

Hope I was able to help you. If you have any further questions, please don't hesitate to contact me again.

Kind regards,
Ms. Ran Dang
Managing Editor
Molecules (http://www.mdpi.com/journal/molecules)

News: Newly Released Impact Factor for Molecules (2014): 2.416

Follow us on Twitter: https://twitter.com/Molecules_MDPI (@Molecules_MDPI)
Linkedin: https://www.linkedin.com/in/molecules
--

MDPI AG
Molecules Editorial Office
Klybeckstrasse 64, 4057 Basel, Switzerland Tel. +41 61 683 77 34; Fax: +41 61 302 89 18
E-Mail: molecules@mdpi.com
http://www.mdpi.com/journal/molecules

On 1/22/2016 1:28 AM, Xianglin Zhai wrote:
>
> Dear editor,
>
>
> I am requesting a letter of permission to reprint from MDPI on the
> article that I have published in the journal of /Molecules,
> /"*/Nanoscale Lithography Mediated by Surface Self-Assembly of
> 16-[3,5-Bis(Mercaptomethyl)phenoxy]hexadecanoic Acid on Au(111)

1

> Investigated by Scanning Probe Microscopy/*" with authors: Xianglin
> Zhai <http://www.mdpi.com/search?authors=Xianglin%20Zhai&orcid=>,
> Han Ju Lee
> <http://www.mdpi.com/search?authors=Han%20Ju%20Lee&orcid=>,Tian Tian
> <http://www.mdpi.com/search?authors=Tian%20Tian&orcid=>,T. Randall Lee
> <http://www.mdpi.com/search?authors=T.%20Randall%20Lee&orcid=>
> andJayne C. Garno
> <http://www.mdpi.com/search?authors=Jayne%20C.%20Garno&orcid=>*.* I
> would like to include the article in my dissertation to be submitted
> to Louisiana State University.
>
>
> I would appreciate your permission to use the above article.
>
>
> Thank you for your consideration,
>
>
> --
>
> Xianglin Zhai Ph.D. candidate Chemistry Department Louisiana State
> University B7 Choppin Hall Baton Rouge, LA 70803 Office: 225-578-8853
> Facsimile: 225-578-3458 e-mail: xzhai1@lsu.edu <mailto:xzhai1@lsu.edu>
>
>
>
>
>
>
>
>
>
>
>
>

APPENDIX B: OPERATING PROCEDURE FOR SCANNING TUNNELING MICROSCOPY IN AMBIENT ATMOSPHERE

In Scanning Tunneling Microscopy (STM), a bias voltage is applied between a sharp, conducting tip and the sample. When the tip approaches the sample, electrons "tunnel" through the narrow gap, either from the sample to the tip or vice versa, depending on the bias voltage. The tunneling current is held constant throughout the scan, magnitude difference in the tunneling current. The interaction is between single atoms in the sample and tip, giving STM remarkable high lateral resolution.

Nose assembly and multi-purpose scanner

The Agilent multi-purpose scanner, when equipped with an STM nose assembly (Figure B1), can be used for STM.

Figure B1 Scanner and nose assembly for STM. Insert is the STM nose assembly.

Tips preparation for STM

Agilent STM tips are pre-cut of chemically etched lengths of 0.25 mm OD, 80% platinum-20% iridium wire (Figure B2). If the wire tip is damaged it can be trimmed and used again (Figure B3).

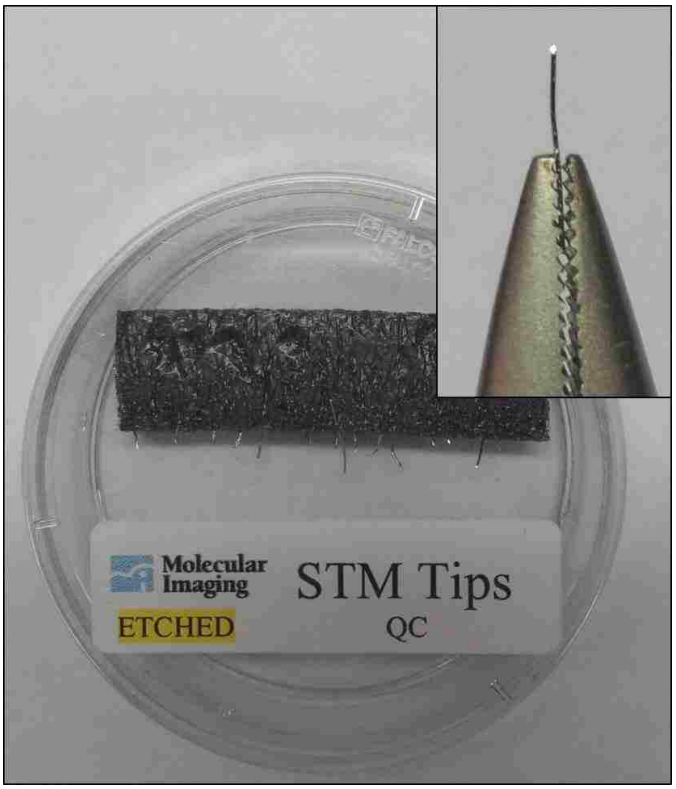

Figure B2 Pre-cut STM tips. Insert is a close-up view of a STM wire picked with pliers.

1. Use the pointed tweezers to carefully pick up a piece of wire (tip).
2. Hold the end of the wire tightly with the pliers.
3. Holding the tip with the pliers, move the cutters at a length of approximately 4 mm, as obliquely as possible (in a very sharp angle).
4. Close the cutters until you can feel the wire, but do not cut it.
5. To obtain the required sharpness, the wire needs to be torn off by pulling the wire cutter quickly away from you, rather than cutting cleanly through the wire.

6. Use the pointed tweezers to hold the tip wire right behind the tip.
7. Release the flat pliers.
8. Insert the tip into the nose assembly. Grasp the tip with pointed tweezers, then insert it into the hollow tube until it protrudes approximately 2 mm.
9. Place the scanner onto the microscope base.

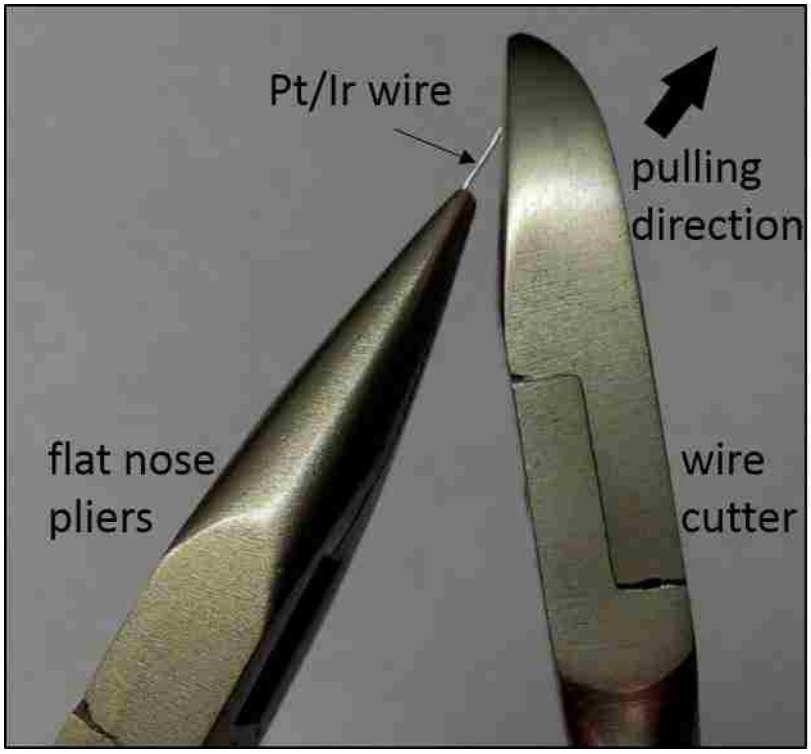

Figure B3 Tip preparation.

Mount sample onto sample plate

10. Prepare the sample and place it on a sample stage. The sample must be electrically isolated from the sample.
11. Attach an electrode from the sample plate to the sample. Lift the spring-loaded electrode clip on the sample stage and insert the electrode under it. Connect the electrode to the sample, ensuring good contact (Figure B4).

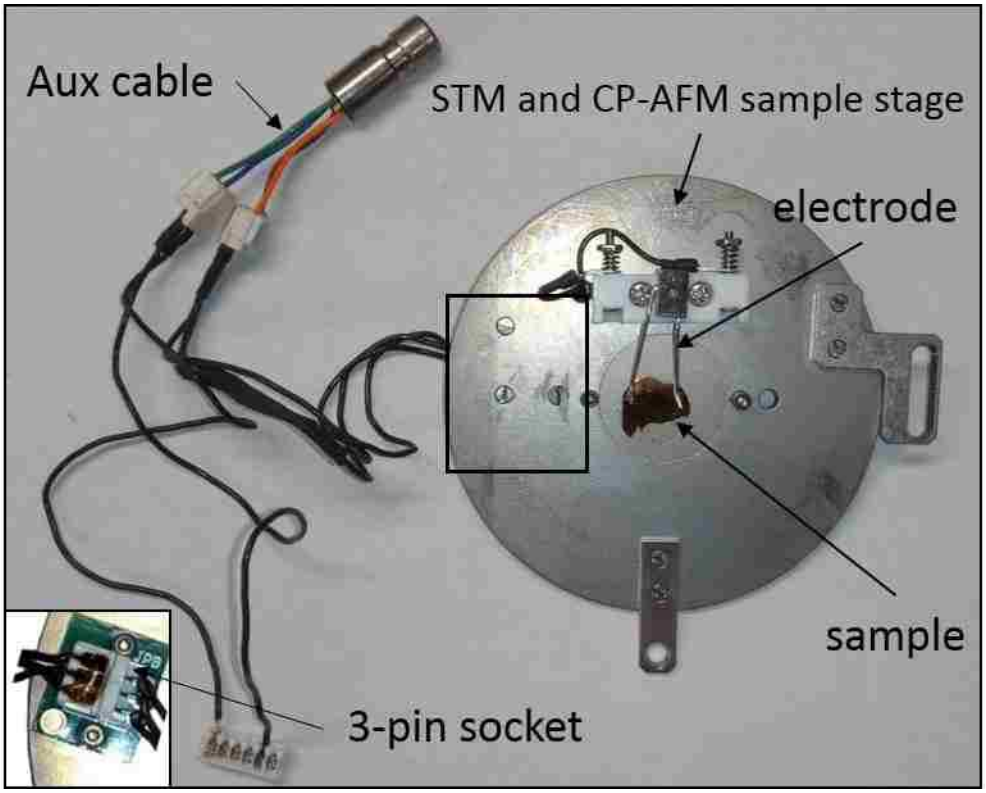

Figure B4 Sample plate connection. Insert is the backside of the boxed area, shows the 3-pin socket plugged with the 3-pin EC connector.

12. Plug the 3-pin EC connector of the Aux cable plate into the 3-pin socket on the back of the sample stage. Plug the other end of the Aux cable into the Aux socket on the microscope base.

    Note: The sample plate cable can transfer low levels of electric noise to the sample. During very high resolution imaging this can affect images quality during high resolution imaging (usually less than 1 μm^2 area). First plugging the sample plate cable to the flexible 3-wire umbilical included with the sample plate is recommended. The umbilical should then be plugged in to the microscope base.

STM imaging procedure

13. In PicoView 1.12, choose **Mode > STM**.

14. In the **Servo** window enter the **Sample Bias Voltage**. Typical values are 50-200 millivolts (0.05-0.2 V). A positive bias indicates current flow from the tip to the sample, and vice versa for negative bias (Figure B5).

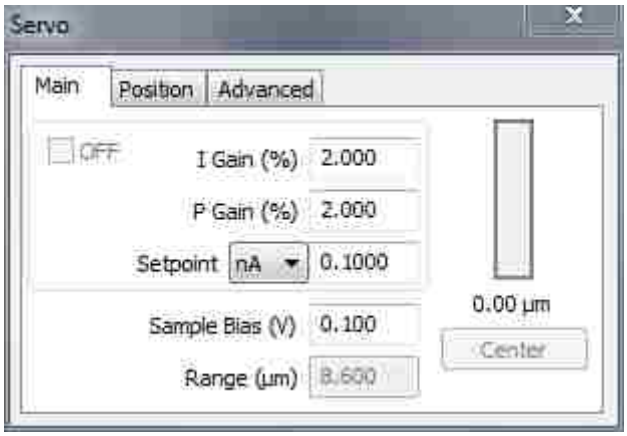

Figure B5 Servo window settings for STM imaging.

15. Enter the **Setpoint** current, in nanoamps, that the system will try to hold constant during scanning. Atypical setting is 1-2 nA.
16. Enter the **I** and **P** gains for the z-servo, which will dictate how quickly the system will adjust to changes in tunneling current. Typical values are 1-2 % for both gains.
17. In the **Realtime Images** window choose to display images for **Current** and **Topography**.
18. In the **Scan and Motor** window set the scan **Size** and **Speed**. A scan **Speed** of 1 **ln/s** is a good starting value.
19. Using the **Close** switch on the **HEB**, lower the scanner until the tip is close to, but not touching, the scanner. The video system is not useful in the STM as the tip is essentially vertical, so view the tip from the side of the microscope and bring it as close to the sample as you can. Be certain to not drive the tip into the sample. To be safe you can make the approach length longer, which will just extended time to the approach.

20. Click the **Approach** button in PicoView's toolbar. The scanner will lower until the Setpoint current is reached.
21. For lowest current operation, once engaged reduce the **Setpoint** value until the indicator in the **Servo** window changes from green to red. Then increase the **Setpoint** until the indicator in the **Servo** window just turns green. For rougher surfaces you may need to increase the setpoint current slightly more.
22. In the **Scan and Motor** window click the **Up** or **Down** arrows to begin the scan.

APPENDIX C: OPERATING PROCEDURE FOR ANGSTROM THERMAL EVAPORATOR

Angstrom thermal evaporator is used to make gold thin films on substrates. Usually, the substrates are silicon wafer and muscovite mica. The gold thin film made by Angstrom thermal evaporator is monocrystalline Au(111) surface. [The location of the gold evaporator is in CMB 454]

Safety grounding

A grounding probe is fastened to the back of the system frame. It is required of all operators to ground the high voltage leads inside the chamber connected to the electron beam as soon as any chamber door is opened. Residual voltages at these leads could be potentially harmful.

Figure C1 Grounding probe.

Preparing the instrument

1. Turn on the gas source.

Figure C2 Location of the gas source.

2. Turn on the cooling water source.

Figure C3 Location of the cooling water source.

3. Turn on the main disconnect.

Figure C4 Location of the main disconnect.

4. Level the pneumatic gas shut off knob.

Figure C5 Location of the pneumatic gas shut off knob.

Editing Parameters within the *Inficon Deposition Controller*

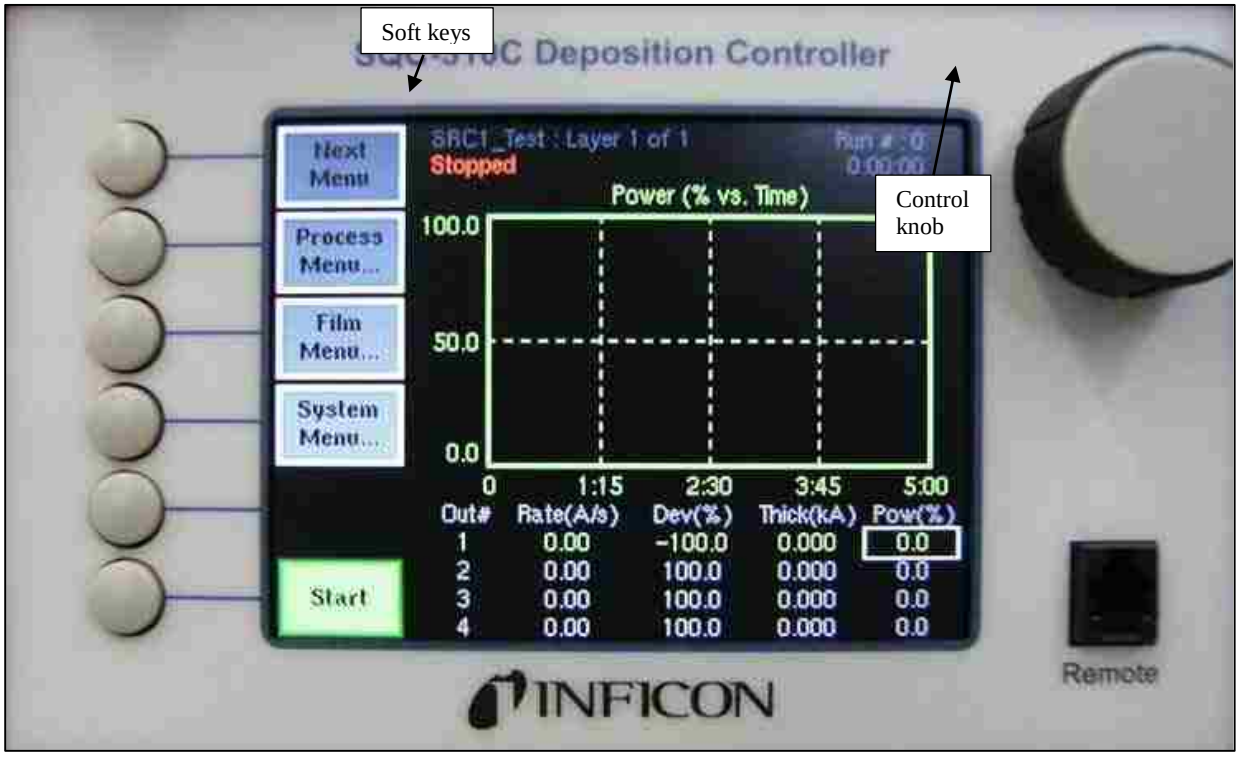

Figure C6 Control panel of SQC-310C deposition controller.

To edit a parameter in any menu, turn the control knob to scroll to the desired parameter, and press the Edit soft key. The cursor will move to the parameters value. Turn the control knob to set the desired parameter value. The soft key functions in Edit mode are as follows:

Next: Store and move to next parameter for editing. It will just move to the next parameter if no change has been entered.

Cancel: Stop editing, do not store and return the selected parameter to its previous value.

Enter: Save the value entered, ends editing for selected parameter.

1. Press ***Next Menu*** until the Film Menu soft key is displayed. Press ***Film Menu*** to view a list of stored films. Turn the setting knob to scroll to an entry in the list that is currently labeled **<*Empty*>** to create a new film.

2. Press the ***Create*** soft key to create a default film at that location. Note the film number that you just created (or you can edit film name by pressing ***Edit Name*** key). Press the ***Edit*** soft key. Enter parameter values in the required fields below. (typical parameters: [film name], p Term 20, I Term 0.5, D Term 0, Material Gold, Film Tooling 95)

Figure C7 Editing film parameters.

Press the ***Main Screen*** soft key to return to the main screen.

3. Press the ***Process Menu*** soft key to view a list of processes. Turn the setting knob to scroll to an entry in the list that is labeled **<*Empty*>** if you wish to create a new process and press the ***Create*** soft key (or you can edit film name by pressing ***Edit Name*** key). Press the ***Select*** soft key to make the new process the active process.

Figure C8 Process menu.

4. Press the ***Edit*** soft key to view a list of layers in the selected process. The layer list should be blank if it is a new process. Press ***Insert New***, and then scroll down the list of films to the film you just created. Press ***Insert Normal*** to insert the selected film as Layer 1.1. The display returns to the ***Layer Select*** menu.

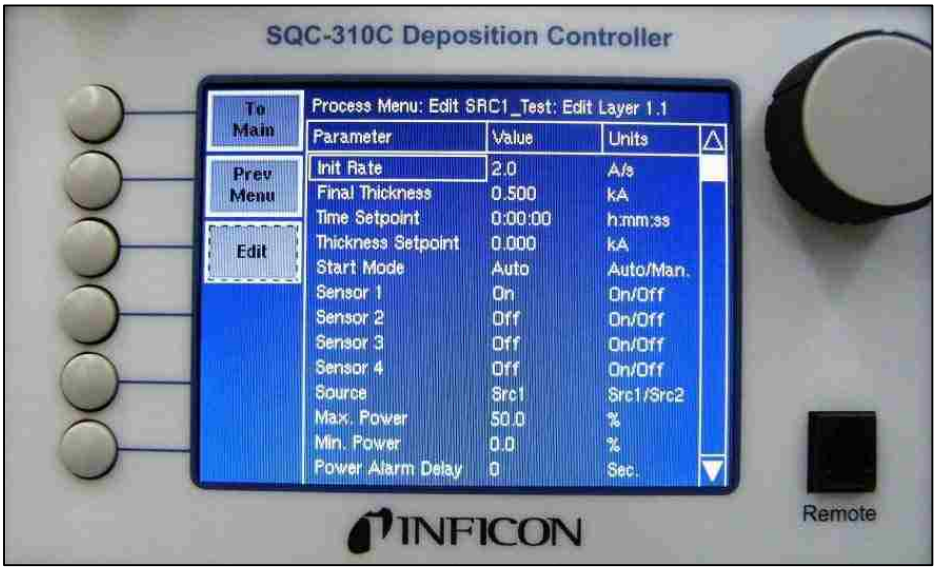

Figure C9 Layer menu.

5. Press ***Main Screen*** soft key to return to the main menu screen.
6. In the main menu screen press the ***Next Menu*** soft key one time. Make sure that Automatic mode is active (Auto/Manual) NOT Manual mode (Manual/Auto).
7. Click ***Edit*** soft key to type in *initial rate* (3 Å), *film thickness* (2.000 kÅ), change *start mode* to *auto*, turn on *sensor 2*, and source 2.
8. Press the ***Next Menu*** soft key to return to the main menu screen.

Figure C10 Deposition interface.

Mounting substrate and depositing metal

1. Bring the precut mica, depositing metal (gold pellets), clean gloves, sharp tip tweezers into glove box.
2. When the chamber door is opened a probe must be touched to both of the high voltage copper conductors that are connected from the chamber feed through to the electron beam gun. This is illustrated in Figure C11.

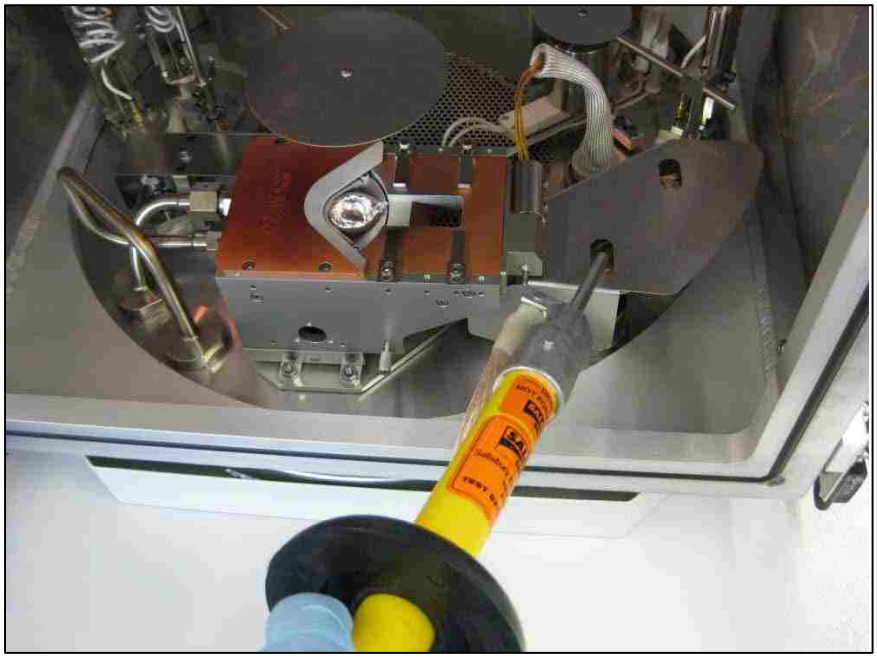

Figure C11 Probe touching high voltage conductor.

3. Fix the freshly cleaved mica onto the sample plate using the clips. (Note: choose thicker piece of mica, clean side up.)
4. Mount the sample plate onto the holder inside depositing chamber. (Note: clean mica side faces down, turn sample plate to lock)
5. Close shudder.
6. Mount the crucible onto *source 2(*corresponds to *sensor 2, right side one)* or *source 3 (*corresponds to *sensor 1, left side one).*
7. Put 6 gold pellets on crucible. (Note: this number for gold pellets is empirical for a 200 nm thick gold film. Different number for other thickness may apply)
8. Close chamber.
9. Turn on the turbo pump. Wait until the pressure inside the chamber decreases to 10^{-7} torr to initiate depositing process for gold (usually it takes 12 h) or to 10^{-6} torr for aluminum (usually it takes less than 1h).

Deposition process

1. Preheat the sample stage at 325 C for 30 min. Use arrows on substrate temp to set green value. Press substrate heater (green button). Press start on vacuum pump.

Figure C12 Operating panel for angstrom thermal evaporator.

2. Turn off the heater. [When heating up the substrate, the pressure in the chamber went up to 2.9 x 10^{-6} torr. Do not start deposition process until the pressure goes back to 10^{-7} torr. It will be about one hour after the heater turned off.]
3. Check source 2 sensor 2 settings then press the ***Start*** soft key to begin.
4. When the process is finished, turn on the sample heater again to 365 C to anneal the Au(111) film under vacuum for 30 min.
5. Turn off the heater by pressing the green button. Allow about 2 hours for the substrate to cool down.
6. To take your sample out of the chamber, press the ***Start/Stop*** button on the vacuum pump controller to initiate the venting process.

7. After the chamber is vented, open the chamber. Carefully remove the substrate after the sample holder cooled to room temperature.

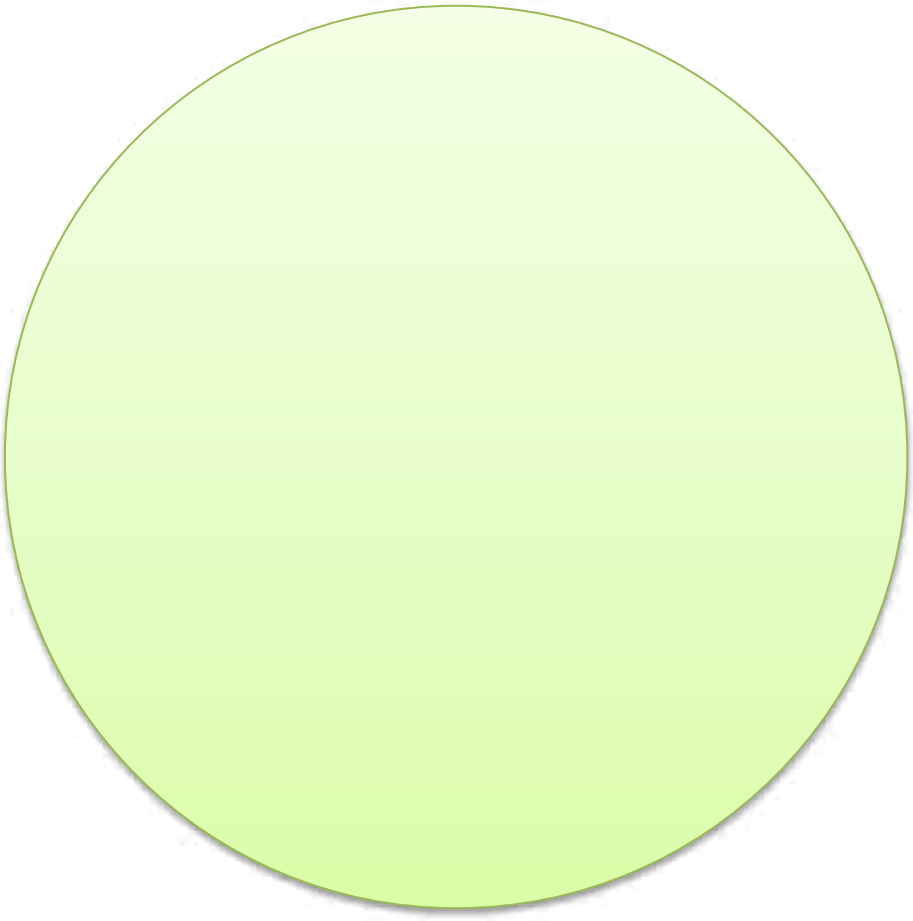

Figure C13 Real size of the mica substrate (4.7 in./12cm in diameter).

APPENDIX D: SUPPLEMENTAL INFORMATION FOR NANOSCALE LITHOGRAPHY MEDIATED BY SURFACE SELF-ASSEMBLY OF 16-[3,5-BIS(MERCAPTOMETHYL)PHENOXY]HEXADECANOIC ACID ON AU(111) INVESTIGATED WITH SCANNING PROBE MICROSCOPY[3]*

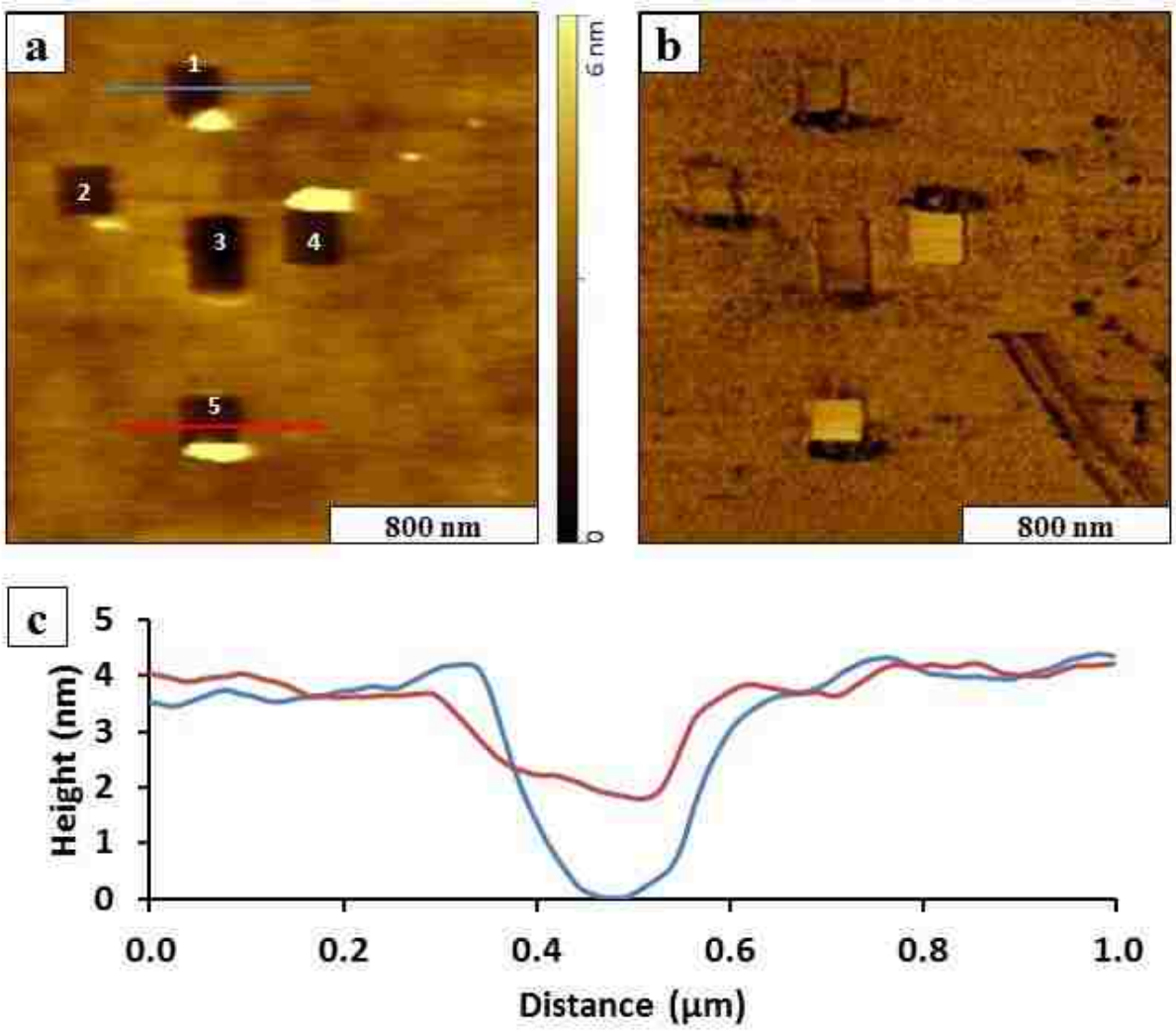

Figure D1 Nanopatterns fabricated by scanning probe based nanolithography within a bilayer of 16-[3,5-bis(mercaptomethyl)phenoxy]hexadecanoic acid (BMPHA). *(a)* Side-by-side views of nanoshaved and nanografted patterns. These figures present a zoom-out view of Figure 3.5*(a)* Contact-mode topography image acquired in ethanol. The areas 1, 2 and 3 are nanoshaved regions; areas 4 and 5 are nanografted patterns of n-octadecanethiol (ODT). *(b)* Simultaneously acquired lateral force image; *(c)* cursor profiles corresponding to the red and blue lines in *(a).* The blue line reveals depth of the nanoshaved area, the red line profiles the depth of nanografted pattern. The bilayer of BMPHA was prepared by immersion of a Au(111) substrate in 5 mM ethanolic BMPHA solution for 30 h. The concentration of ethanolic ODT solution used for nanografting was 1 mM.

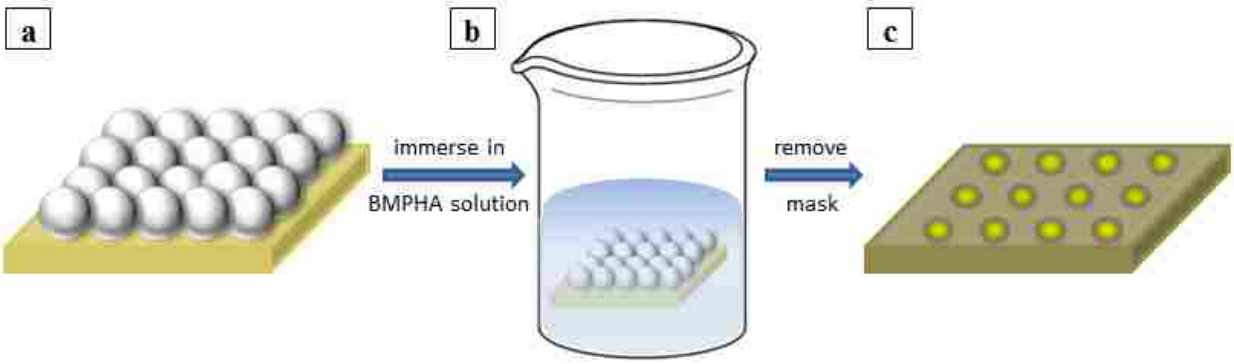

Figure D2 Steps for preparing nanopatterns of thiol-based films using immersion particle lithography. *(a)* A surface mask of close-packed mesospheres was prepared on template-stripped gold, and annealed for 12 h at 150 C. *(b)* The masked substrate was immersed in an ethanolic solution of dilute multidentate thiol. *(c)* The mask of silica spheres was removed by rinsing and sonication. The uncovered pore areas can be filled with a second molecule, such as n-alkanethiols with a further immersion step.

APPENDIX E: SUPPLEMENTAL INFORMATION FOR CONDUCTIVE-PROBE MEASUREMENTS WITH NANODOTS OF FREE-BASE AND METALLATED PORPHYRINS

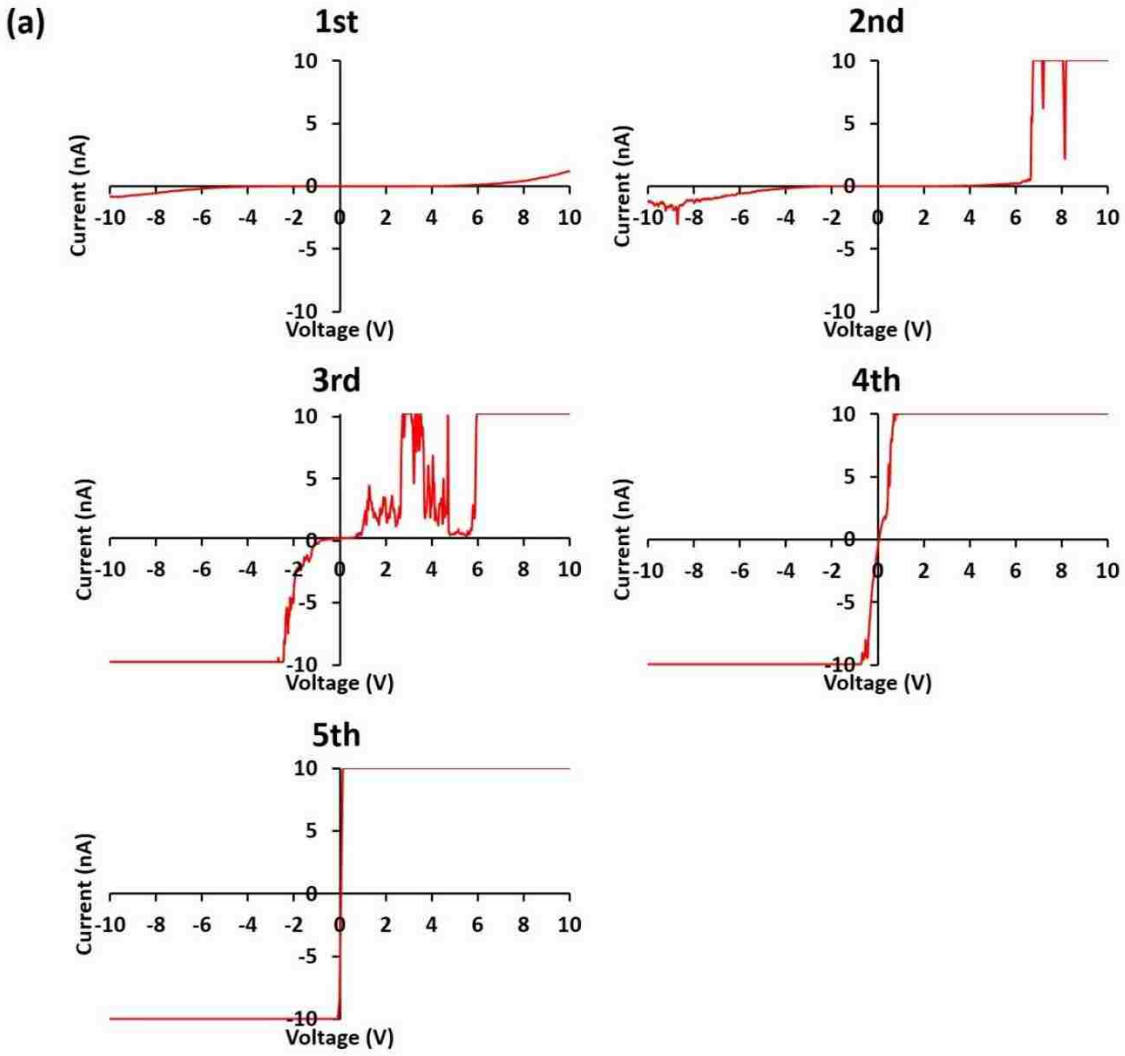

Figure E1 Successive voltage sweeps taken from an individual TPP nanodots, to evaluate changes after multiple measurements. *(a)* The first five I-V profiles taken from a nanodot with 6 nm height;

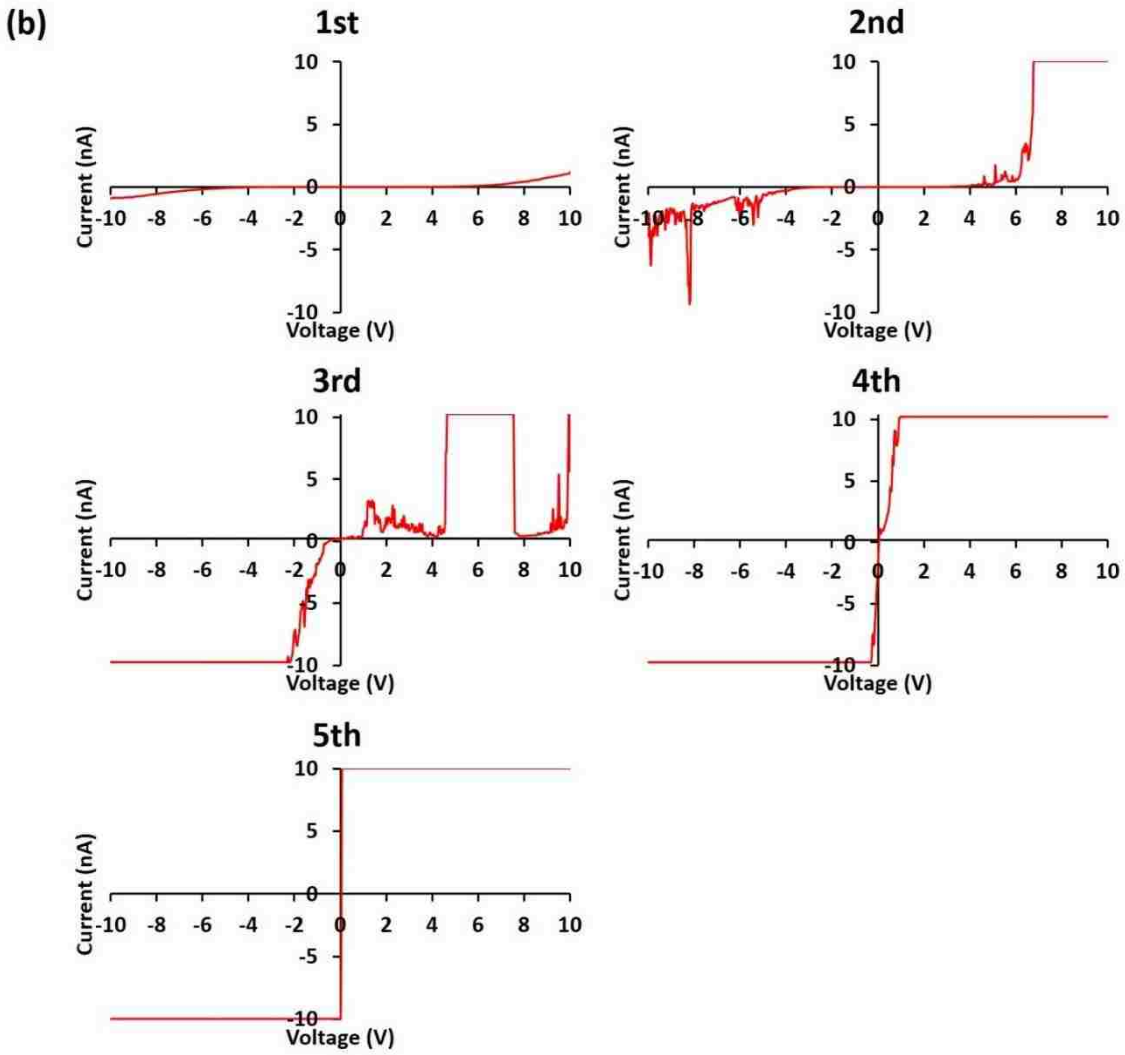

Figure E1 Successive voltage sweeps taken from an individual TPP nanodots, to evaluate changes after multiple measurements. *(b)* The first five I-V profiles taken from a nanodot with 7 nm height.

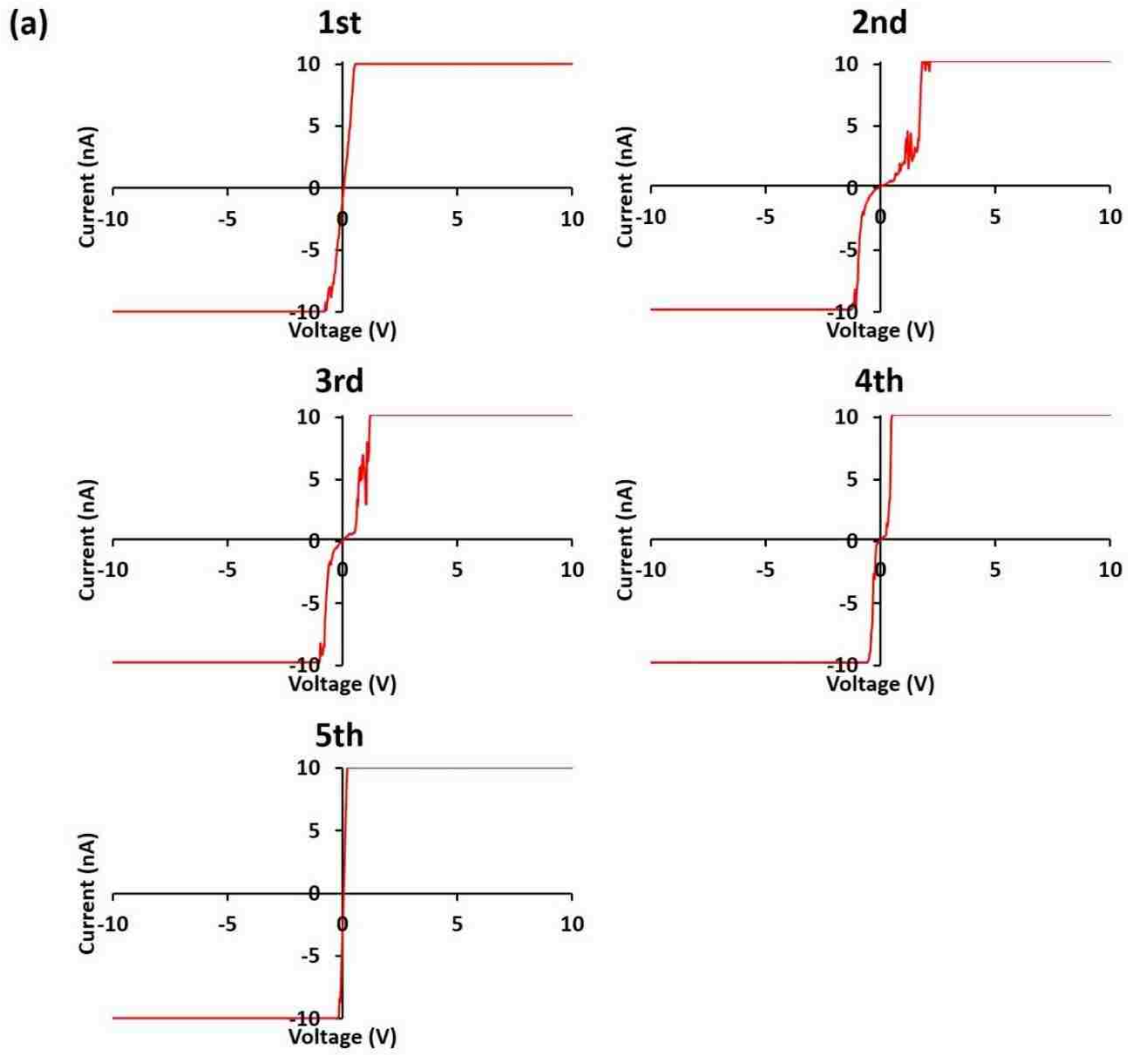

Figure E2 Successive voltage sweeps taken from an individual TPC nanodots, to evaluate changes after multiple measurements. *(a)* The first five I-V profiles taken with a TPC nanodot with 6 nm height;

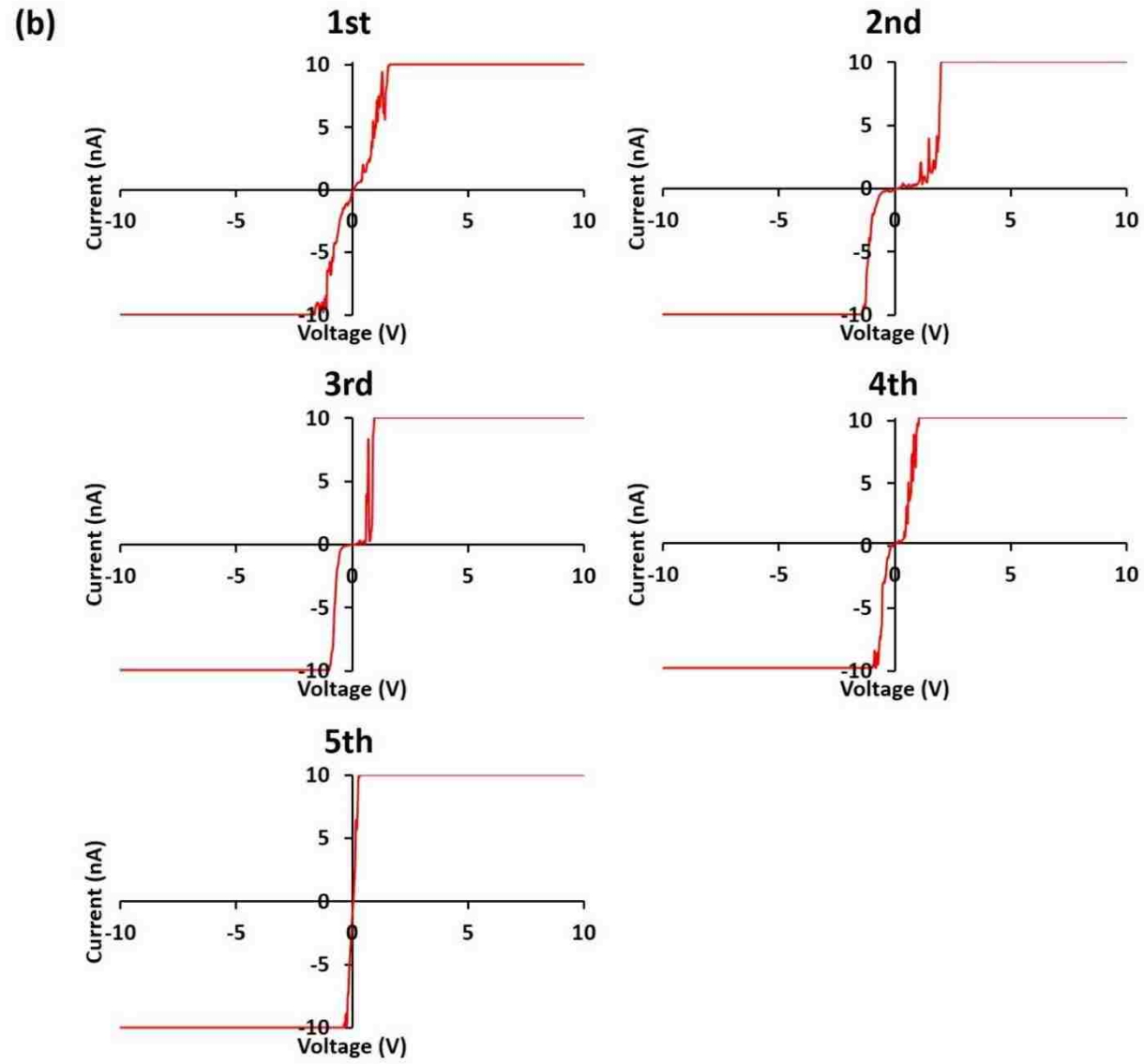

Figure E2 Successive voltage sweeps taken from an individual TPC nanodots, to evaluate changes after multiple measurements. *(b)*The first five I-V profiles taken from a TPC nanodot with 7 nm height.

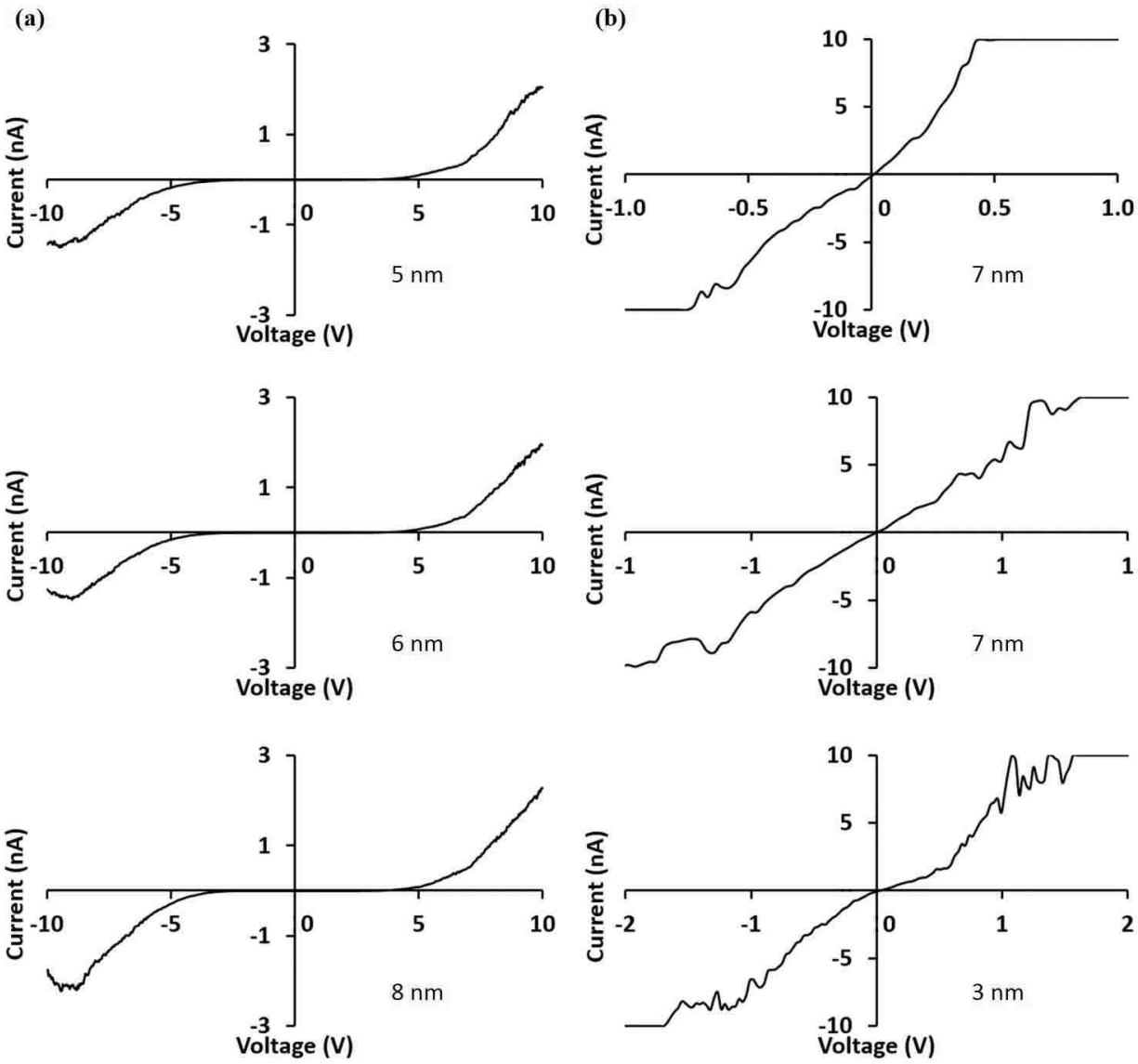

Figure E3 Example I-V curves for *(a)* TPP nanodots and *(b)* TPC nanodots with selected heights. Distinct differences in the conductivity of TPP and TPC at the nanoscale are shown by the I-V curves collected from individual nanodots. Nanodots of TPP exhibit semi-conductive I-V profiles, whereas TPC nanodots have wire-like characteristics. The cobalt atom coordinated to the porphyrin structure increases the conductivity of the nanodots.

APPENDIX F: SUPPLEMENTAL INFORMATION FOR DISTANCE-DEPENDENT MEASUREMENTS OF THE CONDUCTANCE OF PORPHYRIN NANORODS STUDIED WITH CONDUCTIVE-PROBE ATOMIC FORCE MICROSCOPY

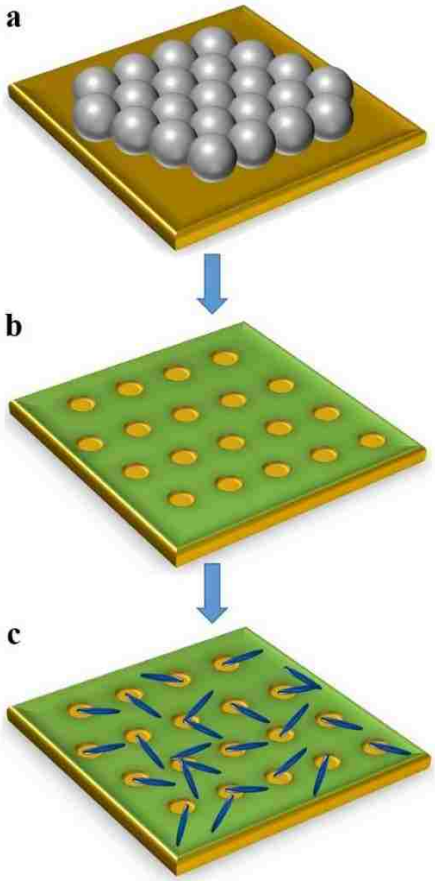

Figure F1 Steps of immersion particle lithography with porphyrins. *(a)* Mesospheres were deposited on Au(111) to form a surface mask; *(b)* nanoholes within a dodecanethiol SAM formed on Au(111) after immersing the masked surface in a dodecanethiol solution and then rinsing away the mesospheres from the surface; *(c)* porphyrin nanorods grow on the exposed Au(111) sites after an immersion step. A nanopore array was fabricated within dodecanethiol on Au(111). The steps of fabricating the nanopore array was described in previous work (Figure F1a).[3] The gold substrate masked with silica mesospheres was then submerged in ethanol containing dodecanethiol to prepare nanoholes within the thiol SAM. When the mesosphere mask was removed, a periodic arrangement of uncovered areas of substrate was disclosed as circular nanoholes. The array in thiol SAM on Au(111) was used to direct the growth of nanorods by immersing the template into the solution of TPC or TPP (Figure F1b). After the immersion of the template, porphyrin nanorods grew from the bare Au(111) area (Figure F1c). This protocol produces the porphyrin nanorods with one end connected to the bare gold areas and the remainder of the nanorod lying on the dodecanethiol SAM. The discrete circular areas of Au(111) serve as an electrode for CP-AFM. A platinum coated AFM tip serves as the other electrode for measuring the conductivity of the nanorods.

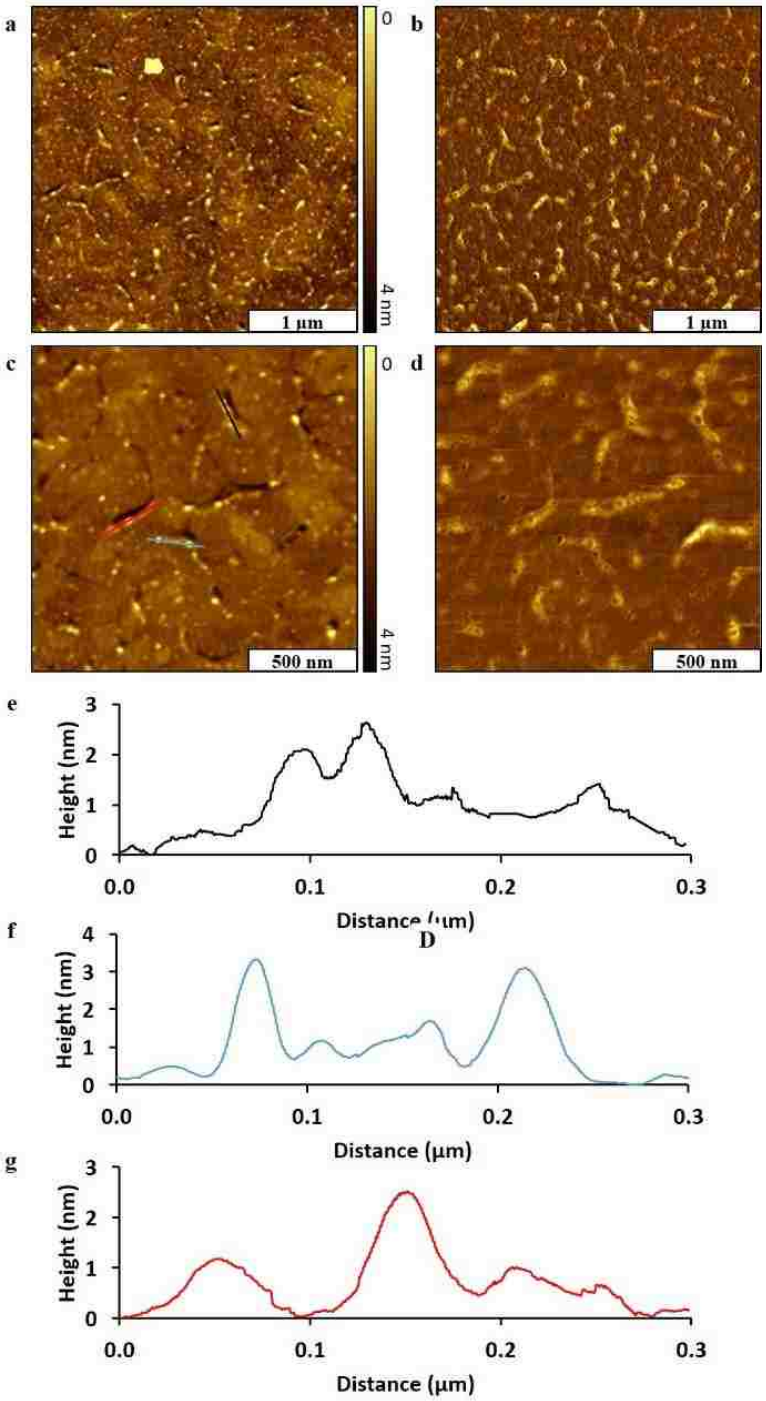

Figure F2 Control experiment to evaluate whether the nanorods form in solution or are grown from the surface. The experiments reveal aggregates of TPP were formed on gold by depositing 5 µL 10^{-5} M TPP solution. Nanorods were not observed. *(a)* A wide view of TPP aggregates shown with a topography frame; *(b)* corresponding phase image; (c) close up view of TPP aggregates; *(d)* simultaneously acquired phase image. Images were acquired by tapping mode AFM in ambient conditions. *(e)* Cursor profile of the black line in *(c)*; *(f)* cursor profile of the blue line in *(c)*; *(g)* cursor profile of the red line in *(c)*.

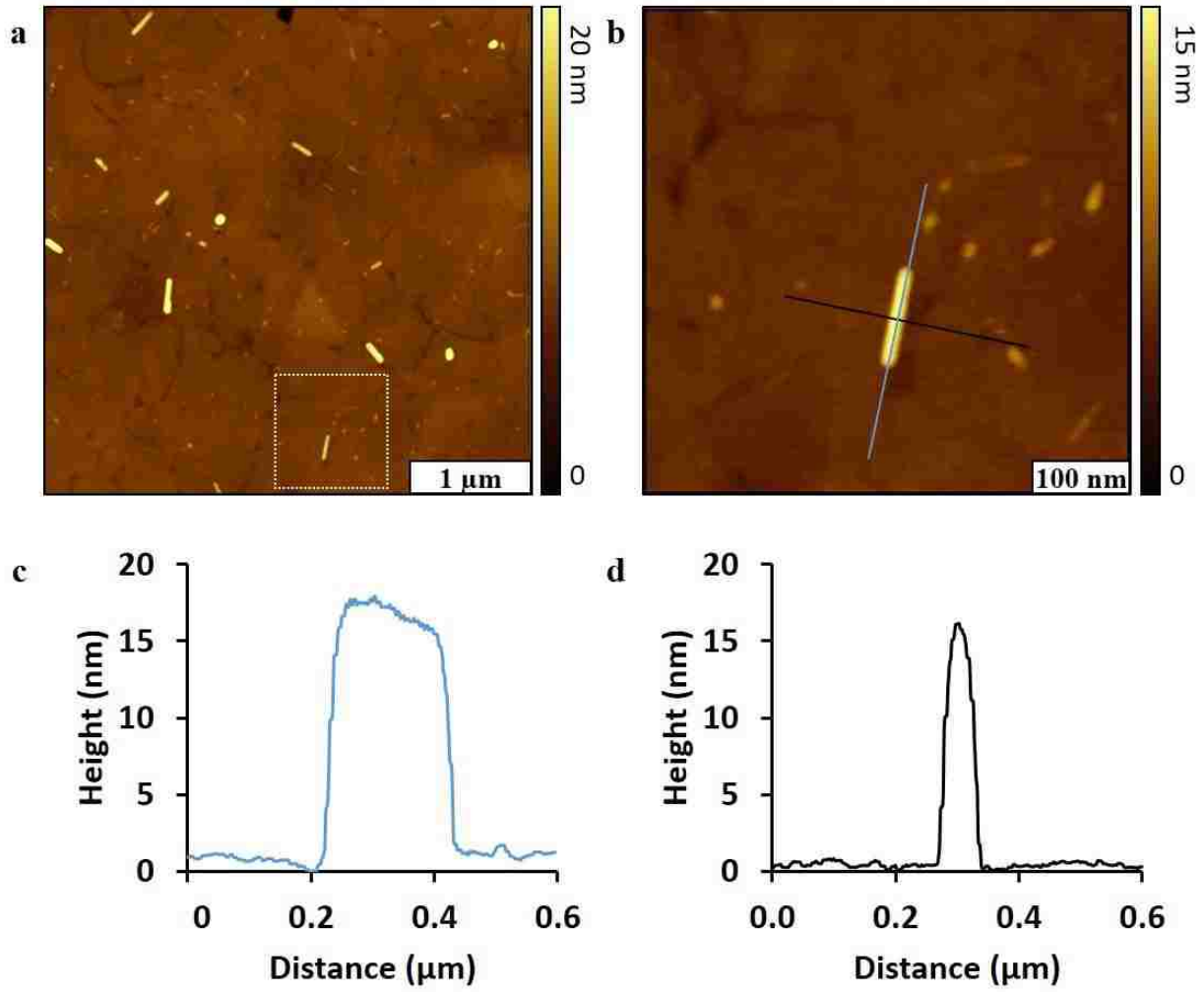

Figure F3 With extended immersion intervals of the substrate TPC nanorods were formed. *(a)* Topography frame; *(b)* An individual TPC nanorod shown in the white frame in *(a)*. The topography images were acquired with tapping mode AFM in ambient conditions. Nanorods of TPC formed on gold by immersing a freshly stripped gold substrate in a TPC solution (10^{-5} M for 42 h). The TPC molecules were dissolved in dichloromethane at 10^{-3} M and then diluted to 10^{-5} M in ethanol. *(c)* Cursor profile of a cross section of the TPC nanorod which corresponds to the blue line in *(a)*. *(d)* Cursor profile of a longitudinal section of the TPC nanorod which corresponds to the black line in *(b)*.

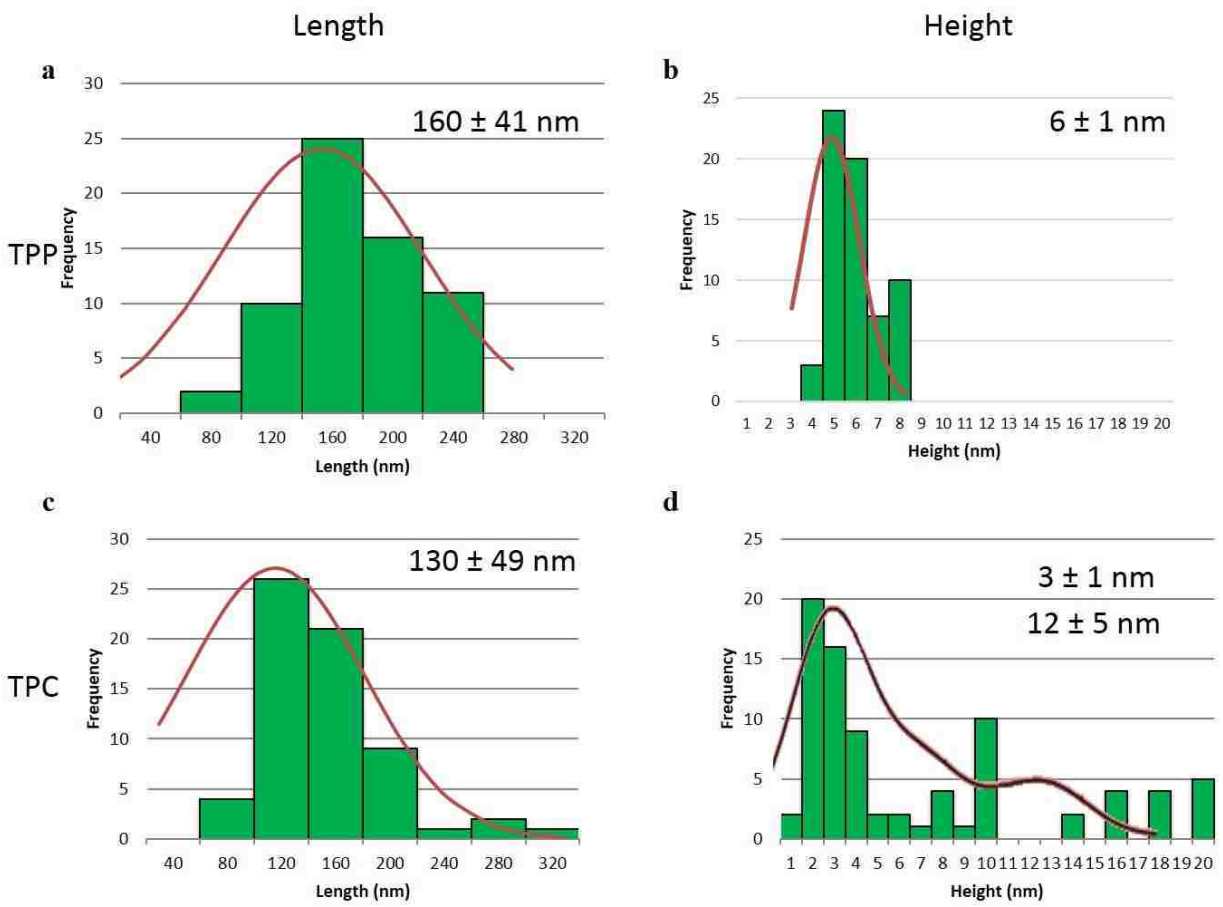

Figure F4 Histograms of the length and the height of TPP and TPC nanorods. *(a)* Length of TPP nanorods (*n*=64); *(b)* height of TPP nanorods (*n*=64); *(c)* length of TPC nanorods (*n*=82); *(d)* height of TPC nanorods (*n*=82). The solid lines represent the fit of the data to a Gaussian distribution. The accompanying values represent the means and standard deviations of the fits. The dashed lines in *(d)* are fitted with a double Gaussian distribution.

VITA

Xianglin Zhai is a native of Northeast China and was born in Harbin, Heilongjiang Province in 1983. He received his bachelor's degree in wood science and engineering from Northeast Forestry University (NEFU) in June 2006, followed by a master's degree in wood science and technology in 2009. During his time at NEFU, he participated in undergraduate research under Dr. Fenghu Wang for one year and was under the guidance of Dr. Yixing Liu for his master's research. Upon graduation, he worked as a research assistant in Dr. Chung-Yun Hse's lab in the USDA Southern Research Station in Pineville, LA, USA. In the spring of 2012, he began doctoral studies at Louisiana State University where he joined Dr. Jayne C. Garno's group. Thus far at LSU, Xianglin has published a first author publication. Two additional first author manuscripts are in submission. Xianglin is co-author of two publications and at least two additional shared manuscripts are in preparation. Xianglin presented original research at both regional and national conferences including two talks, six first-author poster presentations, and six co-authored posters. Xianglin directed senior thesis research for an LSU undergraduate student in chemistry, Denzel Alexander, who won a poster award for his studies with scanning probe characterizations of organic thin films. Xianglin has taught undergraduate laboratories at LSU for seven semesters and won a Teaching Award in 2014 for teaching the general chemistry lab. The competitive TA scholar awards recognize excellence for teaching undergraduates. The degree of Doctor of Philosophy he is expected to have the degree conferred at the Spring 2016 Commencement, Louisiana State University, Baton Rouge, LA.